

DESIGN, ANALYSIS AND DEVELOPMENT OF A HIGH TEMPERATURE ACTUATOR  
FOR GAS TURBINE BLADE TIP CLEARANCE CONTROL

MUSTAFA BULUT COŞKUN

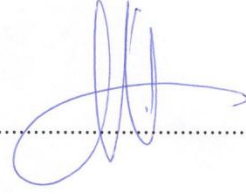
Submitted to the Graduate School of Engineering and Natural Sciences  
in partial fulfillment of  
the requirements for the degree of  
Master of Science

SABANCI UNIVERSITY

DESIGN, ANALYSIS AND DEVELOPMENT OF A HIGH TEMPERATURE ACTUATOR  
FOR GAS TURBINE BLADE TIP CLEARANCE CONTROL

APPROVED BY:

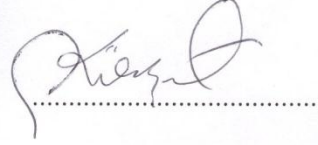
Assoc. Prof. Dr. Mahmut F. Akşit  
(Thesis Supervisor)



Assoc. Prof. Dr. Serhat Yeşilyurt



Assoc. Prof. Dr. Kürşat Şendur



Asst. Prof. Dr. Güllü Kızıldaş Şendur



Asst. Prof. Dr. İlyas Kandemir



DATE OF APPROVAL: 06.07.2011

© MUSTAFA BULUT COŞKUN 2011

ALL RIGHTS RESERVED

# DESIGN, ANALYSIS AND DEVELOPMENT OF A HIGH TEMPERATURE ACTUATOR FOR GAS TURBINE BLADE TIP CLEARANCE CONTROL

Mustafa Bulut COŞKUN

Mechatronics Engineering, M.Sc. Thesis, 2011

Thesis Supervisor: Assoc. Prof. Dr. Mahmut F. AKŞİT

Keywords: High temperature actuator, tip clearance control, friction, wear, tribometer, superalloy.

## ABSTRACT

During a typical startup cycle industrial gas turbine blades experience rapid radial thermal expansion while bulky shroud structure with larger thermal inertia requires much longer period to reach its operating temperature. Turbine designers have to leave a safe radial distance in order to prevent contact of blades to the surrounding annular casing. However, when thermal steady state in the turbine stage is achieved, shroud and casing grow and excessive amount of blade-shroud clearance remains. Engine efficiency is very sensitive to blade-shroud clearance. Just one millimeter of radial blade tip gap in first stage turbine section of a 150 MW class engine leads to 4% efficiency drop due to blade tip leakage. To achieve better efficiency or higher power, turbine blade tip clearance has to be controlled. Attempts to address blade tip clearance problem were not applicable as designs were bulky and complex which required excessive modification on the turbine hardware and design. The goal of this study is to design, analyze and develop a low-cost and compact actuator system which is capable of controlling the tip clearance up to 0.25mm at elevated temperatures. Actuator will be positioned between inner and outer shrouds of the casing to force the inner shroud radially away from the blades during transients, and allow it to come back towards the blades when casing reaches operating temperature to decrease the tip leakage during steady state.

Different actuator designs have been studied and finite element analysis solutions have been obtained for deflection and stress. Low cycle fatigue life of the actuator has been estimated via Coffin-Manson criterion. An experimental setup has been designed and fabricated to validate the simulation results. Furthermore, since actuator will be subjected to wear at elevated temperatures due to mechanical loading and vibrations in the gas turbine, friction and wear behavior of candidate actuator materials has to be investigated. High temperature scuffing combined with rapid oxidation can lead to failures and dramatic reductions service life. Therefore, another experimental setup has been developed to conduct friction and wear tests of the candidate actuator materials, i.e. Nickel and Cobalt based superalloys Haynes 25, 188 and 214. The tests have been conducted at 20, 200,400 and 540 °C. Overall, the results indicated that the compact actuator can achieve 0.25 mm tip clearance reduction leading to 1% efficiency increase for 880 startup cycles.

## ÖZET

Endüstriyel gaz türbinleri ve uçak motorlarında, türbin kanadı ile sabit gövde “stator” arasında bırakılan boşluk, türbin güç ve verim kaybının en önemli sebeplerinden biridir. Endüstriyel gaz türbinlerindeki sıcaklığa bağlı genleşmeler ve uçak motorlarında manevralar sırasında gerçekleşen rotor esnemeleri sebebiyle, hesaplanan maksimum esneme / genleşme değerleri göz önüne alınarak türbin kanadı ile stator arasında güvenli bir boşluk bırakılması zorunludur. Halbuki; 150MW’lık bir gaz türbininde, türbin kanadı genleşmeler ve esnemeler sonrası eski konumuna geri döndüğünde kalan boşluk her 1 mm’de motor veriminde %4’e varan kayıplara yol açmaktadır. Türbinden daha fazla verim ya da daha yüksek güç çıkışı elde edebilmek için, bahsedilen radyal boşluğun kontrol edilmesi gerekmektedir. Kanat ucu boşluğundan oluşan verim kaybının azaltılması amacı ile bir çok çalışma yapılmıştır. Ancak, varolan yöntemler pahalı olup, türbin tasarımı üzerinde büyük değişiklikler gerektirmektedir. Bu tip çözümler çok yer kapladıklarından mevcut sistemlere uygulanmaları mümkün görünmemektedir. Bu çalışmanın amacı, endüstriyel gaz türbinlerinde, türbin kanadı uç boşluklarının en aza indirilmesi için, aşırı yüksek sıcaklıklarda çalışabilecek ve konumu kontrol edilebilir, güvenilir, az yer gerektiren ve böylece mevcut motorlara entegre edilebilecek bir eyleyici (actuator) sisteminin geliştirilmesidir. Eyleyici sabit gövde de bulunan iç ve dış kuşak parçaların arasına yerleştirilecektir. Böylece, eyleyici, iç kuşak parçayı gerektiğinde kanatlara doğru, radyal yönde itip çekerek boşluk kontrolünü sağlayacaktır. Bu çalışma kapsamında, farklı eyleyici tasarımları üzerinde analizler yapılmıştır. Uygun simulasyon programlarıyla farklı tasarım ve durumlar için sonlu elemanlar analizi çözümleri stres ve deplasman değerleri için elde edilmiştir. Coffin-Manson yöntemiyle, eyleyicinin düşük çevrim yorulma ömrü hesaplanmıştır. Simulasyon sonuçlarını doğrulamak için bir deney düzeneği tasarlanmış ve üretilmiştir. Ayrıca, eyleyici, gaz türbinin çalışma koşullarında, mekanik yükler ve titreşimlerden dolayı, yüksek sıcaklıkta aşınmaya

maruz kalacaktır. Bu tür etkiler, malzemenin servis ömürünü önemli ölçüde azaltabilmektedir. Bu yüzden, eyleyicide kullanılması düşünülen malzemelerin, yüksek sıcaklıktaki aşınma ve sürtünme davranışlarının incelenmesi gerekmektedir. Bu amaçla, aday eyleyici malzemeleri olan Haynes 25, 188 ve 214 süper alaşımlarının aşınma ve sürtünme testlerinin yapılabilmesi için farklı bir test düzeneği daha tasarlanmıştır. Aşınma ve sürtünme testleri, 20, 200, 400 ve 540 °C’ de yapılmıştır. Genel olarak sonuçlar eyleyicinin 880 çevrim boyunca, 0.25mm’lik boşluk kontrolü yapabildiğini, başka bir deyişle verimi %1 arttırabildiğini göstermiştir.

## **ACKNOWLEDGEMENTS**

I would like to express my deep and sincere gratitude to my advisor Dr. Mahmut F. Aksit for his continuous support, practical advices and patience during the progress of this work. I am grateful to my committee members Dr. Serhat Yeşilyurt, Dr. Kürşat Şendur, Dr. Güllü Kızıldaş Şendur and Dr. Ilyas Kandemir for taking the time to read and comment on my thesis. I also would like to thank my friends Serdar Aksoy, Elif Hocaoglu, Fatih Tabak and Ertuğrul Çetinsoy for their helps and guidance during the course of my thesis. My sincere thanks to Umut Şen, Ali Arsal, M. Rafet Ozdemir, Muhsincan Şeşen, Yusuf Sipahi, Duruhan Özçelik and Alihan Kaya for their support and friendship. My deepest gratitude goes to my parents for their unflagging love and support throughout my life. This thesis would not have been possible without them.

## **TABLE OF CONTENTS**

CHAPTER 1.....	1
INTRODUCTION AND PROBLEM STATEMENT .....	1
1.1 OVERVIEW ON GAS TURBINES.....	1
1.1.1 COMPRESSOR.....	1
1.1.2 COMBUSTOR.....	2
1.1.3 TURBINE.....	3
1.2 PROBLEM DEFINITION – TURBO MACHINERY BLADE TIP CLERANCE ISSUE.....	4
 CHAPTER 2.....	 7
2.1 LITERATURE ON BLADE TIP CLEARANCE CONTROL CONCEPTS .....	7
2.2 LITERATURE ON HIGH TEMPERATURE FRICTION AND WEAR.....	10
2.2.1 FRICTION AND WEAR BEHAVIOR AT HIGH TEMPERATURES.....	10
[400°C-599°C] .....	10
2.2.2 FRICTION AND WEAR BEHAVIOR AT VERY HIGH TEMPERATURES [600°C-799°C] .....	17
2.2.3 FRICTION AND WEAR BEHAVIOR AT ULTRA-HIGH TEMPERATURES (800°C AND BEYOND) .....	20
 CHAPTER 3.....	 23
TRIBO-TESTING OF CANDIDATE ACTUATOR.....	23
3.1 SLIDING WEAR RIG.....	23
3.1.1 SLIDING WEAR RIG DESIGN SPECIFICATIONS .....	24
3.1.2 MEASUREMENTS AND CORRECTIONS .....	27
3.1.2.1 Dynamic Friction Coefficient Estimation: .....	27
3.1.2.2 Calibration of Measurement errors:.....	27
3.1.2.3 Wear Coefficient Estimation: .....	29
3.1.3 SENSORS AND DATA ACQUISTION:.....	29
3.1.3.1 Load Cell: Noise cancellation and data acquisition.....	29
3.1.3.2. Thermocouple:.....	31
3.1.3.3. On-off Switch: Counter .....	31
3.1.4 FRETTING WEAR TEST RIG .....	32
3.2 FRICTION AND WEAR CHARACTERISTICS OF CANDIDATE ACTUATOR MATERIALS (H25, H188, H214) AGAINST HASTELLOY X.....	33

3.2.1 .MATERIALS AND TEST PROCEDURE.....	33
3.2.2 TEST RESULTS.....	34
CHAPTER 4.....	40
DESIGN AND ANALYSIS OF THE HIGH TEMPERATURE ACTUATOR .....	40
4.1 MATERIAL SELECTION .....	40
4.2 COMPACT ACTUATOR DESIGN .....	43
4.3 ANALYSIS OF DIFFERENT ACTUATOR DESIGNS .....	45
4.3.1 Actuator Design A: .....	45
4.3.1.1 Boundary Conditions.....	46
4.3.1.2 Simple Plate Analysis of the Actuator Design A .....	48
4.3.1.2.1 Effect of the design parameters on maximum stress and displacement : .....	49
4.3.1.3 Finite element analysis of the actuator Design A: .....	54
4.3.2 Actuator Design B: Actuator with Bellow Cross Section.....	57
4.3.2.1 Boundary Conditions:.....	60
4.3.2.2 Results: .....	61
4.4 LOW-CYCLE FATIGUE LIFE ESTIMATION OF THE ACTUATOR DESIGN B..	67
CHAPTER 5.....	70
ANALYSIS AND DESIGN VALIDATION .....	71
5.1 ACTUATOR TEST RIG DESIGN AND TEST PROCEDURE .....	71
5.2 CONTROLLER DESIGN .....	74
5.2.1 Proportional Integral Derivative Control (PID).....	74
5.2.2 Control Circuit and Microcontroller .....	75
5.3 FABRICATION OF THE ACTUATOR PROTOTYPE.....	78
CHAPTER 6.....	80
CONCLUSION .....	80
REFERENCES.....	82

## LIST OF TABLES

3.1	Wear Rig Specifications	25
3.2	Composition, Density and Vickers Hardnesses of Test Materials	33
4.1	Eligible Welding Types for Haynes 25, 188 and 214	42
4.2	List of Design Parameters	47
4.3	$\beta_1$ , $\beta_2$ and $\alpha$ values for Corresponding a/b ratios	48
4.4	Comparison of Analytical and Comsol Results	56
4.5	Mechanical Properties of Haynes 188 at 540 °C	59
4.6	Abaqus FEA Results for Design B under 5 bar Interior Pressure	61
4.7	Abaqus FEA Results for Design B under 10 bar Interior Pressure	62
4.8	Abaqus FEA Results for Design B under 10 bar Interior Pressure	64
4.9	Displacement Solutions Summary for Corresponding Interior Pressure	65
4.10	Fatigue life of the actuator Design B with different pressure inputs	69

## LIST OF FIGURES

1.1	Industrial Gas Turbine Stages: Compressor, combustor and turbine	1
1.2	Axial Flow Compressor Rotor Blades and Stator Vanes	2
1.3	A Combustion Model	3
1.4	A Combustion Can	3
1.5	Turbine Stage	4
1.6	Clearance Variation During Operating Cycle of a Jet Engine	5
1.7	Blade Tip Clearance Control Concept	6
2.1	NASA's First Generation ACC Test Rig	8
2.2	NASA's Second Generation ACC Test Rig	9
2.3	Shrink-fit Method	9
2.4	HTSMA ACC Concept	9
3.1	Wear Rig Components	24
3.2	Complete Picture of the Wear Rig	24
3.3	Working Principle of the Pneumatic Piston	25
3.4	Three Components of the Lower Specimen Holder	26
3.5	Multiple Wear Tracks	26
3.6	Test Section Installation Detail Through the Furnace Cover	27
3.7	Wheatstone Bridge Circuit Diagram	30
3.8	Amplifier and Low-pass Filter Circuit	31
3.9	Comparison of Filtered and Unfiltered Load Cell Output Signals	31
3.10	MiniLab 1008 10 Bit Data Acquisition Card	32
3.11	Fretting Wear Rig Components	32
3.12	Friction Coefficients of H25, H188 and H214 against Hastelloy X	34

3.13	Dimensionless Wear Coefficients of H25, H188 and H214 against Hastelloy X	35
3.14	Dimensionless Wear Coefficients of Hastelloy X against H25, H188 and H214	35
3.15	SEM Photomicrographs Showing Portions of Wear Tracks at 20K Magnificatio	36
3.16	Wear Tracks of H25, 188 and 214 at 540°C via Optical Microscope	38
3.17	Material Transfer at the Wear Track of H25 and H214	39
4.1	Elastic Modulus of Candidate Materials at Several Temperatures	40
4.2	Tensile Strength of Candidate Materials at Several Temperatures	41
4.3	Yield Strength of Candidate Materials at Several Temperatures	41
4.4	Oxidation Depth of Candidate Materials at Elevated Temepatures	42
4.5	Top View of the Actuator	43
4.6	Cross Section of the Pressurized Actuator	44
4.7	Actuator Position in the Gas Turbine	44
4.8	Analysis Section	45
4.9	Dimensions of the Actuator Design A	46
4.10	Boundary Conditions of the Actuator	46
4.11	Force Acting on the Sheet	47
4.12	Boundary Conditions for the Mathematical Model	48
4.13	Required Liquid Pressure in order to Get 0.25mm Displacement vs a/b ratio	50
4.14	Maximum Stresses with 0.25mm Displacement vs Sheet Thickness	51
4.15	Required Liquid Pressure in order to Get 0.25mm Displacement vs Thickness	52
4.16	Maximum Stress vs Sheet Thickness	52
4.17	Required Liquid Pressure in order to Get 0.25mm Displacement vs Width	53
4.18	Maximum Stress vs Sheet Width	54
4.19	Displacement Distribution over the Plate	55
4.20	Stress Distribution over the Plate	55
4.21	Design B Dimensions	57
4.22	Design B Front View	57

4.23	Dimensions of the Design B in Detail	58
4.24	Seam Welding Locations between the Cells	58
4.25	Fluid Inlet Position on the First Cell of the Array	59
4.26	Boundary Conditions	60
4.27	Abaqus Displacement Results for 5 Bar Interior Pressure	61
4.28	Abaqus Stress Results for 5 Bar Interior Pressure	62
4.29	Abaqus Displacement Results for 10 Bar Interior Pressure	63
4.30	Abaqus Stress Results for 10 Bar Interior Pressure	63
4.31	Abaqus Displacement Results for 20 Bar Interior Pressure	64
4.32	Abaqus Stress Results for 20 Bar Interior Pressure	65
4.33	The Trend of Total Displacement Against Interior Pressure	66
4.34	Low Cycle Fatigue Life Curve for Actuator Design B	69
5.1	Actuator Test Rig Components	72
5.2	Isometric View of the Actuator Test Rig	72
5.3	Pressurized Air's Path From the Pressure Regulator to the Actuator	73
5.4	PID Controller with Error Feedback and 2 Degrees of Freedom	75
5.5	Electronic Control System	76
5.6	Schematic Design of the Control Circuit	77
5.7	Welding Locations of the Actuator	78
5.8	Actuator Connection Detail	78

## NOMENCLATURE

$a$	Acceleration
$a$	Length of the sheet
$b$	Width of the sheet
$D$	Ductility
$E$	Modulus of elasticity
$F_f$	Frictional force
$F_i$	Inertial force
$H$	Hardness
$k_p$	Proportional gain
$k_i$	Integral gain
$k_d$	Derivative gain
$L$	Distance slid
$N$	Dead weight
$N_f$	Fatigue life
$q$	Interior fluid pressure
$Q$	Wear volume
$w$	Shroud weight
$W$	Total normal load
$t$	Thickness of the sheet

$T$	Temperature
$F_f$	Proportional gain
$F_i$	Proportional gain
$H$	Hardness

### Greek Symbols

$\alpha$	Constant specified by length/width ratio
$\beta_1$	Constant specified by length/width ratio
$\beta_2$	Constant specified by length/width ratio
$y_{max}$	Maximum deflection
$\sigma_{max}$	Maximum stress
$\sigma_{UTS}$	Ultimate tensile strength
$\varepsilon_a^{el}$	Elastic strain amplitude component
$\varepsilon_a^{pl}$	Plastic strain amplitude component
$\varepsilon_a$	Strain amplitude
$\varepsilon_a^{pl}$	Plastic strain amplitude component
$\varepsilon_a$	Strain amplitude
$\mu$	Friction Coefficient

**CHAPTER 1**  
**INTRODUCTION AND PROBLEM STATEMENT**

**1.1 OVERVIEW ON GAS TURBINES**

Gas turbines or turbine engines come in a wide variety of shapes and sizes for different applications. Gas turbines are used in a variety of services from jet engines and simple mechanical drives to complicated gas lasers and supersonic wind turbines [1]. Typically, gas turbines can be sub grouped into two as aero-engines and industrial gas turbines. However, all types of gas turbines have some common components. Gas turbines consist of three main sections, namely; compressor, combustor and turbine (Figure 1.1) [2]. Although there are variations in design of these three sections between aero-engines and industrial gas turbines, their working principle is similar.

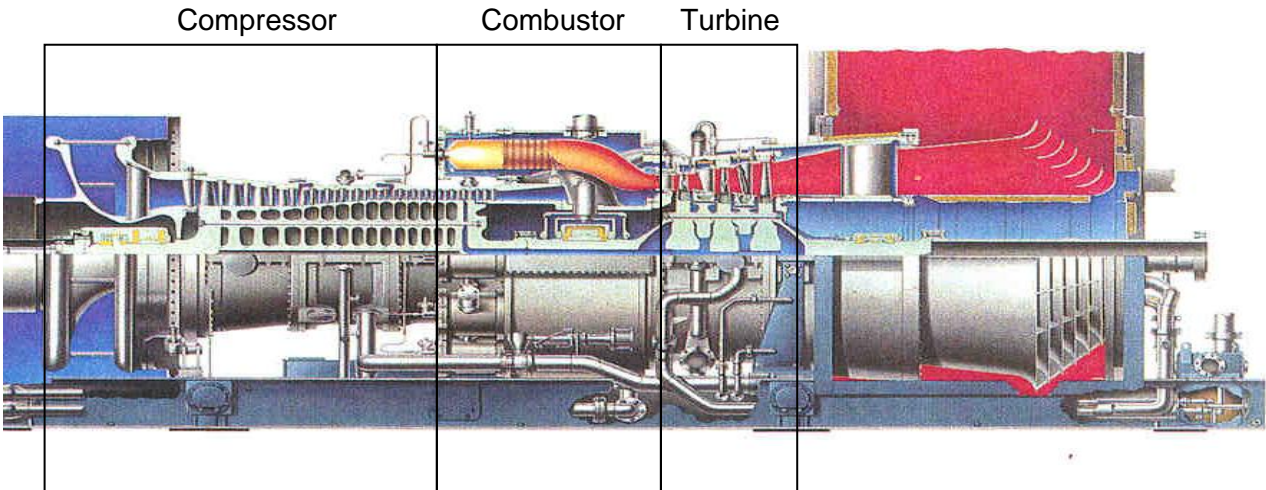
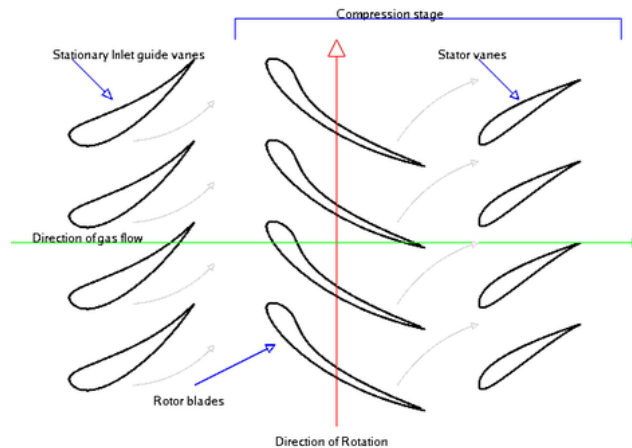


Figure 1-1 – Industrial gas turbine stages: compressor, combustor and turbine.

**1.1.1. COMPRESSOR**

Air taken from inlet is sucked continuously by the compressor, and compressed by a series of rotating blades. Compressors can have 19 or more stages of stator vanes and rotor blades. Stator vanes change the direction of the fluid to ensure that rotor blades face an incoming flow in optimum angle (Figure 1.2 [3]). As the air moves deeper and deeper through the compressor, its pressure and temperature increases. Pressure ratios are typically 12:1 for new industrial turbines where compression ratios of most recent aero-engines are 30:1 [1]. At

the exit of the final compressor stage air discharge temperature ranges from 370-390°C in a typical industrial/aero engine.



**Figure 1-2- Axial flow compressor rotor blades and stator vanes**

### **1.1.2 COMBUSTOR**

The function of the combustion chamber is to accept the air from the compressor and to deliver it to the turbine at the required temperature, ideally with no loss of pressure [4]. Fuel could be in gaseous or liquid state. Gases usually being natural gas, mostly methane, and butane. Liquids may range from highly refined gasoline through kerosene and light diesel oil to heavy residual oil [5]. Sprayed fuel from injectors mixes with the compressed air in the combustion chamber and then mixture is ignited by burners. Typically, firing temperature in the combustion chamber is around 2400-2480°F (1315-1360°C) (Figure 1.3 [1]). High-pressure and high-velocity combustion products expand through the nozzle towards the turbine stage.

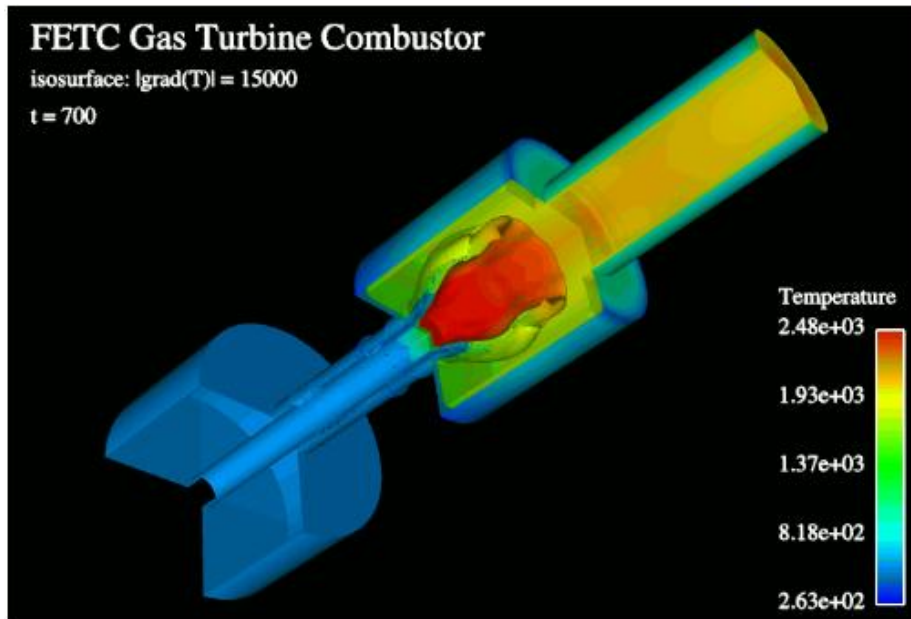


Figure 1.3 – A combustor model

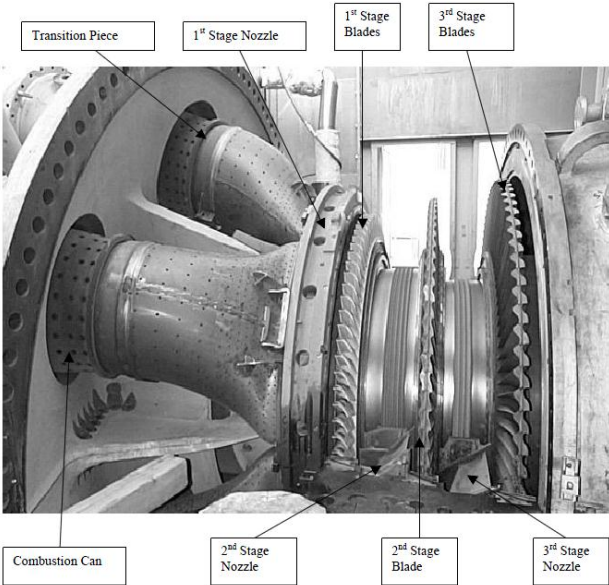


Figure 1.4 – Combustion can [4]

### 1.1.3 TURBINE

Turbine section generally consists of 3 stages of blades in an industrial gas turbine while number of the stages increase for jet engines (Figure 1.5 [4]). Turbine blades are circumvented by a segmented casing that includes inner and outer shrouds, seals and cooling channels. Combustion products have go through stages of turbine blades that are connected to

the same shaft with the compressor blades. Kinetic energy of the high velocity gas is exchanged for mechanical work when the gas flows over the blades and spins the turbine. The generated mechanical torque output is partially used to power the compressor. Output energy can be obtained in the form of shaft power, thrust and any combination of the two. Shaft power is used to drive generators in the industrial gas turbines to produce electricity where thrust is required in the aero-engines. Gas turbines have various applications in ships, tanks and trains.



**Figure 1.5 – Turbine stage**

**1.2 PROBLEM DEFINITION – TURBO MACHINERY BLADE TIP CLERANCE ISSUE**

During a typical startup cycle, industrial gas turbine blades expand faster than the bulky casing (shroud) when combustion gas starts flowing through the turbine section. Due to rapid radial expansion of the blades at the turbine section, blade-shroud tip clearance decreases during startup transient. Therefore, turbine designers have to leave some safe radial gap to prevent contact of blades to casing during start-up and shut-down periods. However, when casing circumventing blades reach to its thermal steady state, excessive amount of clearance remains until the shutdown. Similar blade-shroud interference problem occurs in aircraft engines due to rotor deflections during takeoff, landing and high g-force maneuvers. This phenomena is explained in Figure 1.6 [6] by presenting the clearance variance during flight of a jet engine. Gas turbine efficiency and power are very sensitive to turbine blade tip

clearance. It is reported that, each millimeter of turbine blade tip clearance leads to 4% efficiency loss in medium size industrial turbines [1].

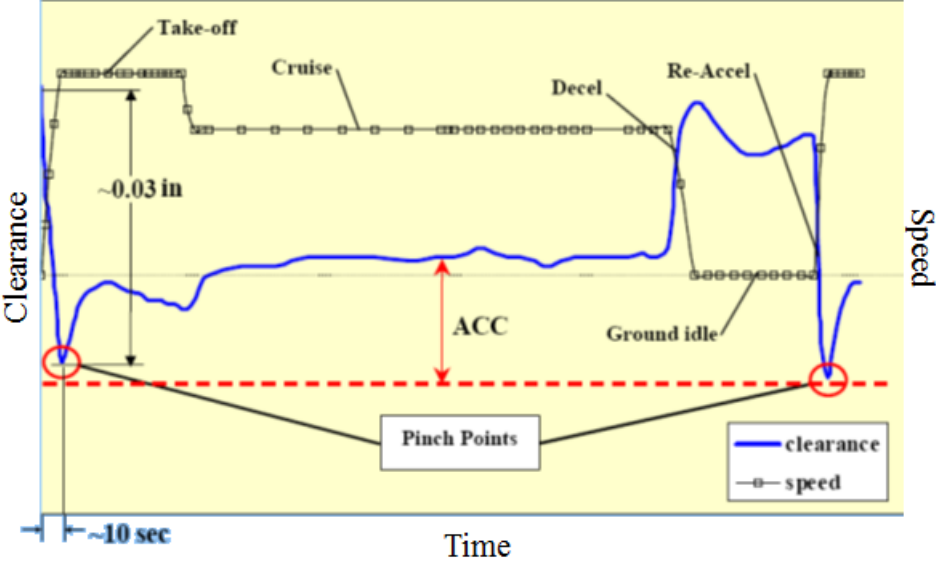


Figure 1.6 - Clearance variation during operating cycle of a jet engine

Tip clearance control has been a challenging problem since the development of the gas turbine engine. This due to the fact that clearance between blade tips and surrounding casing tends to vary primarily due to changes in thermal and mechanical loads on rotating and stationary structures [1]. For jet engines, tip clearance control becomes more challenging due to instant variations in the clearance with harsh maneuvers. However, frequency of clearance variations is relatively low in conventional gas turbines.

High temperature actuation systems are one of the major tools for tip clearance control at engine turbine section. Underlying mechanism of such actuation systems is based on forcing the shroud segments to radially move towards or away from the blades to control the tip clearance. Figure 1.7 [6] illustrates how an active clearance control (ACC) concept should work. In recent approaches, tip clearance is typically controlled by actuators that are positioned in the cavities between inner and outer shrouds. However, most such solutions are complex, expensive, bulky, and require serious modifications on the existing gas turbine hardware or design. Last but not the least, getting actuators working in turbine section is very difficult due to harsh environmental conditions like high temperatures and pressures. A

successful actuation system has to be robust, simple, require minimal modifications on the existing hardware and be able to work at elevated temperatures. A review of research work on active clearance control systems will be presented in the next chapter.

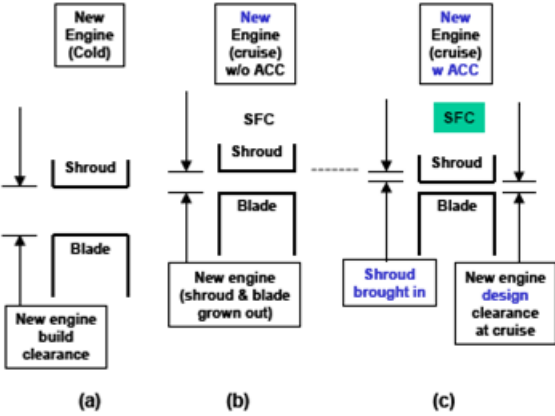


Figure 1.7 - Blade tip clearance control concept

This work aims to design and develop a novel high temperature actuator system that is applicable and retrofitable to most of the current operating turbines with no major modifications on the turbine design. Design goal is to control tip clearance up to 0.25mm actuation stroke that leads to possible 1% efficiency gain. Designing a flexible, controllable, economic actuator is challenging for high temperature applications. Exposure to the rapid oxidation combined with mechanical vibrations requires high temperature actuators to have good friction and wear resistance in order to provide sufficient service life. Therefore, as part of the development work some high temperature friction and wear tests have been conducted for candidate actuator materials.

## **CHAPTER 2**

### **BACKGROUND AND LITERATURE SURVEY**

#### **2.1 LITERATURE ON BLADE TIP CLEARANCE CONTROL CONCEPTS**

Active Clearance Control (ACC) and Passive Clearance Control (PCC) are two main methods that are being used for blade tip clearance control. ACC method can be divided into three sub-groups as Active Thermal Control, Active Mechanical Control and Active Pneumatic Control. Similarly, PCC method can be sub grouped as Passive Thermal Control and Passive Pneumatic Control.

In active thermal control systems, shroud systems are heated and cooled with the aid of air from compressor and fan, or through hot steam from some external steam source. Therefore, the tip clearance can be controlled based on expansion and shrinkage of the shroud. Turbine manufacturers began using active thermal control at late 70s [7-9]. However, due to its physics and nature, active thermal control has slow response time, provides only a limited amount of clearance control, and in some cases requires some external steam generation system. To improve the method, more appropriate materials and geometries needs to be used. Studies by Ciokajlo [10] and Paprotna et. al. [11] can be named as some of the significant works about this method. On the other hand, passive thermal systems rely on material properties and engine operating temperatures to match rotor and stator growth levels. This method is applicable to be used in smaller engines. Carpenter et al. [12] describe a system which combines stator materials with different coefficients of thermal expansion to allow faster growth of the shroud at lower temperatures to better match the centrifugal growth of the rotor. However, selective use of materials with different thermal expansion rates may not be applicable at elevated temperatures as most of such materials do not have oxidation and wear resistance properties to match actual engine challenge.

The working principle of an active pneumatic control system is based on using high-pressure air generated by the compressor to force stator to move in the radial direction [13]. This method may lead to a drop in the overall efficiency, since some of the compressor air is used for actuations. Moreover, such systems can fail due to high cycle fatigue. Catlow et. al.'s [14] work can be given as an example of such systems. Similarly, passive pneumatic control systems also work with compressed air. They may also use hydrodynamic effects [15]. Concepts of floating shroud segments [16] and blade tip cooling air discharge fall in to this

category [17]. However, robustness issues exist as floating segments may get stuck on each other under gravity loading.

Active mechanical control systems maintain the tip clearance by means of hydraulic, electro-mechanic or magnetic actuators. Actuators are positioned within the suitable cavities of the casing in order to move the shroud radially towards or away from the blade to reduce the leakage through the blade tip [18]. Majority of the active mechanical control concepts have been studied by NASA [19]. First generation of active mechanical control concepts aimed to get feedback from the segmented shrouds with fast response time [20]. A test rig (Figure 2.1) has been built to measure the amount of leakage under the simulated pressure, 30 psig, and temperature, 30psig, conditions. In this rig, turbine blades are fixed and not rotating.

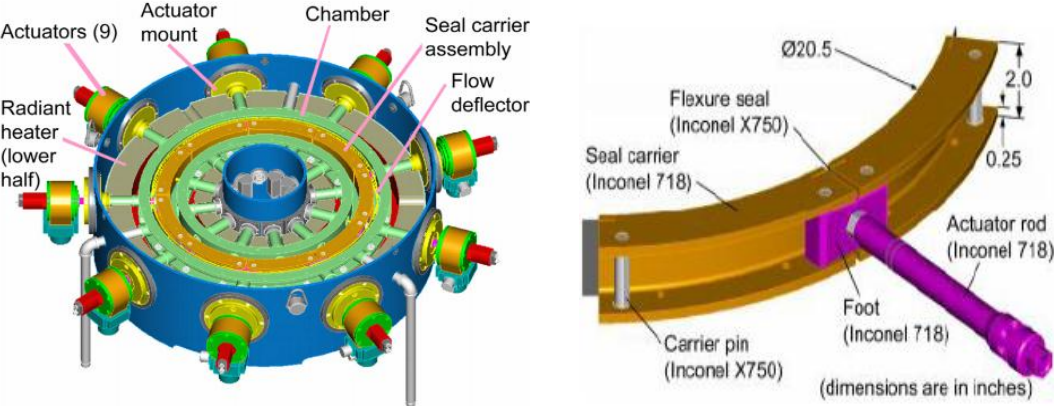


**Figure 2.1** – NASA’s first generation ACC test rig.

Their test results indicated that, closed loop position control has been achieved with 0.001” sensitivity in a desired response time. However, system does not properly on the operating temperature of the gas turbine, 1200 °F, and pressure, 120 psig. Second generation ACC system has been upgraded by Steinetz et. al. [21] to address this problem. Actuator rods have been replaced with servo-hydraulic actuators (Figure 2.2), and casing has been fortified to withstand 120 psig and 1200 °F. Actuator housings and exhaust port have been assembled with shrink-fit method (Figure 2.3). Closed loop position control has been achieved with 0.002” sensitivity under desired temperature and pressure conditions. Yet, these systems are bulky, heavy and complex raising engine applicability and reliability issues.

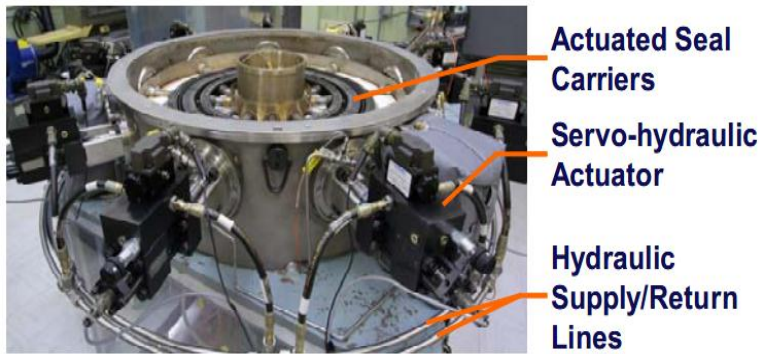


**Figure 2.2** - NASA's 2nd generation ACC test rig



**Figure 2.3** – Shrink-fit method

Another study has been conducted by using high temperature shape memory alloy (HTSMA) actuators which can recover its original shape by heat addition [22]. Classical shape memory alloys mainly composed of NiTi and are capable of working at 100 °C at most, due to the NiTi's low phase transition temperature. Pd, Pt, Au, Hf and Zr elements are doped into the composition and phase transition temperature of the alloys is increased [23]. HTSMA actuator is positioned below the fan bleed manifold and maintains the clearance gap by moving the shroud (Figure 2.4 [23]). Complexity, engine applicability and reliability issues still remain.

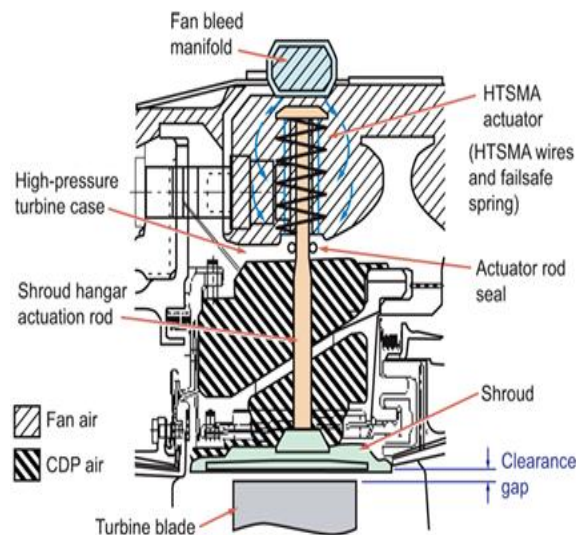


**Figure 2.4** – HTSMA ACC concept.

## **2.2 LITERATURE ON HIGH TEMPERATURE FRICTION AND WEAR**

In gas turbine applications, reduced wear resistance, low strength and rapid oxidation are the critical failure mechanisms that have to be addressed. Such factors are often observed at elevated temperatures and directly shorten the service life of the parts. The actuation and clearance control system that is proposed in this work is subject to pressure loads and mechanical vibrations that exist in the gas turbine. The actuator will be subjected to wear combined with oxidation at elevated temperatures. Therefore, a study of high temperature friction and wear properties of available materials is needed. A group of tests for the candidate materials have been conducted in order to select the best candidate in terms of wear and oxidation resistance. Prior to the tests, related literature has been investigated, and findings have been summarized below to get a better understanding on friction and wear behavior, oxidation phenomena and test procedures at elevated temperatures.

There are comprehensive reviews by Sliney and Allam [24,25] which primarily focus on solid lubricants. In addition, their data belong to the tests conducted before 1991. Friction and wear behavior of carbon nitride coatings, hard coatings, ion-implanted metals, rubber and tire, are reviewed at [26-29] respectively. In addition, previous studies on the effect of surface texturing and tribo-corrosion of coatings are presented in references [30-31]. However a comprehensive literature survey enclosing up-to-date high temperature friction and wear data of various types of materials is not available in open literature. Below results of a recent literature survey on high temperature friction and wear data has been presented.

When operating temperatures are involved, the term “high” is rather relative. High temperature title may refer to different temperature ranges for different applications. The previous studies are grouped as “high”, “very high” and “ultra-high” temperature ranges. As presented here “high” temperature range covers 400-599°C, “very high” temperature range covers 600°C – 799°C, and “ultra-high” temperature range covers 800°C and beyond.

### **2.2.1 FRICTION AND WEAR BEHAVIOR AT HIGH TEMPERATURES [400°C-599°C]**

Lu et al. [32] studied sliding friction, wear and oxidation behavior of CeF<sub>3</sub> sliding against high speed steel (WISCr4V) and stainless steel (1Cr1 8Ni9Ti). Tests were conducted

with 0.5 m/s sliding speed, 39,2 N dead-weight, and within the temperature range of room temperature to 700°C. After the tests, it is stated that, CeF<sub>3</sub> compact-steel couples shows poor friction and wear properties at elevated temperatures. Above 500°C, the dominant wear mechanism is oxidation that leads to severe wear with the contribution of reactions among iron-oxides and steels. To improve the friction and wear performance, Lu added 10% silver in volume to the CeF<sub>3</sub> compact and used “HasteAlloyC” as the counter surface material and reported that silver is effective to reduce friction and wear up to 300°C due to protective solid film formation on worn surfaces [33]. John et. al. [34] investigated the characteristic of mixture of composite WS<sub>2</sub> and CaF<sub>2</sub> films with 1µm thickness that were grown on steel substrates and TiN coated steel substrates with pulsed laser deposition technique. In the wear track, film has reacted to form oxides like CaO and sulfates like CaSO<sub>4</sub> that provides lubricious behavior. Friction coefficient value of 0.15 at 500°C is obtained from the tests.

Jianxin et al.[35] worked on Al<sub>2</sub>O<sub>3</sub>/TiB<sub>2</sub>/SiC ceramic composites and observed the effects of different amounts of SiC whiskers both on friction and wear behavior against cemented carbide at temperatures up to 800°C. The material is produced by using colloidal and ultrasonic processing techniques. The test rig is linear reciprocating tribometer and tests were conducted under both air and nitrogen atmosphere for 1 hour under 25 N normal load. At the end of the tests, it has been observed that fracture toughness and hardness increases with increasing volumetric amount of SiC in the composite up to %30 and both relative density and flexural strength has decreased. Friction coefficient and wear rates have decreased with increasing amount of SiC content for different atmospheres. The wear mechanism of the composite is abrasive for temperatures below 400°C. The friction coefficient is almost stable up to 400°C for both atmospheres.

Ouyang et. al. [36] worked on friction and wear behavior of low pressure plasma sprayed ZrO<sub>2</sub>-BaCrO<sub>4</sub> (ZB) composite coating at high temperatures up to 800°C and benchmarked the results with the partially stabilized zirconia (YPSZ). At relatively low temperatures, below 200°C, ZB coating exhibits high friction coefficient against sintered Al<sub>2</sub>O<sub>3</sub> and wear rate that is worse than YPSZ, however, its trend changes after 300°C. At elevated temperatures, friction coefficient gradually reduces and mild wear regime occurs due to formation and transformation of BaCrO<sub>4</sub> films. Moreover, Ouyang et. al.[37] worked on ZrO<sub>2</sub>(Y<sub>2</sub>O<sub>3</sub>) matrix composites friction and wear behavior with different amounts of CaF<sub>2</sub> and Ag against alumina balls. The aim of the study is finding the optimum amounts of CaF<sub>2</sub> and Ag in weight to minimize the friction and wear rates at the whole temperature range. Ouyang

et. al. mentioned that adding only  $\text{CaF}_2$  without silver provides poor friction and wear performance at low temperatures. With the presence of silver in the composite higher than 20% in weight lowers the friction and wear coefficients below  $400^\circ\text{C}$ . 35wt. % Ag and 30 wt. %  $\text{CaF}_2$  ( $\text{ZrO}_2(\text{Y}_2\text{O}_3)$ -30 $\text{CaF}_2$ -35Ag) exhibits the best tribological performance in the whole temperature range. Ouyang et. al. [38] also tested the tribological performance of 0.2mm thick low-pressure plasma sprayed (LPPS) and 0.3mm thick laser-assisted hybrid sprayed (LPHS)  $\text{ZrO}_2$ - $\text{Y}_2\text{O}_3$  ceramic coatings. It is observed that, friction and wear behavior of  $\text{ZrO}_2$ - $\text{Y}_2\text{O}_3$  are highly dependent on temperature. At low temperature, friction and wear of the LPHS  $\text{ZrO}_2$ - $\text{Y}_2\text{O}_3$  coatings is improved by laser irradiation due to the reduced pores, high hardness and highly adhesive bonding in contrast to the LPPS coating. Ouyang et. al.'s [39] another study is about the effect of  $\text{BaCrO}_4$  content and sintering temperature on friction and wear performance of  $\text{ZrO}_2(\text{Y}_2\text{O}_3)$ - $\text{BaCrO}_4$  composites. Additional  $\text{BaCrO}_4$  slightly increases the tribological performance of the coating at elevated temperatures. Composite sintered at  $1100^\circ\text{C}$  exhibits the lowest friction coefficient and best wear resistance than over  $1050^\circ\text{C}$ ,  $1150^\circ\text{C}$  and  $1300^\circ\text{C}$ . Ouyang et. al.'s [40] another study is on the friction and wear of  $\text{Al}_2\text{O}_3$  coating sliding on a similar material. Researcher reported that, friction and wear of the coating below  $400^\circ\text{C}$  are low, however above  $400^\circ\text{C}$ , friction coefficient increases where the wear resistance increases due to the change in dominant wear mechanism from mild to severe. Ouyang et. al. [41], also tested tribological performance of  $20\mu\text{m}$  thick cathodic arc ion-plated (V,Ti)N coatings up to  $700^\circ\text{C}$ . Below  $400^\circ\text{C}$ , tribo-chemical reaction is the dominant wear mechanism. Wear debris generally contains  $\text{V}_2\text{O}_5$  type tribo-oxides. It is reported that, oxide layers containing thermally oxidized  $\text{V}_2\text{O}_5$  type platelets on the tracks significantly increases friction performance. Ouyang et. al. [42] experimented (LPPS)- $\text{Al}_2\text{O}_3$  coatings and  $\text{ZrO}_2(\text{Y}_2\text{O}_3)$  matrix composites with different amount of additives as  $\text{BaF}_2$ ,  $\text{CaF}_2$ , Ag,  $\text{Ag}_2\text{O}$ ,  $\text{Cu}_2\text{O}$ ,  $\text{BaCrO}_4$ ,  $\text{BaSO}_4$ ,  $\text{SrSO}_4$  and  $\text{CaSiO}_3$  up to  $800^\circ\text{C}$ .

Yao-hui et. al. [43] studied on friction and wear behavior of Al-12Si/C/ $\text{Al}_2\text{O}_3$  hybrid composites at different test temperatures from 25 to  $400^\circ\text{C}$ . Four different Al based composites are focused in the experiments as monolithic Al-12Si alloy, 4 vol% C/Al-12Si, 12vol%  $\text{Al}_2\text{O}_3$ /Al-12Si and 4vol% C/12vol%.  $\text{Al}_2\text{O}_3$ /Al-12Si. There are three different aims of these experiments as observing effect of the test temperature, effect of volume fraction of  $\text{Al}_2\text{O}_3$  that varies from 0 to 20% with constant 4% C volume and effect of carbon fiber volume fraction varies from 0 to 6% C with fixed 12%  $\text{Al}_2\text{O}_3$ . Experiments are done with pin-on-disc tribometer and GCr15 Bearing Steel is used as counter surface.

Lopez et. al. studied [44] on tribological performance of zirconium nitride (ZrN) coatings deposited by magnetron-sputtering ion plating process on medium carbon steel (AISI 1045). The study also includes a performance comparison between ZrN coated and uncoated AISI 1045 surfaces. Counter surface is alumina ( $\text{Al}_2\text{O}_3$ ) and tests are done at 25,400 and 700°C. It is noted that, at low temperatures, ZrN coating shows an improved performance over uncoated surface. However at elevated temperature coating is worn out due to rapid oxidation and the friction coefficient is slightly higher than uncoated AISI 1045. Metal oxides' presence (i.e. Zr,  $\text{Fe}_x\text{O}_y$ ,  $\text{Mo}_x\text{O}_y$ ) plays an important role in the chemical reactions at 400 and 700°C that leads to an abrasive action on the coating surface.

Polcar et. al.[45] compared the friction and wear performance of TiN, TiCN and CrN at elevated temperatures. When sliding against 100Cr6 ball, friction coefficient increases with temperature for TiN and TiCN coatings. However, for CrN, friction coefficient reaches its minimum value at 500°C. Plastic deformation leads to mild wear for temperature below 400°C when sliding against  $\text{Si}_3\text{N}_4$ . TiN and TiCN coating perform a better wear resistance than CrN by a factor of 20-80 and above 300°C, oxidation occurs on all coatings. Polcar et. al, [46] investigated the CrN coatings sliding against 100Cr6,  $\text{Si}_3\text{N}_4$  and  $\text{Al}_2\text{O}_3$  up to 500°C. Polcar et. al. concluded that, oxidation occurs above 300°C and coating wear is very low when sliding against 100Cr6 however significant transfer of the ball material to the coating occurs. CrN- $\text{Al}_2\text{O}_3$  performs lowest friction at 500°C due to the protective oxide film formation. For CrN- $\text{Si}_3\text{N}_4$  couple, friction decreases with temperature while wear rate increases. Dominant wear mechanism is reported as polishing wear for whole temperature range. Polcar et. al.[47] added some different carbon contents to CrN. Chromium-Carbon-Nitride(CrCN) coatings were deposited on to steel substrates by cathodic arc evaporation method. CrCN coatings are tested against  $\text{Al}_2\text{O}_3$  and  $\text{Si}_3\text{N}_4$  balls. Researcher concluded that, highest wear rates are observed at 400 °C C and at higher temperatures wear resistance is improved.

Li et. al. [48] investigated the effect of the amount of  $\text{MoS}_2$  on nickel based composites containing sulfide and observed the mechanic and friction and wear behavior up to 600°C. It is noted that the optimum  $\text{MoS}_2$  amount for the best tribological performance is 12% wt for all temperatures. To enhance the preceding study on nickel based composites [48], Ji et. al. [49] has doped Ag,  $\text{MoS}_2$  and  $\text{CeO}_2$  into the nickel based composite by powder metallurgy to acquire lubrication over a wide temperature range. It is mentioned that adding Ag provides reduced friction up to 400 °C and higher amount of Ag improves the wear

resistance. However Ji et. al. reported that, Ag is ineffective for higher temperatures. Ruijun et. al. [50] explored the friction and wear behavior of Ti-Cu doped carbonaceous mesophases (CMs) to enhance the friction and wear performance of CM lubricants. Ruijun reported that, transition metallic elements have a catalytic effect on graphitization of non-graphitic carbon materials. According to test results, carbon Ti-Cu doped CM provides a better friction and wear resistance than raw CM and also friction coefficient and wear rate tend to decrease with larger applied loads.

Zhang et. al. [51] electroplated hBN powders with Ni and tested the resulting Ni-Coated hBN particules as a high temperature wear-resistant solid lubricant on 1Cr18Ni9Ti stainless steel. The counter surface is selected as  $\text{Si}_3\text{N}_4$  and tests were conducted with a ball-on-disk tribometer up to  $800^\circ\text{C}$ . It is mentioned that, above  $300^\circ\text{C}$ , dominant wear mechanism was mild adhesive wear, coating softened and debris transfer to counter surface increased. To lower the high friction coefficient of chromium-nitride(CrN) coatings. Bi et. al. [52] tested Ni-17Si-29.3Cr alloy against  $\text{Si}_3\text{N}_4$  from R.T. to  $1000^\circ\text{C}$  with a ball-on-disk tribometer. Bi reported that, at temperatures below  $800^\circ\text{C}$ , wear rate remained constant around  $10^{-5}\text{mm}^3/\text{N.m}$  and wear mechanism is delamination.

Benoy et. al. [53] experimented Au-Cr coatings and reported that chromium could enhance the the adherence performance to avoid coating delamination at elevated temperatures. Laskowski et. al. [54] also studied on candidate foil bearing materials to identify new material combinations that could show better tribological performance than coupled Inconel X-750 (the current foil bearing material) at high temperatures. Following couples are tested at 25, 500 and  $800^\circ\text{C}$  as pin and disk materials respectively: “INCX-750 & INCX-750”, “MA956 & INCX-750”, “MA956-OX & INCX-750”, “INC909 & INCX-750”, “IN713CX & INCX-750”, “Rene'41 & INCX-750”, “MA956 & MA956”, “MA956-OX & MA956”, “MA956 &  $\text{Al}_2\text{O}_3$ ”, “INCX-75 &  $\text{Al}_2\text{O}_3$ ”. However there is no significant improvement observed with the new combinations that could replace the current foil bearing material, Inconel X-750 mates. DellaCorte et. al.[55-56], conducted tests at  $25^\circ\text{C}$ ,  $500^\circ\text{C}$  and  $800^\circ\text{C}$  on metal bonded chrome oxide coating with silver and  $\text{BaF}_2/\text{CaF}_2$  coating, PS300, which is the successor of PS200 coatings. A benchmark between PS300 and PS200 coatings is also presented. It is reported that, both coatings have similar wear rates at  $500^\circ\text{C}$  and most significant advantage of PS300 coatings over PS200 is its lower cost. DellaCorte et. al.[57], tested PS400 coatings in air, inert gas and vacuum environments and a benchmark with

PS304 coatings is presented. It is noted that, PS400 exhibits far lower friction coefficient than PS304 at 500°C.

Barrau et. al. [58] experimented the effect of initial hardness and temperature on friction behavior of tempered martensitic tool steel. Up to 500 °C, oxides becomes thicker on the disc surface with increasing temperature and contribution to friction and wear performance of oxide layers becomes significant after 500 °C. Barrau et al. [59] investigated the effect of temperature, load and pin geometry on wear. Mating surfaces are double tempered martensitic steel (X38CrMoV5) and ferritic-pearlitic mild steel (AISI 1018). Researcher concluded that at elevated temperatures the formation of wear protective oxide layers increases and mentioned the temperature as the most effective parameter. On the other hand, he added that, load and pin geometry also have important roles on flow and bonding of wear debris.

Yang et. al. [60] performed sliding friction and wear tests for sintered ceramics as mullite alumina, silicon carbide and titanium diboride and rubbed them against in various combinations at 25, 500 and 1000°C. Yang et. al. observed the formation of turbofilms and their effect on friction and wear behavior of ceramics. His results indicate that turbofilm has a significant role on the wear behavior of ceramics. Below 500°C, poor adhesion of the film to the surface observed when specific wear rate is in the order of  $10^{-4}$  mm/N-m, Dense and adhesive turbofilm provides good protection for friction and reduces the wear rate. High Strength Steels (HSS) are often used in automotive industry, agricultural and mining equipments. Hardell et. al. [61], experimented the tribological performance of high strength boron steel (HSBS) with and without an Al-Si coating (25µm thick) against surface nitrided and untreated tool steels with different material compositions. Tests were conducted with 20N dead-weight and within the temperature range of 500-800°C. Hardell et. al. concluded that, plasma nitrided tool steel specimen has improved friction performance and provides a better wear protection against seizure and galling while rubbing against HSBS. Hardell et. al. [62] also stated that, with the contribution of oxidized wear debris, dominant wear mechanism is adhesive wear at all temperatures.

Taktak et al. [63], focused on the friction and wear behavior of duplex surface treated AISI 5210 and 8620 bearing steel rubbed against alumina balls at 25 and 500°C. Duplex treatment consists of thermo reactive diffusion (TRD) chromizing and plasma nitriding (PN). It is reported that Plasma nitriding process not only lowers the friction coefficient but also

enhances the wear resistances of both steels. In case of TRD chromized steels, abrasive wear and plastic deformation observed in both temperatures and at 500°C oxidation plays a major role. For duplex treated steels, polishing and oxidative mild wear are the dominant wear mechanisms at 25 and 500°C respectively. Consequently, duplex surface treatment (TRD+PN) shows a better wear resistance than TRD chromized surfaces. Arslan et. al.[64] studied the friction and wear characteristics of MoS<sub>2</sub>/Nb coatings up to 500°C and in air environment. At 500°C, coating is worn out due to rapid oxidation and third body formation. Wider wear tracks and higher debris amount on the coating are observed at both 300 and 500°C. Arslan et. al. mentioned that, MoS<sub>2</sub> coating provided lowest friction coefficient and wear rates at 100°C and lower temperatures and it is appropriate for industrial applications below 100°C with atmospheric conditions.

Mann et. al.[65] , studied friction and wear behavior of hard deposits such as stellite, surface treatment such as nitriding and thermally sprayed coatings such as D-gun sprayed and plasma sprayed coatings on valve spindle material X20CrMoV121 at 550°C . Mann et. al. concluded that, chromium carbide coating by plasma spraying is superior to all other coatings. Kumar et. al. [66] investigated the friction and wear performance of the hexagon wrappers of the fuel-sub assemblies (15Cr-15Ni-2Mo) that are subjected to high frictional force during the removal of the fuel sub-assemblies from the reactor. Tests were conducted with a pin-on-disk linear reciprocating type tribometer with sodium test vessel in hot trapped sodium at 200 and 550°C. Relatively low friction coefficient values were acquired during the tests which are sufficient at fuel handling temperature and met the design requirements. Friction coefficient stabilized after 100 m of rubbing distance due to the sodium chromite film formed prior to the tests and get removed with the progress of the test. Kumar added that adsorption and lubrication mechanism could be the reason for low friction coefficient in sodium environment.

Barnick [67] et. al. tested the performance of various self-coupled materials lubricated with hydrocarbon feed gases under air, nitrogen and nitrogen-acetylene environments at 520°C. For metal alloys as AISI M50, 52100, 440C, 1018, K-Monel (500) and Hastalloy C276, friction coefficients less than 0.08 are measured Friction coefficients of less than 0.10 are measured for alumina, silicon nitride, tungsten carbide and zirconia in nitrogen-acetylene atmosphere. It is reported that, nitrogen-acetylene mixed environment is very effective to reduce friction and wear volume. Sawyer et. al. [68] studied vapor-phase lubrication of self-coupled M50 steel in combined rolling and sliding contacts at 540°C in nitrogen-acetylene

atmosphere. Sawyer reported that friction coefficients as low as 0.01 are measured for 2m/s rolling speed, 10cm/s sliding speed and 100N dead weight in the mixed atmosphere. Moreover, friction coefficients are above 0.35 for pure nitrogen atmosphere and scuffing is observed. Other tests conducted on vapor phase lubrication and showed an excellent friction and wear performance could be listed as, high temperature (above 500°C) lubrication of silicon nitride( $\text{Si}_3\text{N}_4$ ) in sliding and rolling contact with solid carbon, decomposition of carbonaceous gas streams and pyrolyzed carbonaceous gases[69,70], vapor phase lubrication of nickel-based superalloys and effect of early phosphate vapor at 500°C [71] and sliding and rolling wear tests of  $\text{Si}_3\text{N}_4$  simulated under turbine engine exhaust environments at 500°C to observe lubrication performance of  $\text{C}_2\text{H}_2$  admixture[72]. Wang [73], applied PS304 coating on steam turbine governor valve lift rods under operating condition at 540°C for 150 hours. Test results indicate that, coating has a good oxidation resistance and coating surface is well protected with a layer of discontinued glaze film contains NiCr,  $\text{Cr}_2\text{O}_3$ , Ag,  $\text{BaF}_2/\text{CaF}_2$ .

## **2.2.2 FRICTION AND WEAR BEHAVIOR AT VERY HIGH TEMPERATURES [600°C-799°C]**

Xue et. al. [74] studied the effect of temperature over friction coefficient for Hastelloy C with  $\text{CeF}_3$  solid lubricant. Above 700 °C, performance of coating increased due to oxide  $\text{CeO}_2$  formation which reduced friction around 0.15 to 0.20. At elevated temperatures Hastelloy C had negative wear losses due to the transferred film formation on its worn surface which contributed to wear resistance significantly. Lu et.al. [75] tested, the performance of  $\text{CeF}_3$  solid lubricant on friction and wear resistance. The plane orientation and the oxidation of  $\text{CeF}_3$  are the two main factors affecting the friction reduction up to 0.15. The transfer film formed on solid lubricant contributed to minimize wear rate at high temperatures. Lu et. al. [32] studied sliding friction, wear and oxidation behavior of  $\text{CeF}_3$  sliding against high speed steel (WISCr4V) and stainless steel (1Cr1 8NiTi). It could be stated from the test results that, there is a strong correlation between oxidation of  $\text{CeF}_3$  compact with lubricity at 600 and 700°C. Lu et al. [33], added 10 vol.% silver to the  $\text{CeF}_3$  compact to investigate the effect of silver in friction and wear behavior. Test results infer that, adding silver in content, improves

the friction performance at all temperatures except 400°C slightly. At 700°C, silver and CeF<sub>3</sub> perform a synergetic effect on reducing friction.

John et. al.[76] investigated the lubricity of CaSO<sub>4</sub>, BaSO<sub>4</sub> and SrSO<sub>4</sub> films that were grown with pulsed laser deposition technique on steel substrates and TiN coated steel substrates. John et. al. reported that each coating exhibited a low friction coefficient that is smaller than 0.25 for the tests conducted at 600°C. It is observed that when the furnace turned off and temperature began to fall, friction coefficient began to increase significantly beginning from 500°C down to room temperatures. Because the onset of the lubricious behavior for the coating is approximately 500°C Jianxin et al. [35] studied Al<sub>2</sub>O<sub>3</sub>/TiB<sub>2</sub>/SiC<sub>w</sub> ceramic composites and observed the effects of different amounts of SiC whiskers both on friction and wear behavior against cemented carbide in both air and nitrogen. The test results for shows that, there is a gradual increase in friction at 600°C and above in air atmosphere, in contrast, friction coefficient tends to increase significantly in nitrogen atmosphere. Although, wear rates apparently double for temperatures above 600°C, they are in acceptable range, more specifically in the order of 10<sup>-6</sup> mm<sup>3</sup>/N-m. Ouyang et. al state that at 600°C, delamination becomes the dominant wear mechanism for LPPS ZrO<sub>2</sub> coatings rubbing against sintered alumina balls [36], silver addition in content is effective for spark-plasma-sintered ZrO<sub>2</sub>(Y<sub>2</sub>O<sub>3</sub>)- CaF<sub>2</sub>-Ag composites at low temperatures but this effect is lesser at elevated temperatures above 400°C [37] and delamination for due to subsurface crack propagation and abrasive wear for LLPS ZrO<sub>2</sub> coatings are the dominant wear mechanisms at 600 and 700°C respectively [76]. Ouyang et. al. added that, laser assisted hybrid sprayed(LPHS) ZrO<sub>2</sub>-Y<sub>2</sub>O<sub>3</sub> ceramic coatings wear resistance and friction performance is not improved by laser irradiation at 600°C and above, in contrast to lower temperatures [38], wear rate and friction continuously improved after 400°C in small amounts for ZrO<sub>2</sub>(Y<sub>2</sub>O<sub>3</sub>)-BaCrO<sub>4</sub> and matrix composite with highest BaCrO<sub>4</sub> content(50 wt%) is most effective in reducing friction and wear at all temperatures [39], and abrasive wear is the dominant wear mechanism above 700°C for LPPS Al<sub>2</sub>O<sub>3</sub> coatings[40]. Ouyang et. al. [42] reported that, for ZrO<sub>2</sub>(Y<sub>2</sub>O<sub>3</sub>)-Al<sub>2</sub>O<sub>3</sub>-50MoS<sub>2</sub> composite coatings, addition of 50wt. % MoS<sub>2</sub> reduces the friction coefficient to very low values however severe wear is observed due to the degradation of MoS<sub>2</sub>.

Hardell et. al. [61] reported that friction coefficient of Boron steel-tool steel 1 couple's initial friction is high at 500-600°C but tends to decrease at higher temperatures. Moreover, boron steel-tool steel3 couple shows scuffing tendency at 600°C.

Li et. al. [48] reported that, low friction values as small as 0.2 are obtained while rubbing Ni-Cr-W-Al-Ti-MoS<sub>2</sub> composite against Al<sub>2</sub>O<sub>3</sub> and low wear rate is observed while rubbing against nickel-iron-sulfide alloys. Li et. al. [49] states that, addition of CeO<sub>2</sub> to the Ni-Cr-W-Al-Ti composite enhances the friction and wear performance up to 600°C due to formation of smooth glaze layer. Furthermore, additional Ag in content improved the friction and wear rate at temperatures up to 400°C. As a result, nickel-base composite with multi lubricants, better tribological performance acquired compared to previous study [48].

Zhang [51] reported that Ni-Coated hBN provided good friction and wear resistance while rubbing against Si<sub>3</sub>N<sub>4</sub> balls in all test temperatures however wear rate increased mildly at 600-800 °C due to decreasing of strength in coating. Polcar et. al. [47], mentioned that, for CrCN coatings only polishing of the initial ball and coating surfaces are observed with negligible wear rate while rubbing against both Al<sub>2</sub>O<sub>3</sub> and Si<sub>3</sub>N<sub>4</sub> as counter interfaces.. Staia et. al.[78] experimented the high temperature friction and wear behavior of nitrided AISI D2 tool steel prior and after PAPVD coating up to 600°C. At 600°C, oxidation and reduce of the mechanical strength of the substrates lead to fracture and delamination of the films. Formation of third-body also contributes to wear.

Bi et. al. [52] states that, the wear rate of the Ni-17.5Si-29.3Cr alloy almost remained constant around 10<sup>-5</sup> mm<sup>3</sup>/N-m. It is also reported that, Ni based alloys and coatings, Mo<sub>2</sub>Ni<sub>3</sub>Si/NiSi, Cr<sub>13</sub>Ni<sub>5</sub>Si<sub>2</sub>, show excellent wear and oxidation resistance at 600°C [79-81].

DellaCorte et. al. [55,56], reported that, moderate wear is observed at 650 °C for both PS200 and PS300 foil bearing coatings with a wear rate of about 7x10<sup>-4</sup> mm<sup>3</sup>/N-m and friction coefficients ranged from 0.23 to 0.31 while rubbing against Inconel X750 pins. Another work on foil bearings focused on tribological performance of ion diffused Cu-4Al coatings on foils at 25 and 650<sup>0</sup>. Evaluations were done through start-stop tests via air bearing test rig by Malcolm et. al.[82]. Journal wear rate is generally higher with the Cu-4Al coated bearing than the uncoated one at 650°C. Also, it is observed that friction coefficient for Cu-4Al is 19% higher than the uncoated bearing. Malcolm concludes that further studies have to be done in order to understand the friction and wear behavior of the Cu-4Al better at high temperatures. DellaCorte et. al.[57] reported that, friction coefficients are almost the same for both PS304 and PS400 coatings, however PS400 shows a better wear performance while rubbing against Inconel X750 pins at 650°C. Zabinski et. al. [83] tested the solid lubricant, PbMoO<sub>4</sub>, in oxidizing environments. Zabinski reported that , PbMoO<sub>4</sub> films deposited by

pulsed laser method are lubricious at 700°C with a friction coefficient of 0.35. However, high friction leads material to failure at room temperature. Test results of X38CrMoV5 steel-A1018 couple by Barrau et. al. [58], indicate that at 700°C, localized oxidation of X38CrMoV5 pin with rich chromium and molybdenum oxides is observed and metal-oxide mixed zone is gradually transformed in a compact layer of oxide debris. Lopez et. al. [44] states that uncoated AISI 1045 has about %10 lower friction coefficient (0.62) than ZrO<sub>2</sub> coated substrate (0.69) and both coated and uncoated substrates are worn out due to severe oxidation at elevated temperatures.

### **2.2.3 FRICTION AND WEAR BEHAVIOR AT ULTRA-HIGH TEMPERATURES (800°C AND BEYOND)**

Jianxin et al. [35] stated that, at 800°C, dominant wear mechanism is oxidation for air atmosphere and adhesion and diffusion dominates for nitrogen atmosphere for Al<sub>2</sub>O<sub>3</sub>/TiB<sub>2</sub>/SiC<sub>w</sub> composites with different amount of SiC<sub>w</sub> whiskers. Friction coefficient and wear rates decreased with increasing amount of SiC<sub>w</sub> content for both atmospheres. Friction coefficient in nitrogen atmosphere increases dramatically where in air it gradually decreases.

Laskowski et. al. [54] reported that Rene 41 shows a little performance over other foil bearing material candidates however, no significant improvement observed over current foil bearing material, Inconel X-750. Benoy et. al. [53] states that, at 800°C, Au coatings failed by delamination in the wear track and coating transfer from disk to pin is observed and precluded for more reliable measurements. Also, chromium in Au-Cr coatings could enhance the adherence performance to avoid coating delamination at elevated temperatures.

Heshmat et.al. [85], tested several coatings for foil bearings such that Korolon 800, Korolon 1350A and Korolon 1350B. Counterface disks were coated with a plasma sprayed PS304, hard chrome, dense and Korolon 1350B. The friction coefficient of Korolon 800 against PS304 was around 0.1-0.2 at 416°C. Due to a localized wear or degradation of the pad coating friction coefficient increased to 0.3-0.4 to the end of experiment. During the high temperature tests with hard chrome coated disks, severe cracking was observed in thick coating. During startup and shutdown Korolon 1350B coated surfaces exhibit quick drop in coefficient of friction from 0.2 to 0.08 due to the change in the degree of conformity between the pad and the disk surface. Korolon 800 wore mostly at locations of the highest contact

pressure. No measurable wear detected when the disk coated with Korolon 1350A subjected to the pad coated with Korolon 800 and the lowest friction coefficient is measured as low as 0.06 during startup and shutdown. The wear performance of Korolon 1350A was observed superior to dense chrome and PS304 which caused moderate pad wear. At 810°C, Korolon 1350A survived and performed well except start-stop cycle where slight burnishing is noticed.

Ouyang et. al. [36] reported that, at elevated temperatures, friction coefficient gradually reduces and mild wear regime occurs for ZrO<sub>2</sub>-BaCrO<sub>4</sub> (ZB) composite coating due to formation and transformation of BaCrO<sub>4</sub> films. Moreover, Ouyang et. al. [37] claimed that, ZrO<sub>2</sub>(Y<sub>2</sub>O<sub>3</sub>)-30CaF<sub>2</sub>-35Ag composite sintered at 950 °C is the most effective on reduction of friction and wear at 800°C and lower temperatures. Ouyang et al. mentioned that, at 800°C average friction coefficient remains to a value of  $0.97 \pm 0.1$  together with substantial noise and vibration during wear process[9], best friction and wear performance for ZrO<sub>2</sub>(Y<sub>2</sub>O<sub>3</sub>)-BaCrO<sub>4</sub> coatings is obtained by ZrO<sub>2</sub>(Y<sub>2</sub>O<sub>3</sub>)-50%wtBaCrO<sub>4</sub> as 0.42 and  $1.3 \times 10^{-5}$  mm<sup>3</sup>/N-m respectively[39]. Miyoshi et. al. [86]'s results for Al<sub>2</sub>O<sub>3</sub>/ZrO<sub>2</sub> (Y<sub>2</sub>O<sub>3</sub>) pins indicate that, wear coefficient of the pins are generally increase at elevated temperatures. For 65.07Al<sub>2</sub>O<sub>3</sub>/3.69ZrO<sub>2</sub> (1.24Y<sub>2</sub>O<sub>3</sub>) of eutectic composition, has the minimum wear rate at 800°C and has a relatively low friction coefficient, 0.43, when sliding against B<sub>4</sub>C.

Hardell et. al. [61] reported that, Al-Si coating on boron steel 1 is effective on reducing friction when rubbing against nitrided steel at 800°C. Plasma nitrided tool steel 2 has a similar friction performance with tool steel 1 and both of them show some scuffing tendencies at 800°C. Negative specific wear rates are measured for coated boron steels while rubbing against tool steel 2-3 due to the material transfer. DellaCorte et. al [84] mentioned that when Pt coated MoRe sliding against H188, dynamic friction in air atmosphere is generally lower than the Ar-H<sub>2</sub> atmosphere due to the formation of lubricious oxide layer in air. . Barrau et. al. [58] experimented the effect of initial hardness and temperature on friction behavior of tempered martensitic tool steel up to 950°C. It is observed that internal oxidation contributes to decohesion of pin debris and due to the degradation of mechanical properties at 950°C, 42HRC material has a viscous behavior.

Yang et. al. [60] performed sliding friction and wear tests for sintered ceramics as mullite alumina, silicon carbide and titanium diboride and rubbed them with each other in various combinations up to 1000°C. Yang also observed the formation of turbofilms and their effect on friction and wear behavior of ceramics. His results conveyed that turbofilm has a significant role on the wear behavior of ceramics. Dense and adhesive turbofilm provides

good protection for friction and reduces the wear rate. Bi et. al. [52] tested Ni-17Si-29.3Cr alloy against  $\text{Si}_3\text{N}_4$  from R.T. to  $1000^\circ\text{C}$  with a ball-on-disk tribometer. Bi reported that, above  $800^\circ\text{C}$ , wear rate began to increase rapidly due transformation of dominant wear mechanism to adhesion and oxidation.

Following the literature study, and considering the range of temperatures for a typical gas turbine shroud interface, it has been decided that Cobalt/Nickel superalloys provide a good compromise between oxidation and wear resistance. Therefore, Haynes 25, Haynes 188 and Haynes 214 have been selected as candidate materials for further study.

## **CHAPTER 3**

### **TRIBO-TESTING OF CANDIDATE ACTUATOR**

A custom test rig has been designed to characterize high temperature friction and wear behavior of the actuator materials. The system has been designed in such a way that tribopair test section can be placed in a high temperature furnace. Depending on the setup material limits very high temperature test can be conducted using commercially available high temperature furnaces. While most tribotest systems remain limited to 800 °C, the presented system is capable of test temperatures up to 1200 °C. For temperatures beyond 800 °C, some special high temperature materials like Bohler H525 are used as the rig material. The presented system is capable of operating at 1Hz speed with 25 mm stroke. Force data are measured by a high precision load cell. Together with the normal load, horizontal force data are used to calculate friction coefficient at the end of a test. Test rig has been designed to be simple and easy to use. By offsetting lower specimen track location after each test, multiple wear tracks can be obtained from a single specimen. Moreover, test rig is modular, so the pneumatic piston in the system could be replaced by a vibrator or shaker to allow for high frequency fretting testing.

#### **3.1 SLIDING WEAR RIG**

Custom design wear and friction test rig is used to characterize wear and friction behavior of Haynes 25, Haynes 188 and Haynes 214 to 540 °C. The sliding contact between test samples is generated by pneumatic piston through linear actuation. Friction coefficient is calculated by measuring frictional force exerted on sample via high precision load cell integrated to the actuator assembly. On the other hand, wear coefficient values are acquired through weight loss measurements and Archard's equation. Weight of test samples are measured before and after each test to determine the amount of removed material.

### 3.1.1 SLIDING WEAR RIG DESIGN SPECIFICATIONS

As shown in Figure 3.1, the tribo test system is composed of pneumatic piston (1) , load cell (2), hinge (3), two AISI 304 push rods/pipes (4), upper specimen holder (5), lower specimen holder (6), lower rod fixer (7), pneumatic relay(8), on/off valve (9). Test rig's specifications are summarized in Table 3.1. A picture of the test system with external components is presented in Figure 3.2.

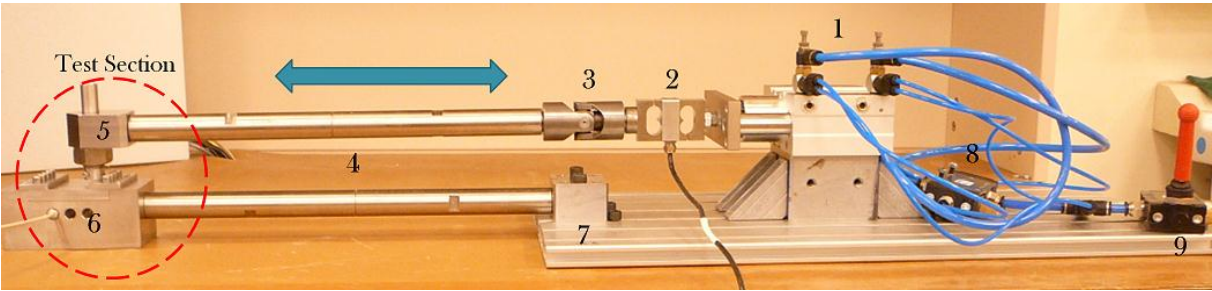


Figure 3.1 – Wear rig components

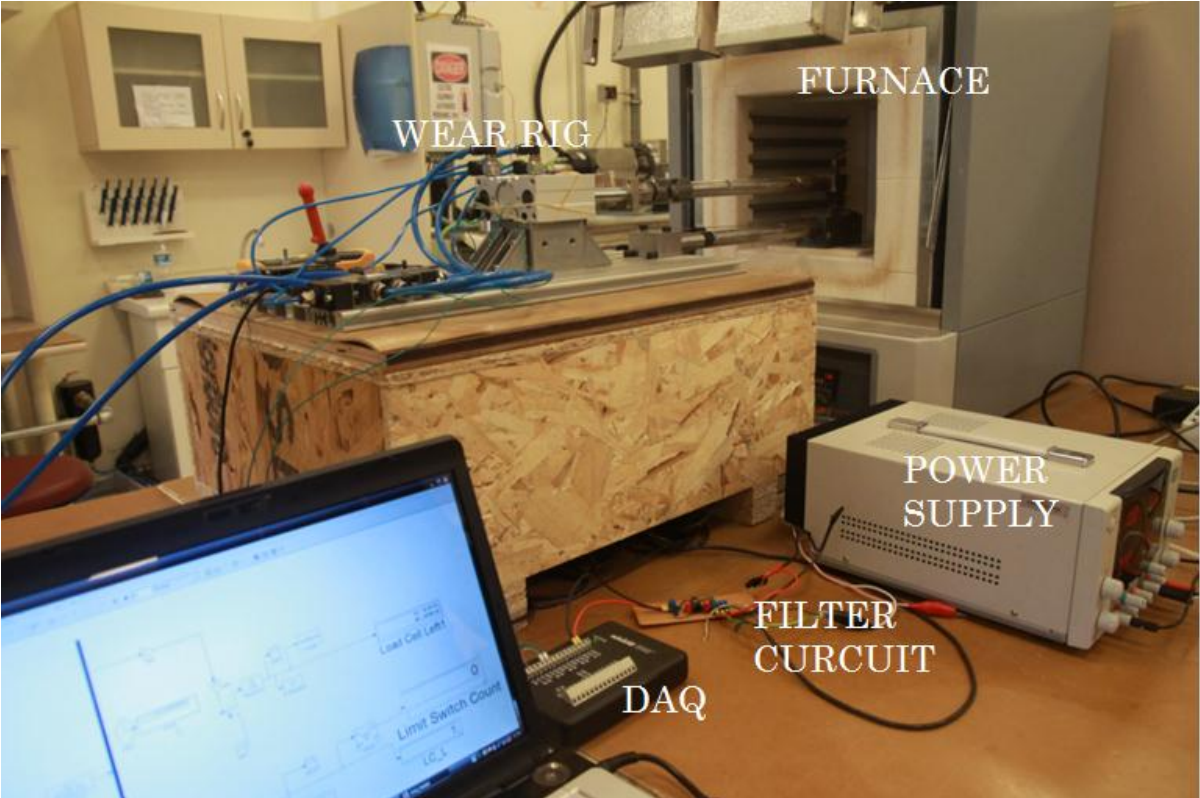
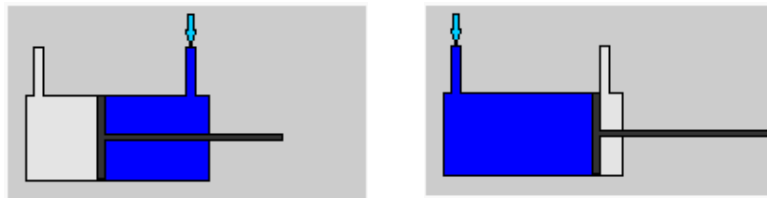


Figure 3.2- Complete picture of the wear rig

**Table 3.1 – Wear Rig Specifications**

<b>Wear Rig Type</b>	Linear Reciprocating
<b>Upper Specimen</b>	Flat Ended, Ball
<b>Lower Specimen</b>	Sheet Metal
<b>Temperature Range</b>	25-1250°C
<b>Max Speed</b>	1 Hz
<b>Stroke</b>	25 mm
<b>Load Range</b>	10-50N

To actuate the system on linear reciprocal axis, Mindman MCGB triple-guide pneumatic piston is used. Piston is excited by 6 bar air with a compressor, and is capable of exerting 500N with up to 5mm stroke. Stroke is mechanically reduced to 2.54mm (1”). As shown in Figure 3.2, piston has two input ports for pressurized air. The port on the right allows pressurized air in to the chamber to push the piston. When the piston reaches the mechanical stop pressure in the chamber increases. Then, with a pneumatic relay switching mechanism, air is diverted the left port to push the piston in opposite direction. To accelerate the cycle, fast exhaust valves are plugged into the ports. Speed of the piston is adjustable up to 2 Hz.



**Figure 3.3 - Working principle of the pneumatic piston**

An Omega LCM101-50 load cell is connected to the piston to measure the total frictional resistance exerted to the piston. Measured horizontal force data are transferred to the computer by means of a 20-channel data acquisition system, and monitored in an EXCEL

sheet. Horizontal force data are necessary to calculate friction coefficient values at the end a test. The procedure will be explained later. Load cell is capable of measuring up to 500 N.

AISI 304 push rod/pipe is connected to the load cell with a hinge. The push rod also acts as heat insulator due to its poor thermal conductivity and hollow/tubular construction. Required rod length to prevent temperature sensitive devices from deterioration (e.g. load cell), is determined as 380 mm through a simple finite element analysis.

Left side of the pipe is assembled with upper-specimen holder which applies 12.8 N to lower specimen horizontally due to its own weight. Test load can be calibrated by adding extra ring-shaped masses on the top, if needed. Upper specimen has 0.5 mm diameter and 10 mm length.

Lower specimen holder is positioned just under the pin and fixes the rectangular shaped sheet metal (25x50x0.025mm) as a counter surface to the pin. Lower specimen holder consists of three parts (Figure 3.4). The two parts on the top used for fixing the specimen and allows it to be positioned on the third part. There are eight positions defined by multiple screw holes. The first two parts can slide over the third, and can be fixed on any desired position by a set of screws (Figure 3.5). Therefore, it is possible to acquire multiple wear tracks from one specimen fixed at the lower side. Materials of upper and lower specimen holders and fittings are of same type, AISI 304, as to prevent jamming or loosening up of the parts due to different thermal expansion rates.

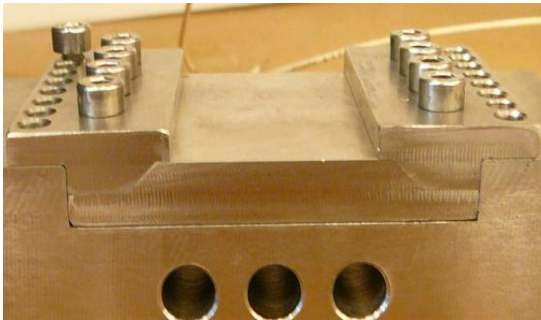


**Figure 3.4** – Three components of the lower specimen holder.

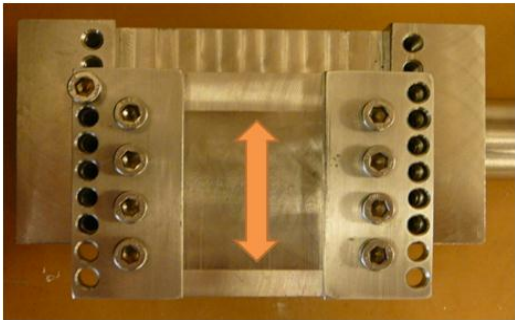


**Figure 3.5** – Lower specimen holder can slide to achieve multiple wear tracks from single specimen.

The lower specimen holder is anchored by a pipe which is identical to the pipe that is mentioned before and other edge of the pipe is connected to a metal block to make the lower specimen holder stand still.

System can be heated either by placing the specimen holders in a furnace and inserting connecting roads through holes in the lid (Figure 3.6), or by placing cartridge heaters into the lower specimen holder.

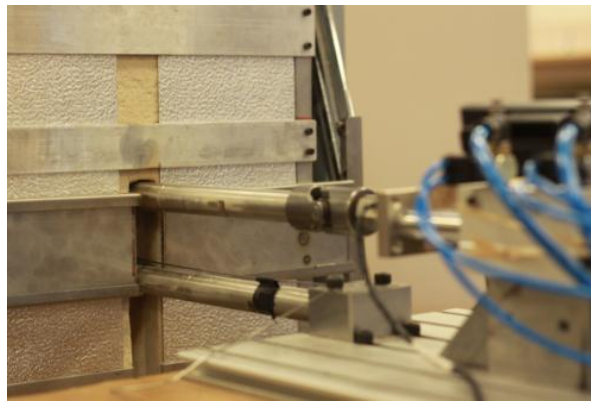


**Figure 3.6**– Test section is positioned in the furnace through access hole in the cover

### **3.1.2 MEASUREMENTS AND CORRECTIONS**

#### **3.1.2.1 Dynamic Friction Coefficient Estimation:**

To find the friction coefficient the simple friction equation is used. “ $\mu$ ” is the friction coefficient where “ $F_f$ ” is the friction force measured by load cell. “N” is the normal load applied on the sheet metal by dead weight.

$$\mu = F_f/N \quad (3.1)$$

#### **3.1.2.2 Calibration of Measurement errors:**

The inertial force generated and applied on load cell due to the acceleration will result in measurement errors. This undesired force can be estimated from Newtons Second Law if

nominal acceleration of the system is found. The stroke of the piston is known. The acceleration is calculated as follows:

$$0.5at^2 = x \quad (3.2)$$

$$a = 2x/t^2 \quad (3.3)$$

where a is acceleration, t is time and x is stroke. For t equals 0.5 s and x equals 0.025 m, the acceleration, a is,

$$a = 2 \cdot \frac{0.025m}{0.5^2s^2} = 0.2 \text{ m} \cdot \text{s}^{-2} \quad (3.4)$$

The inertial force due to this acceleration is calculated from Newtons Second Law as follows,

$$F_i = m * a = 3.05x0.2 = 0.61 \text{ N} \quad (3.5)$$

The measurements from the load cell are calibrated by using the inertial force found above as bias force to ignore it from friction coefficient estimation on the sample. This procedure is suitable for relative ranking of the materials as conducted here. Higher precision tests can be conducted at slower speeds to minimize inertial load effects.

### **3.1.2.3 Wear Coefficient Estimation:**

Wear coefficient values are calculated by Archard Equation.

$$K = \frac{QH}{WL} N \quad (3.6)$$

where K is the wear coefficient, H is the hardness of the material. Q,W and L are wear volume, total normal load and track length respectively.

The weight of the samples is measured by a precision balance with 0.0001 gram sensitivity before and after each test. The difference between the measurements will give the weight of the detached material from the specimen.

### **3.1.3 SENSORS AND DATA ACQUISITION:**

There are three major sensors in the wear rig: load cell, thermocouple and on/off switch. Load cell measures the friction force data, and outputs proportional potentials within the range of 0-30mV for 0-500N axial loads. K-type thermocouple is used to measure temperature of the lower specimen and an on/off switch is placed behind the pneumatic piston to calculate total distance slid from the number of cycles.

#### **3.1.3.1 Load Cell: Noise cancellation and data acquisition**

High precision Omega LCM101 load cell is used to measure friction forces. Load cell is capable of measuring axial force values within the range of -500 to 500N, and converts it to voltage proportionally to -30 to 30mV range. The conversion is facilitated by a Wheatstone Bridge circuit in the load cell (Figure 3.7). When the load cell is subjected to load, resistor x shown in Figure 3.7 adjusts itself and circuit outputs a corresponding voltage.

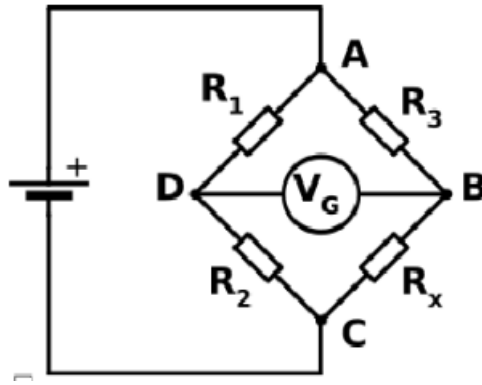


**Figure 3.7-** Wheatstone bridge circuit diagram

Although the underlying mechanism of the load cell is simple, differential output signals are noisy. There are two modes of noise that should be addressed. The first type is common mode noise which is conducted on all lines in the same direction. With an AC power supply line, for example, noise is conducted on both lines in the same direction. The second type is differential noise mode which is conducted on the signal (VCC) Line and GND line in the opposite direction to each other.

To minimize the common mode noise, INA101 high accuracy instrumentation amplifier is used. With the aid of the amplifier, output range of the load cell (-30 to 30mV) is amplified to 0-5V. The common mode noise is dramatically reduced after the amplification, thanks to INA101. The differential mode noise is reduced with the aid of a RC low-pass filter with 30Hz cut-off frequency. The complete picture of the custom design filter circuit is presented at Figure 3.8, and a benchmark of unfiltered and filtered output signal picture is shown in Figure 3.9. The outputs of the load cell are connected to the input terminal of the filter circuit and filtered outputs are connected to a 10bit data acquisition card, and then to the computer.

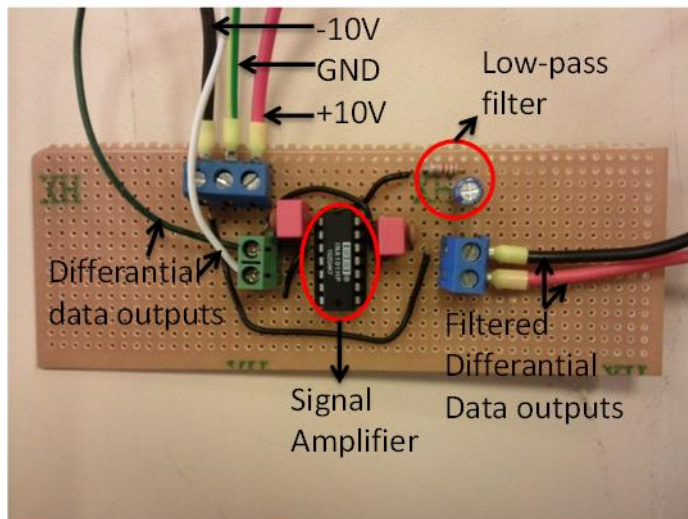


**Figure 3.8** -Amplifier and low-pass filter circuit



**Figure 3.9** – Comparison of filtered and unfiltered load cell signals via oscilloscope.

### 3.1.3.2. Thermocouple:

Although the furnace has its own built-in thermometer, in order to accurately measure sample temperatures an Inconel 600 coated K-type Ordell OM02 thermocouple is used. Junction of the thermocouple is positioned to the lower specimen. Temperature data is not recorded, but displayed through CEM DT612 thermocouple meter. Thermocouple is calibrated with two reference points as icy water (0°C) and boiling water (100°C). A -3°C offset is observed and compensated for both temperatures.

### 3.1.3.3. On-off Switch: Counter

To calculate the total distance slid, number of total cycles is counted by an on-off switch which is positioned behind the pneumatic piston. “Normally closed” and “common” terminals of the switch are subjected to +5V and GND respectively via the data acquisition card (Figure3.10). Before connecting to +5V terminal, a 2.2 Kohm resistor is used to reduce the current. At each cycle, the shaft of the piston hits the switch, and +5V is sent to the DAQ which increments the counter value in the SIMULINK model.

### 3.1.3.4. Data Acquisition Card and Software

A 10bit miniLAB 1008 data acquisition card is used to gather the data from the load cell and on/off switch. Card is connected to the PC via USB port, and Matlab/Simulink is used to control the incoming signals from the data acquisition card.



Figure 3.10 – miniLAB 1008 10 bit data acquisition card.

### 3.1.4 FRETTING WEAR TEST RIG

The linear reciprocating test rig is modular, so that the pneumatic piston in the system could be replaced by a pneumatic vibrator to conduct fretting wear tests as shown in Figure 3.11. Pneumatic vibrator is connected to a linear slide to allow cyclic motion in axial direction. Frequency of the cycles is calculated as 240Hz with accelerometer when 2bar air pressure is applied to the vibrator. Stroke is calculated as 200 $\mu$ m with coordinate measuring machine (CMM) from the wear tracks. Test procedure and other details are the same with the sliding wear test rig.

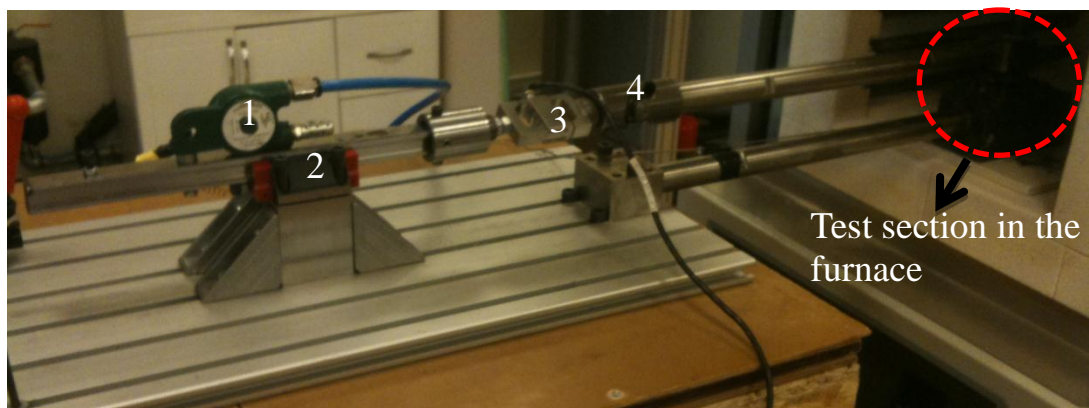


Figure 3.11 - Fretting wear rig is composed of pneumatic vibrator (1), linear slide (2), load cell (3), hinge (4).

### 3.2 FRICTION AND WEAR CHARACTERISTICS OF CANDIDATE ACTUATOR MATERIALS (H25, H188, H214) AGAINST HASTELLOY X

#### 3.2.1 .MATERIALS AND TEST PROCEDURE

Haynes 25, Haynes 188 and Haynes 214 sheets are tested against Hastelloy X pins. Rectangular sheets have the dimension of 45x15x0.3mm where the cylindrical pins have 5mm diameter and 20mm length. Micro-hardness of the test specimens are measured via Wolper Testor 2100 under 100gf load and are presented at Table 3.2 together with density and composition of the materials.

**Table 3.2** –Composition, density and Vickers hardness of test materials.

<b>Test materials wt% composition</b>	<b>Haynes 25</b>	<b>Haynes 188</b>	<b>Haynes 214</b>	<b>Hastelloy X</b>
Co	51	39	-	1.5
Ni	10	22	75	47
Cr	20	22	16	22
W	15	14	-	0.6
Fe	3	3	3	18
Mn	1.5	1.25	0.5	1
Si	0.4	0.35	0.2	1
C	0.10	0.10	0.05	0.10
La	-	0.03	-	-
B	-	0.015	0.01	0.008
Al	-	-	4.5	-
Zr	-	-	0.1	-
Y	-	-	0.01	-
Mo	-	-	-	9
<b>Density (kg/m<sup>3</sup>)</b>	9130	8980	8050	8220
<b>Hardness (HV)</b>	340	305	289	432

Prior to experiments, test specimens are cleaned with ultrasonic acetone bath for 10 minutes at 40KHz to get rid of any surface films and contamination. Then, cleaned specimens are weighed with a precision balance with 0.0001 gram sensitivity. The test setup is heated up to the desired temperature with the furnace for approximately 2 hours. Temperature of the test specimens are additionally measured via K-type thermocouples. After the tests, specimens are allowed to cool down slowly, and are ultrasonically cleaned and weighed again.

Wear measurements are typically obtained by weight loss measurements. At elevated temperatures, weight loss or gain is also possible due to rapid oxidation other than wear. To measure the loss or gain, another identical sheet specimen is also positioned in the furnace. Hence, weight loss/gain due to the oxidation is independently calculated and weight loss due to pure wear is calculated by adding or subtracting the weight loss/gain due to the oxidation. Corrected wear loss is then divided by density, distance slid, load and multiplied by the hardness to obtain dimensionless wear coefficient. Friction coefficient is calculated by measuring frictional force exerted on the sample via high precision load cell integrated to the actuator-connecting rod assembly. Additionally, surface structure and phase compositions of the worn surfaces are studied with Scanning Electron Microscopy (SEM) and Energy-Dispersive X-ray Spectroscopy (EDX) respectively.

**3.2.2 TEST RESULTS**

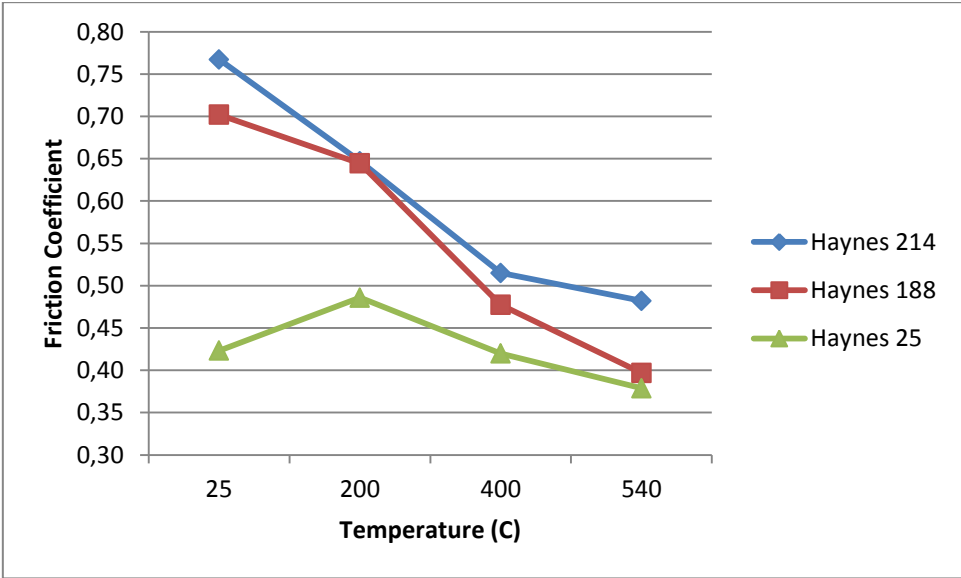


**Figure 3.12**– Friction coefficients of H25, H188 and H214 sheets against Hastelloy X pin.

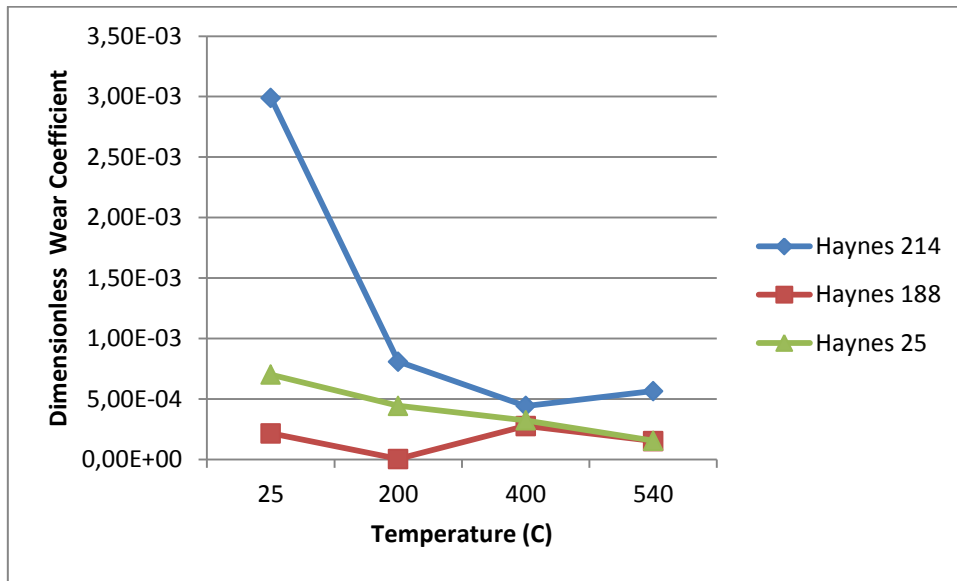


**Figure 3.13**– Dimensionless wear coefficients of H25, H188 and H214 sheets against Hastelloy X pin.

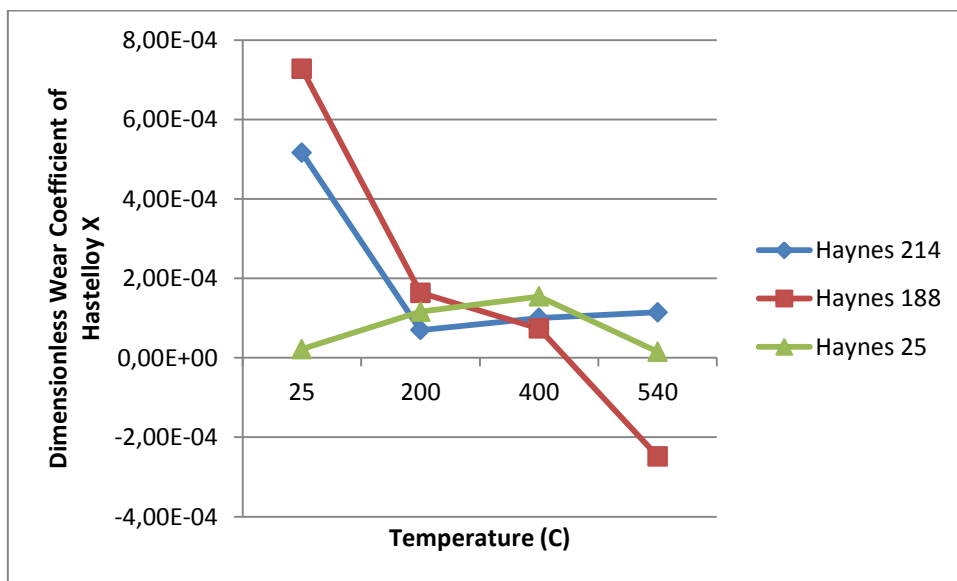


**Figure 3.14**– Dimensionless wear coefficients of Hastelloy X pins against H25, H188 and H214 sheets.

Results of the friction and wear tests are summarized in Figures 3.12 to 3.14. A set of scanning electron photomicrographs showing portions of wear tracks on sheet samples that belong to the tests conducted at 400 and 540 °C is presented in Figure 3.15. Haynes 25 has the lowest friction coefficient values for each test condition. Haynes 25 has friction and wear

coefficients of 0.42 and  $7.0E-4$  respectively at room temperature. Haynes 188 has a significantly higher friction coefficient as 0.70 but provides a better wear resistance, at  $2.1E-4$ . Haynes 214 has the highest friction and wear coefficients at room temperature as 0.76 and  $2.9E-3$  respectively.

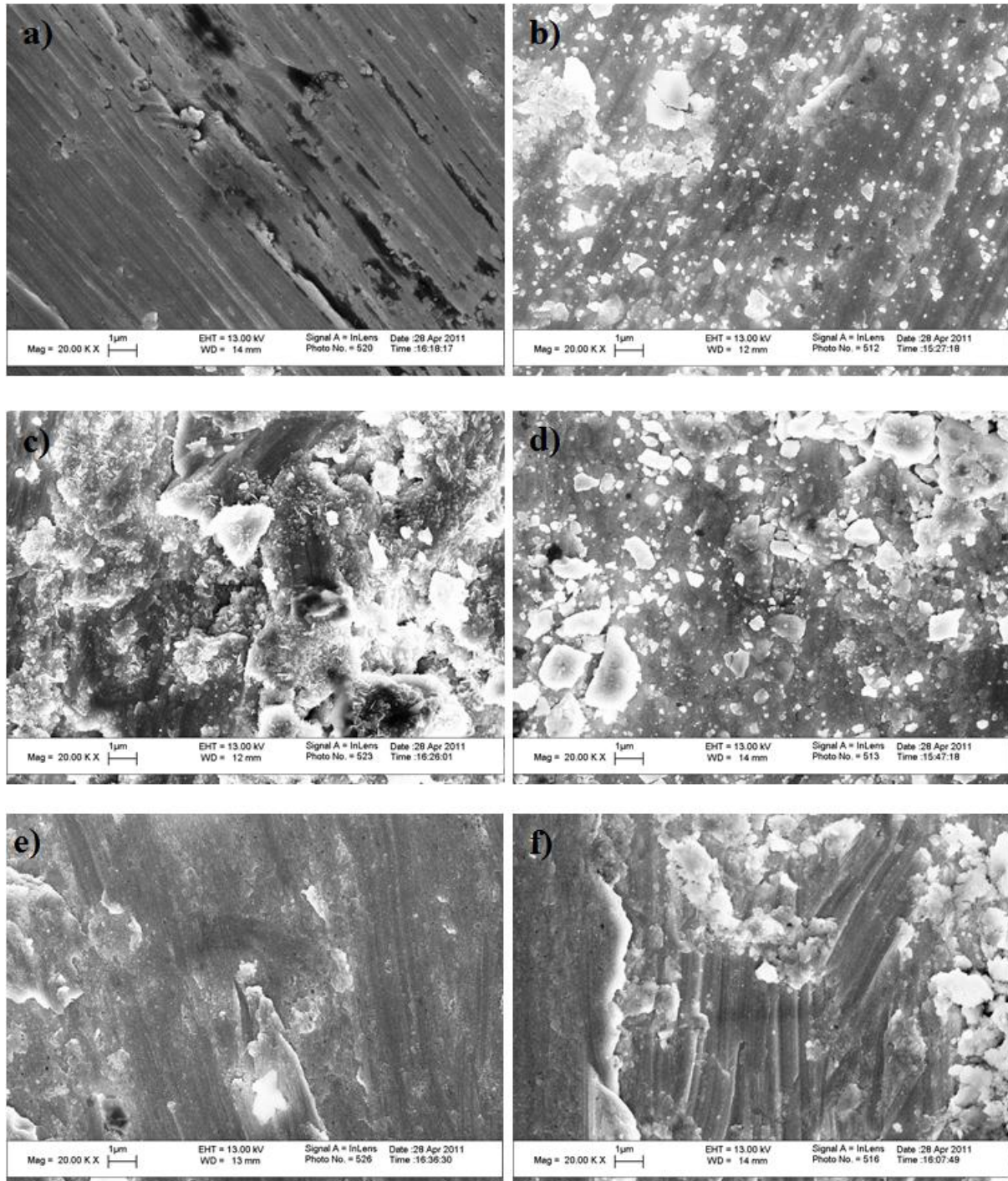


**Figure 3.15** – SEM photomicrographs showing portions of wear tracks with 20K magnification for a) Haynes 25, 400°C b) Haynes 25, 540°C c) Haynes 188, 400°C d) Haynes 188, 540°C e) Haynes 214, 400°C f) Haynes 214, 540°C.

Unlike other specimens, friction coefficient of Haynes 25 increases at 200 °C to the 0.486 with substantial noise and vibration. Haynes 188 and 214 have the same friction coefficient as 0.64. However, in contrast to Haynes 188's mild wear regime with a wear coefficient of 6.67E-6, wear behavior of Haynes 214 is more severe with wear coefficient in the order of 1E-3. The reason for low wear coefficient of Haynes 188 is probably due to the material transfer. Since the composition of the Haynes 188 and Hastelloy X are very similar, it is almost impossible to distinguish the excessive material over the wear track.

At 400 °C, friction coefficients tends to reduce with the test time for Haynes 25 and 214 where friction coefficient of Haynes 188 exhibited some minor variations. Haynes 25 has friction and wear coefficients as 0.42 and 3.2E-4 respectively. Friction coefficient of Haynes 188 reduces to 0.47 while wear rate slightly increases to 2.7E-4. Noise is higher for Haynes 214 at 400 °C than the tests at 200 °C. Substantial amount of nickel oxides are detected on the wear track. Oxide films enhance the wear resistance, and decrease wear coefficient to 4.4E-4.

At 540 °C, both Haynes 25 and 188 gained a bluish color on account of the intense cobalt-oxide formation as shown at Figure 3.16. In addition, significant amount of nickel, chrome and tungsten oxides are identified through EDX analysis. These oxides form a lubricious and protective layer on the wear track. Friction and wear coefficients drop to lower values than that of tests conducted at 400°C. Haynes 25 exhibits the lowest friction coefficient among all specimens in all tests at 0,38. Like Haynes 25, Haynes 188 have a relatively low friction coefficient at 0.40. Wear coefficients for Haynes 25 (Figure 3.12) and 188 decreases to 1.54E-4 and 1.51E-4 respectively.

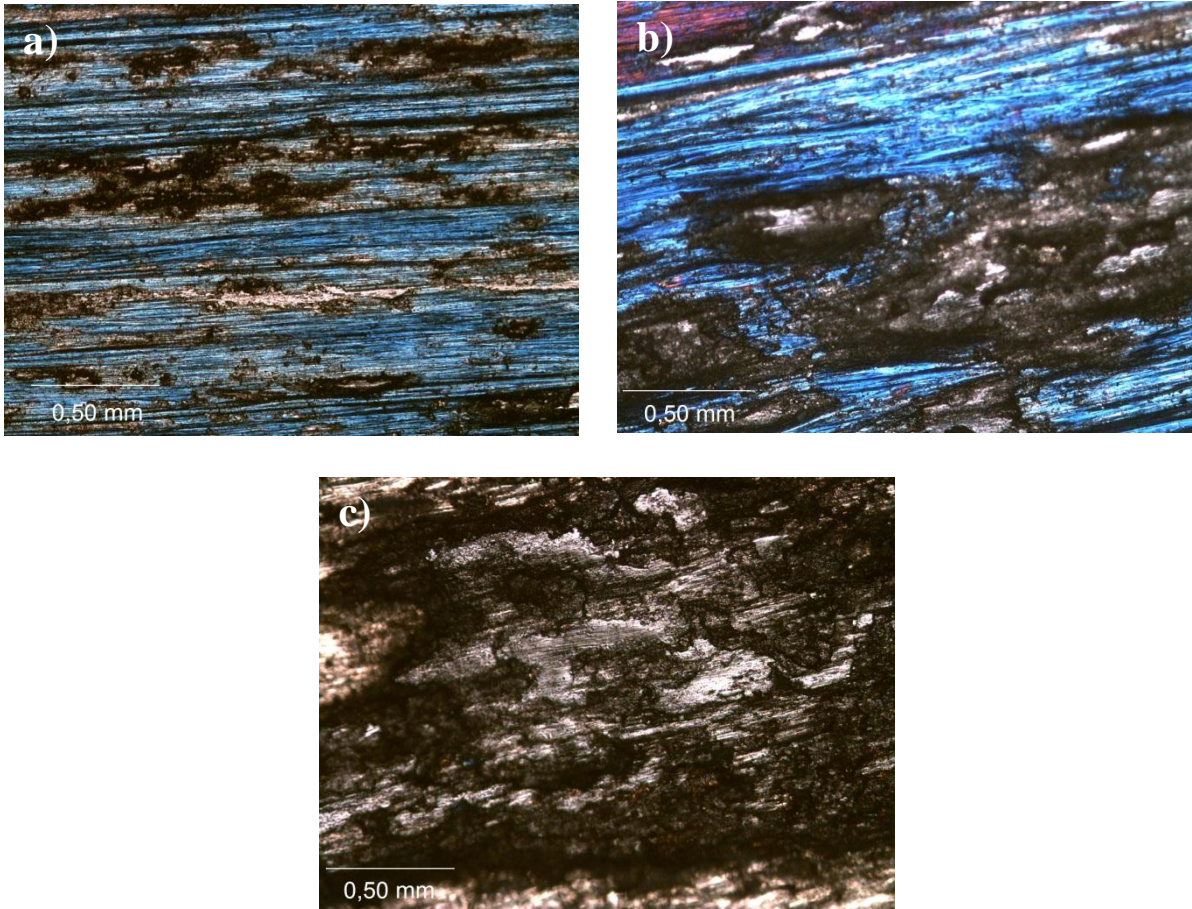


**Figure 3.16**–Wear tracks of Haynes 25, 188 and 214 at 540°C via optical microscope. a)Haynes 25 b)Haynes 188 c)Haynes 214.

Unlike other specimens, wear coefficient of Haynes 214 is slightly increased to  $5.6E-4$  probably due to formation of coarse wear particles within the wear track (Figure 3.16c). Hager et. al. reported that, enhanced plasticity of the nickel-oxide films could be the reason for larger wear particles at elevated temperatures. Moreover, edge dislocations are observed on the wear track of Haynes 214 sheet.

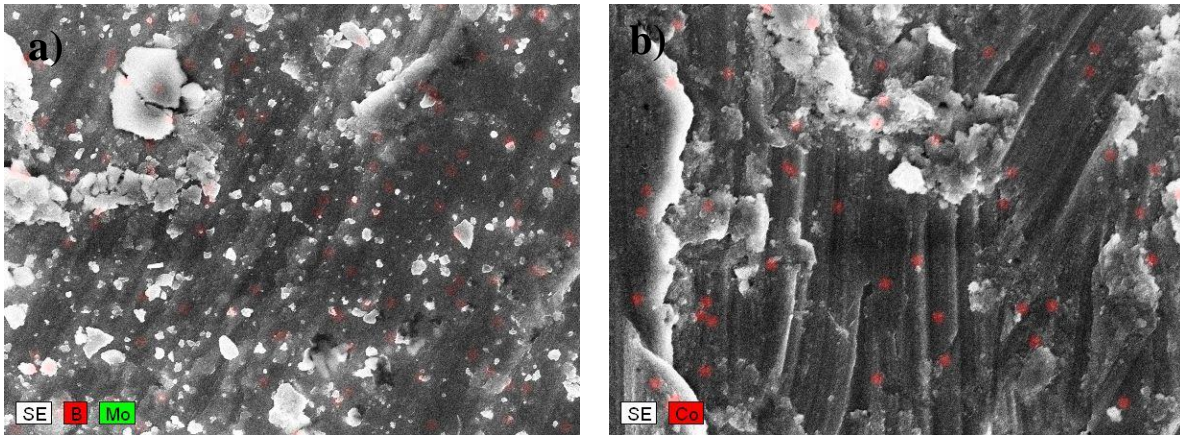


**Figure 3.17** a) Haynes 25 (Locations of transferred Boron from pin to sheet are marked in red.) b) EDX image of Haynes 214 (Locations of transferred Cobalt from pin to sheet are marked in red.)

To check the material transfer phenomena from pin to the disk for Haynes 25, B (Boron) and Mo elements are scanned through EDX analysis. B and Mo are not normally included in the Haynes 25's material composition; therefore, they could provide clues on material transfer. Some amount of B is detected on the wear track while no Mo is observed (Figure 3.17a). Similarly for Haynes 214, small amounts of Co is detected (Figure 3.17b). Material transfer to Haynes 188 is indistinguishable, since its composition is very similar to pin material.

In brief, friction and wear performance of Haynes 25, 188 and 214 sheets are tested against HastelloyX pins. Tests were conducted at 25, 200, 400 and 540°C with 10N dead weight. Test speed was 1Hz with total sliding distance around 1km. Results showed that:

- Haynes 25 has the lowest friction coefficients at all test temperatures.
- Above 400°C, Haynes 25 and 188 exhibit the best wear resistance. Protective cobalt-oxide layers are formed on the Haynes 25 and 188 at 540 °C in addition to nickel, chrome and tungsten oxides.
- Small amount of material transfer from pin to sheet is observed for Haynes 25 and 214 at 540°C. Material transfer to Haynes 188 is indistinguishable, since its composition is very similar to pin material.
- At elevated temperatures, larger wear particles are formed on the wear track of Haynes 214 due to enhanced plasticity of the nickel-oxide films.

As a result, Haynes 188 is selected as the actuator material, since it has superior friction and wear performance over the other candidates.

**CHAPTER 4**  
**DESIGN AND ANALYSIS OF THE HIGH TEMPERATURE ACTUATOR**

**4.1 MATERIAL SELECTION**

Custom design actuator will be positioned between inner and outer shrouds at turbine section. Therefore, it will be subjected to high temperatures. At these conditions, selection of proper actuator materials is important. During material selection high temperature resistance, availability in sheet form, high oxidation resistance, wear resistance and welding ability characteristics were taken into consideration. Cobalt/Nickel superalloys Haynes 25, Haynes 188 and Haynes 214 have been selected as candidate actuator materials. The specifications for these selected materials have been studied. Variation of elastic modulus values with respect to temperature is presented at Figure 4.1 [87-89].

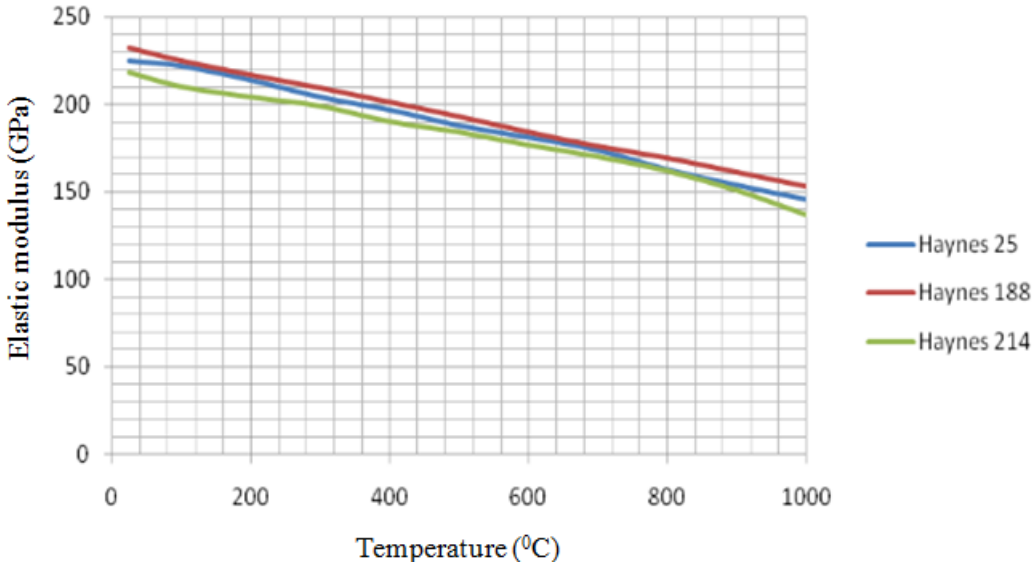


**Figure 4.1** – Variation of elastic modulus of candidate materials with temperature.

Behavior of ultimate strength of the candidate materials has been presented in Figure 4.2 [87-89]. It is apperant from the figure that, for all of the candidate materials ultimate strength dramatically reduces beyond 700 °C. However, for the target operating temperature

of 540 °C the selected materials have sufficient strength combined with excellent wear resistance.

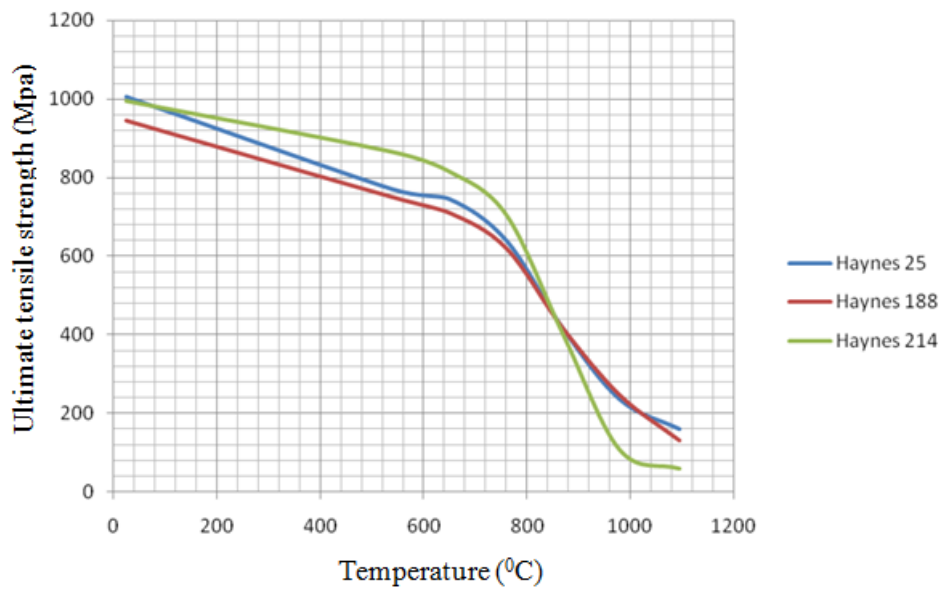


**Figure 4.2** – Tensile strength of candidate materials at elevated temperatures

Variation of yield strength for candidate materials has been plotted with respect to temperature in Figure 4.3 [87-89]. Haynes 214 has higher yield strength than other candidates up to 900 °C. For higher temperatures, Haynes 25 or 188 retain better strength.

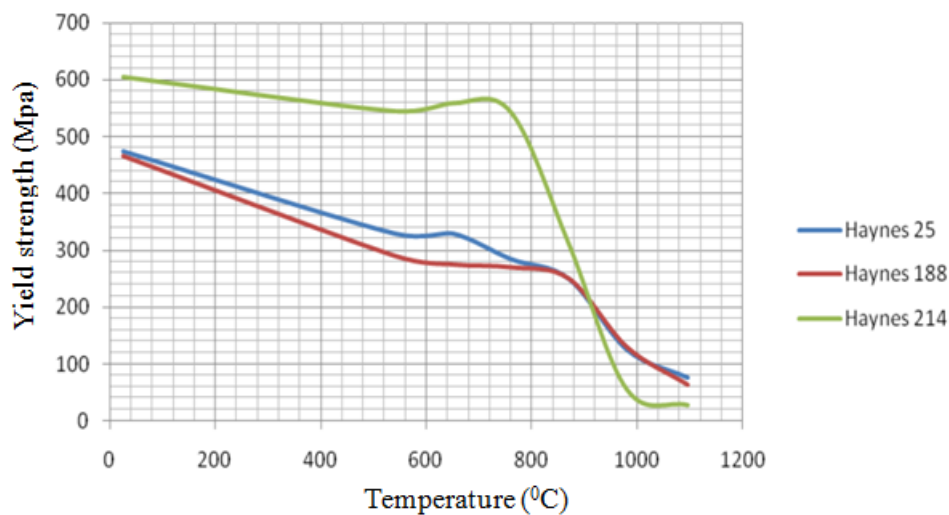


**Figure 4.3** – Variation of yield strength for the candidate materials at elevated temperatures

Oxidation resistance is one of the most important properties that is expected from the actuator material. At high temperatures, material loss occurs due to the oxidation. Figure 4.4 [87-89] presents the oxidation depth values for the candidate materials at elevated temperatures. The presented data was acquired by subjecting the selected superalloys to high temperature for several hours. Although, Haynes 25 has the lowest oxidation resistance, in the 600-800°C interval, maximum oxidation depth is only 0,55µm and it would lead to 0.0048mm per year which is acceptable. Therefore, all of the material candidates have been considered to have sufficient oxidation resistance.

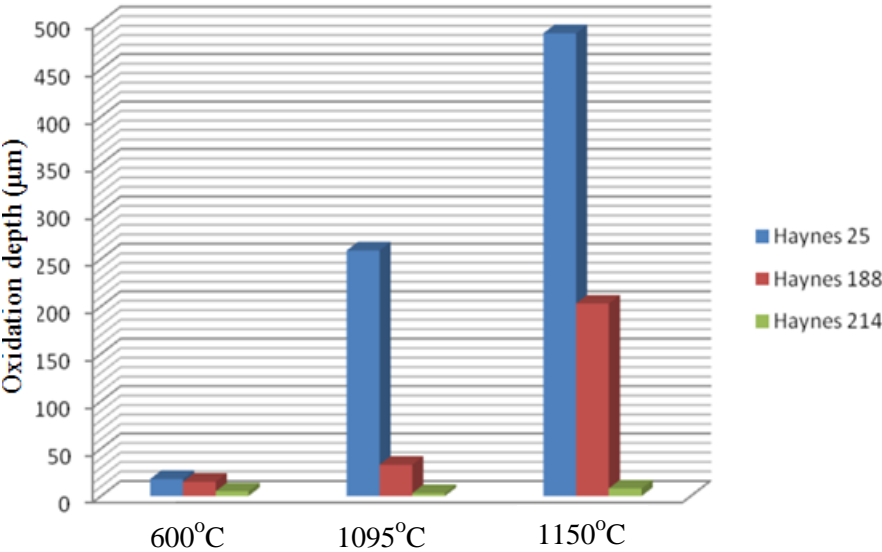


**Figure 4.4** – Oxidation depth of candidate materials at elevated temperatures.

The custom design actuator will be manufactured by welding the superalloy sheets together. Welding suitability of the candidate materials has been presented at Table 4.1 [87-89].

**Table 4.1** – Eligible welding types for Haynes 25, 188 and 214

Material	Electron Beam Welding	Tungsten Inert Gas (TIG) Welding	Metal Inert Gas Welding	Electric Arc Welding	Electric Resistance Welding
Haynes 25	√	√	√	-	√
Haynes188	√	√	√	-	√
Haynes214	-	√	√	√	-

All of the candidate materials possess favorable welding behavior. Actual selection of the actuator material depends on additional information on high temperature friction and wear resistance, as well as the working temperature and required service life depending on engine and location. For this study, a sample 540 °C working temperature has been considered. Therefore, Haynes 188 has been selected due to its excellent friction and wear resistance. The high temperature friction and wear resistance of candidate materials were discussed in detail at Chapter 3.

### 4.2 COMPACT ACTUATOR DESIGN

Compact actuator system has been disclosed by M. F. Aksit [90]. It is composed of two thin sheet strips welded at long edges and partially welded accross with selected intervals. Partial welds provide actuation fluid to pass and pressurize each cell leading to multiple lift pads which get actuated through application of pressure at a single entry. (Figure 4.5). Actuation occurs through pressurizing the interior section of the actuator with a fluid, hence two plates deflect for some displacement as shown at Figure 4.6.

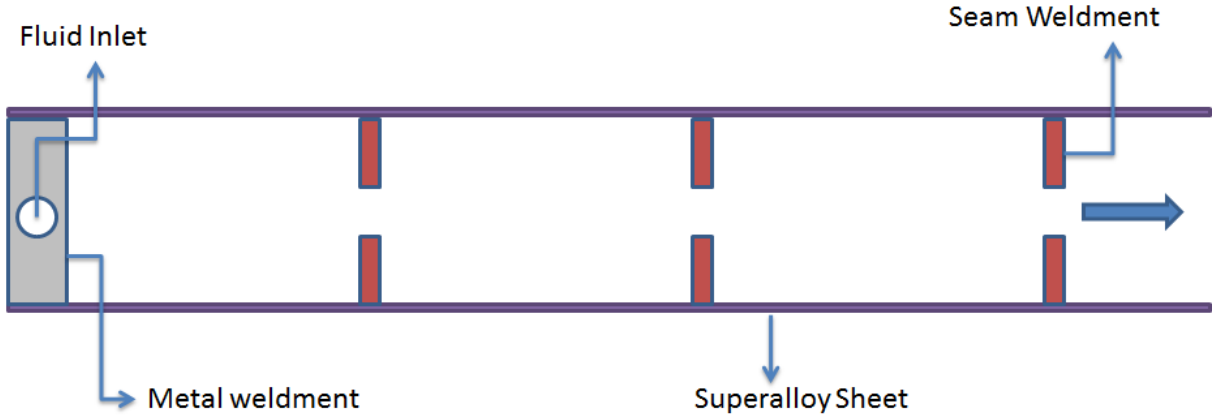
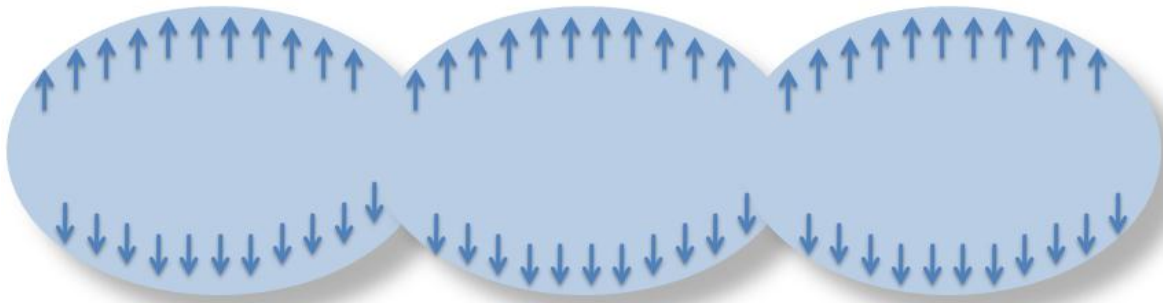
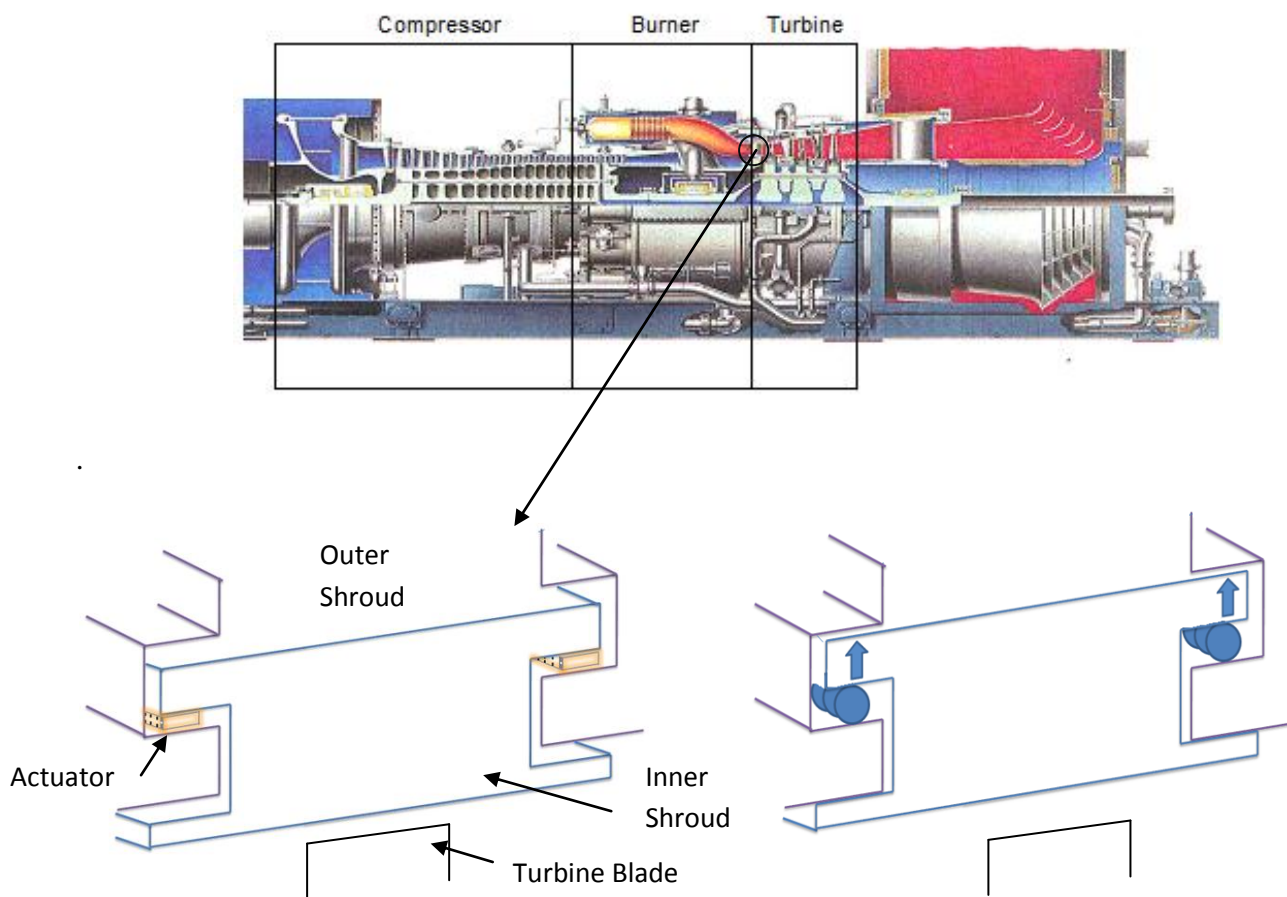


Figure 4.5 - Top view of the actuator.



**Figure 4.6-** Cross section of the pressurized actuator

Actuator will be positioned at the interface between inner and outer shrouds of the gas turbine (Figure 4.7). When pressurized, it moves the inner shroud outward and away from the blades during transients. Therefore the clearance between inner shroud and turbine blade increases. When actuation fluid is evacuated, system is deactivated.



**Figure 4.7 –** Actuator position in the gas turbine.

## 4.3 ANALYSIS OF DIFFERENT ACTUATOR DESIGNS

### 4.3.1 Actuator Design A:

Two different actuator designs have been evaluated. The first actuator consists of two long sheet strips welded along the edges to form an inflatable cavity which is divided into sub cells with intermitted welds seam running across. The first design is more compact and simpler. Yet, it has less displacement capability.

The simple first actuator design consisted of sequential pressure cells. Being identical in geometry, and exposed to the same actuation pressure, each cell behaves in the same manner when actuated. Due to symmetry, only one side of an actuator cell is sufficient to analyze. In other words, only the upper sheet of a pressure cell between two consecutive seam welds has been investigated as shown in Figure 4.8. Geometric details of this single sheet/plate is presented in Figure 4.9

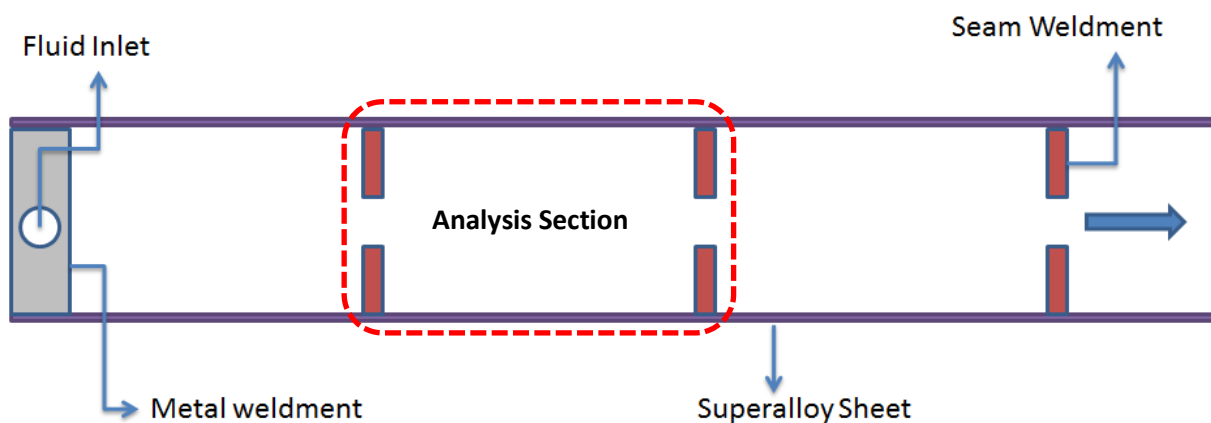
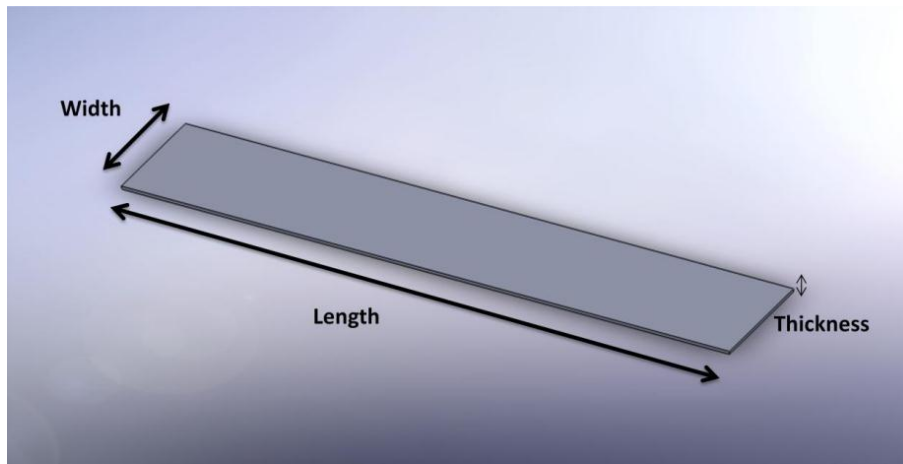


Figure 4.8 - Analysis Section.



**Figure 4.9** - Dimensions of selected actuator cell for Design A: Length=50mm, Width=10mm, Thickness=0.25mm

#### 4.3.1.1 Boundary Conditions

Boundary conditions for the analysis of the first design have been presented in Figures 4.10 and 4.11. While a uniform pressure load has been applied at inner face of the sheet, there is a constant external load that is applied at the center of the outer side of the sheet. This constant load represents the working load that each cell has to lift. Working load comes from the pressure load applied on each inner shroud due to existing pressure differential between outer and inner side of each inner shroud. The magnitude of this load varies from application to application. In this work, considering that an inner shroud will be actuated by at least 4 lift cells (2 at each side) a 400 N per cell working load has been used to represent an average inner shroud load in a mid size industrial turbine.

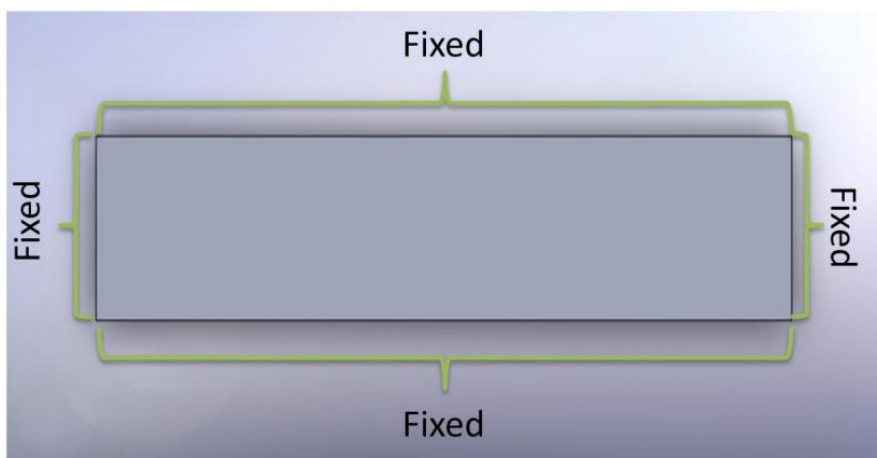


**Figure 4.10** – Boundary conditions of the actuator

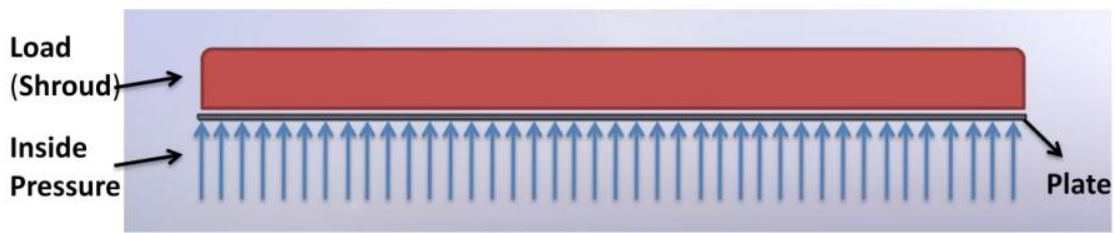


**Figure 4.11** – Forces acting on the actuator sheet

List of design parameters are summarized at Table 2. Length of the actuator cell, “a”, is defined as 50mm where width, “b”, is 10mm. The details about optimization of the parameters “a” and “b” are presented in the next section. Thickness of the sheet is 0.25 mm and “q” is the required amount of pressure that leads to 0,00025 m maximum displacement. Average temperature of the actuator located between inner and outer shrouds at first stage of a typical gas turbine is accepted to be around 540°C. Therefore, mechanical properties of Haynes 188 such as Poisson’s ratio and elastic modulus at 540 °C are taken into consideration during the analyses.

**Table 4.2** – List of design parameters

<b>Design Parameters</b>	<b>Definition</b>
<b>a</b>	Length of the sheet
<b>b</b>	Width of the sheet
<b>t</b>	Thickness of the sheet
<b>q</b>	Interior fluid pressure
<b>w</b>	Load (external Load)
<b>T</b>	Temperature

### 4.3.1.2 Simple Plate Analysis of the Actuator Design A

The goal of this simple plate analysis is to find the required inner fluid pressure to achieve 0.25mm displacement using selected superalloy sheet. Stress and deflection of a rectangular plate with all edges fixed (Figure 4.12) while under uniform can be calculated as follows; [91]

$$y_{max} = \frac{\alpha q b^4}{E t^3} \quad (4.1)$$

$$\sigma_{max} = \frac{-\beta_1 q b^2}{t^2} \quad (4.2)$$

where,  $y_{max}$  is the maximum deflection and  $\sigma_{max}$  is the maximum stress that occur under pressure load,  $q$ .  $E$  is the elastic modulus of the material (at 540 °C for our case), and  $a$ ,  $b$ ,  $t$  are length, width and thickness respectively.

Rectangular plate, all edges fixed

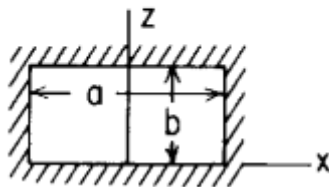


**Figure 4.12** – Boundary conditions for the simple plate analysis

Parameters  $\beta_1$ ,  $\beta_2$  and  $\alpha$  have specific values for different length(‘a’)/width(‘b’) ratios as shown in Table 4.3 [91].

**Table 4.3-**  $\beta_1$ ,  $\beta_2$  and  $\alpha$  values for corresponding a/b ratios

a/b	1.0	1.2	1.4	1.6	1.8	2.0	$\infty$
$\beta_1$	0.3078	0.3834	0.4346	0.4680	0.4872	0.4973	0.5000
$\beta_2$	0.1386	0.1794	0.2094	0.2286	0.2406	0.2472	0.2500
$\alpha$	0.0138	0.0188	0.0226	0.0251	0.0267	0.0277	0.0284

Values for parameters  $\beta_1$ ,  $\beta_2$  and  $\alpha$  are extracted from Table 4.3 for  $a/b = \infty$  ratio as 0.5, 0.25 and 0.0284 respectively. Modulus of elasticity of Haynes 188 material at 540 °C is 197 GPa [88].  $y_{max}$  is the maximum deflection and is 0.25 mm. The only unknown is “q”, the required interior pressure which can be found by Equation 4.1.

Using Equation 4.1 and solving the equation for “q” we get;

$$q = \frac{y_{max}Et^3}{\alpha b^4} = \frac{0.00025m \times 1,97 \times 10^{11}Pa \times (0,00025m)^3}{0,0284 \times (0,01m)^4} = 2.3658 \times 10^6 Pa \quad (4.3)$$

$$= 23.658 \text{ bar}$$

After “q” is found, maximum stress, " $\sigma_{max}$ ", can be calculated by Equation 4.2 as;

$$\sigma_{max} = \frac{-\beta_1 qb^2}{t^2} = \frac{-0.5 \times 2.3658 \times 10^6 Pa \times (0,01m)^2}{(0,00025m)^2} = 1.8926 \times 10^9 Pa \quad (4.4)$$

#### 4.3.1.2.1 Effect of the design parameters on maximum stress and displacement:

Using the same method to calculate  $y_{max}$  and  $\sigma_{max}$ , the optimum “a”, “b” and “t” values that maximize deflection and minimizes stress in a minimal space can be estimated. In this analysis, the effect of the different a/b, t and b values have been investigated while keeping other parameters constant. Results have been plotted in Figures 4.13-18.

**i. Selecting the a/b ratio:**

Using the Equations 4.1 and 4.2, the required inner pressure and the corresponding maximum stress values have been investigated when a/b ratio varies from 1 to 5 (Figure 4.13-4.14). Results indicate that the required amount of pressure and the maximum stress decrease with increasing a/b ratios. However, an asymptote is reached when a/b ratio is around 2.3. Considering geometric limitations in a typical midsize industrial turbine first stage application width of the actuator strip has been limited to 0.01 m. Therefore, one actuator length should be minimum 0.023m. Considering that such a typical shroud would have around 0.1 m length, and two cells are sufficient to lift an inner shroud at each side, cell length has been selected as 0.05 m.

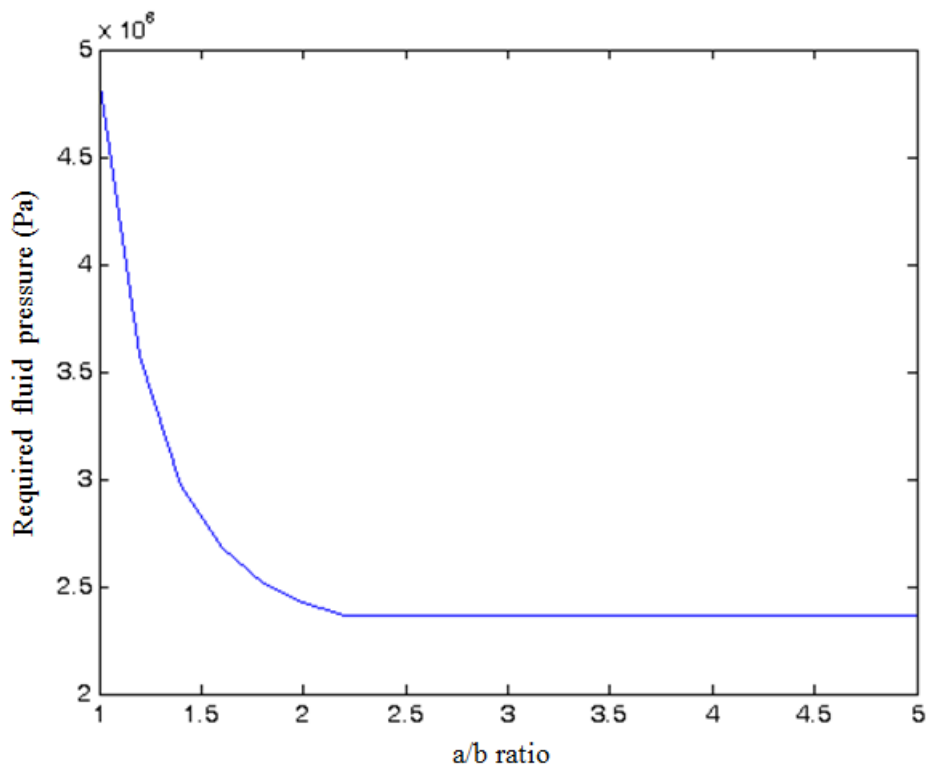


**Figure 4.13** – Required liquid pressure in order to achieve 0.25 mm displacement vs a/b ratio

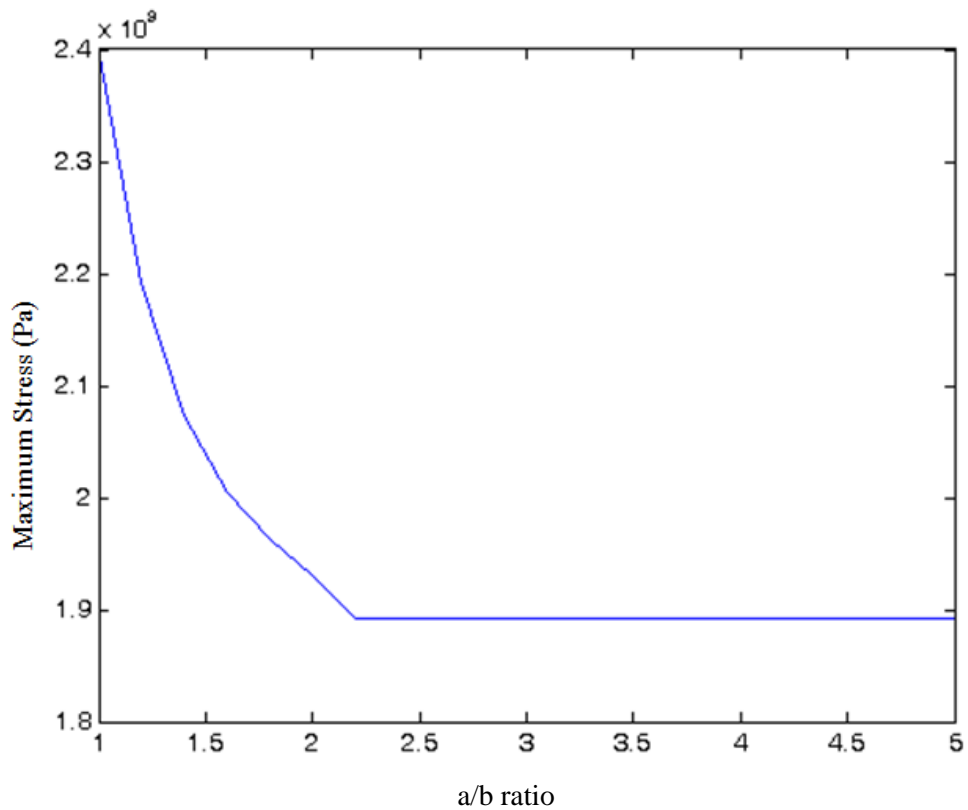


**Figure 4.14** – Maximum stresses with 0.25 mm displacement vs sheet thickness

**ii. The effect of sheet thickness over required liquid pressure and maximum stress**

Applying the same method for actuator sheet thickness(t), maximum stress values corresponding to the required actuation pressure in order to achieve 0.25 mm displacement have been calculated for sheet thickness values ranging from 0.5E-4 to 5E-4 m. The results have been plotted in Figures 4.15 and 4.16). The required pressure increases exponentially with the sheet thickness, while the trend of maximum stress is linear. It is favorable to reduce sheet thickness as small as possible to minimize stress. However, oxidation limits actuator life. Therefore, 0.25 mm sheet thickness selected for Haynes 188 actuators.

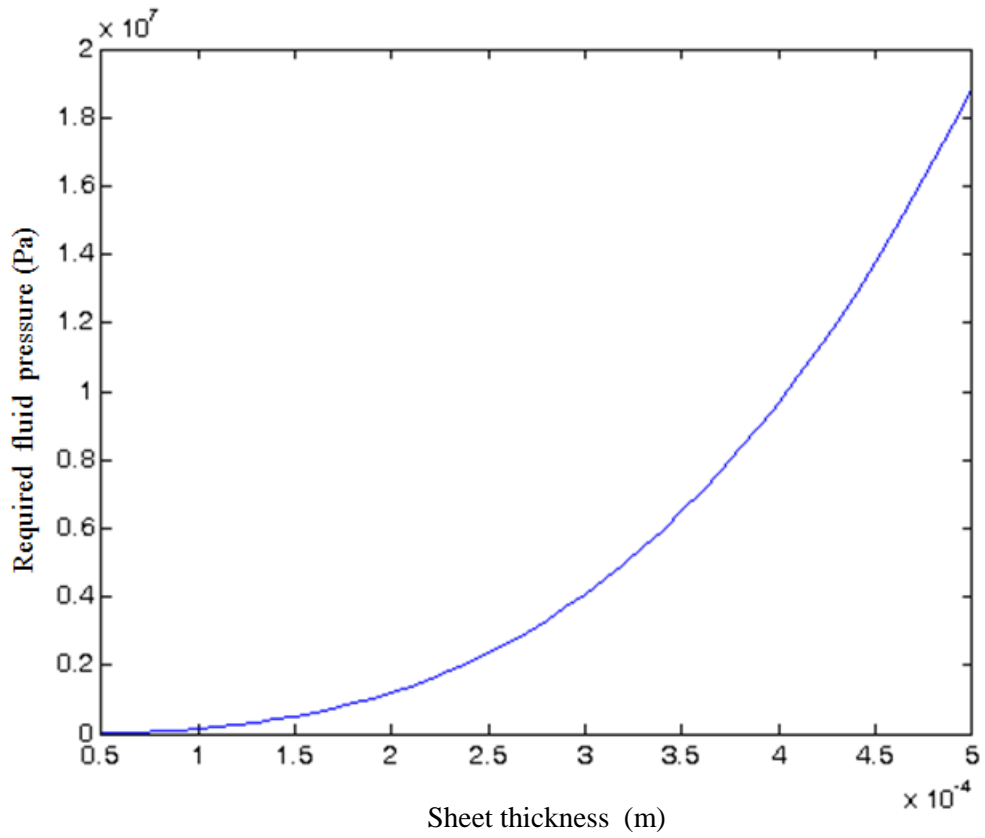


**Figure 4.15**– Required liquid pressure to achieve 0.25mm displacement vs sheet thickness

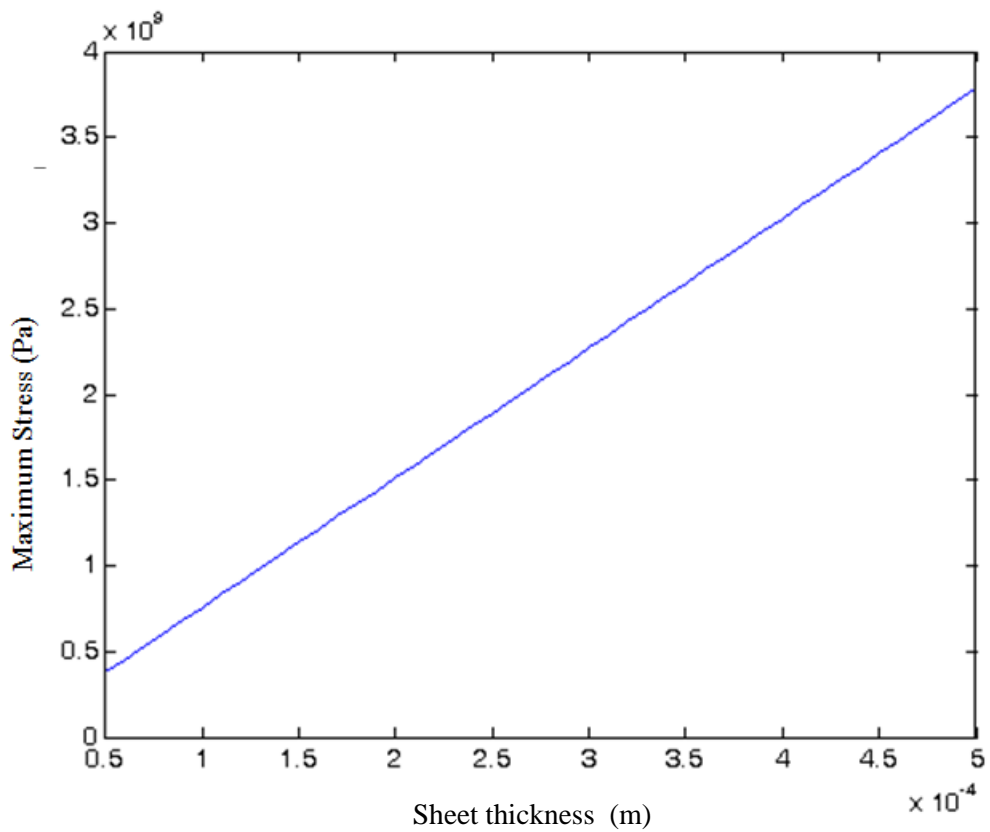


**Figure 4.16** – Maximum stress vs sheet thickness. (Other parameters are kept constant)

### iii. Effect of the cell width over required liquid pressure and maximum stress

Although cell width, “b”, has been defined as 0.01 mm for a sample application, it would be useful to observe its effect on required pressure and maximum stress for various size applications. Again, using the same procedure through the equations 4.1 and 4.2, maximum stress and cell width relations have been investigated (Figures 4.17 and 4.18). The results indicate that both maximum stress and the required actuator drop exponentially as cell width increases.

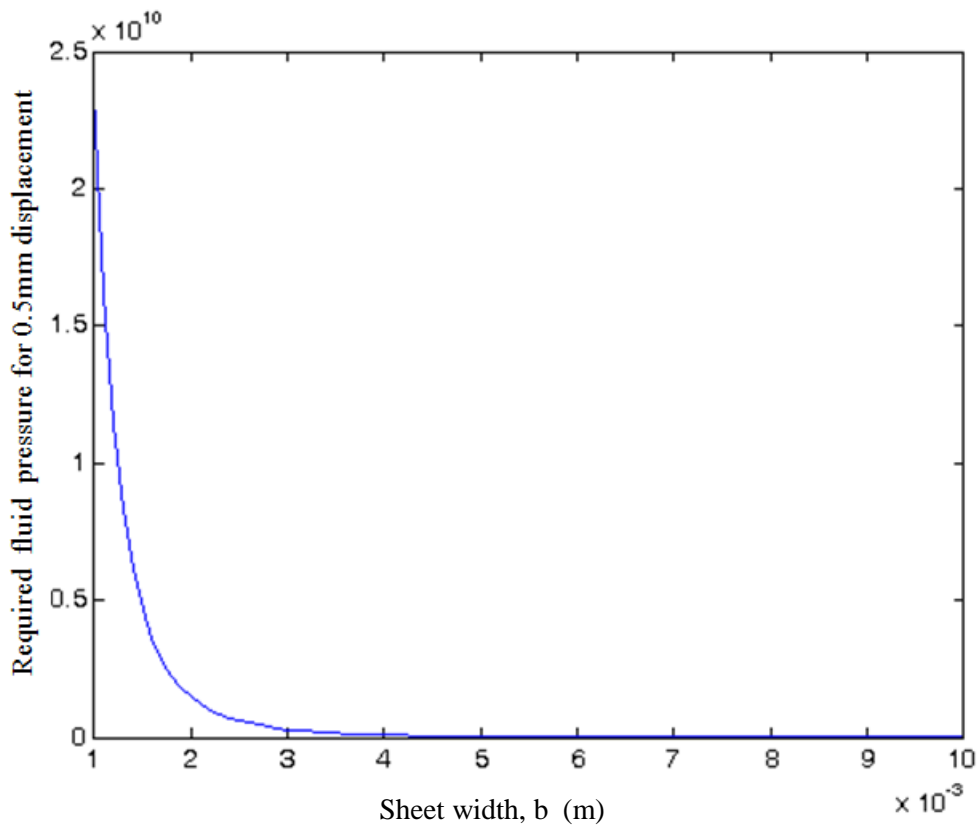


Figure 4.17 – Required liquid pressure to achieve 0.25mm displacement vs actuator width

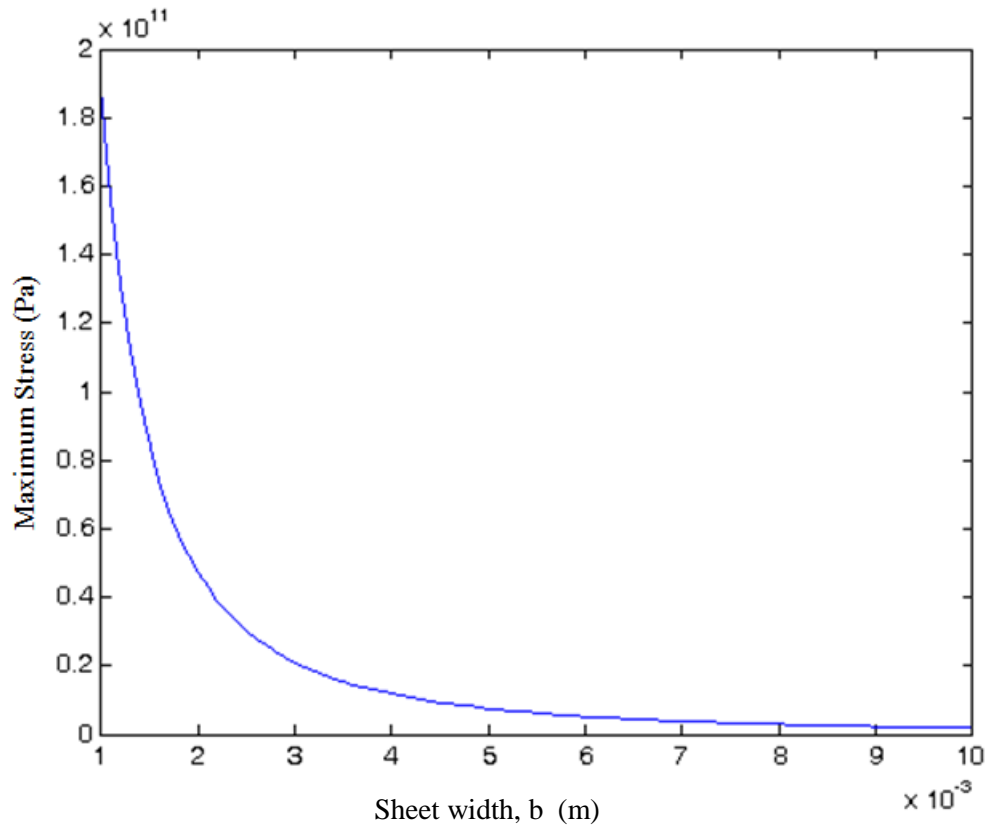


Figure 4.18– Maximum stress vs actuator width (Other parameters are kept constant).

#### 4.3.1.3 Finite element analysis of the actuator Design A:

As design is very simple, full analytical plate solution is available, and a finite element analysis is not necessary. However, second actuator design involves convoluted structure, and analytical solution is difficult to obtain. Once a finite element model and solution procedure has been established and validated, the same procedure can be used to analyze the convoluted actuator model. A commercially available code, COMSOL has been used to obtain displacement and stress solutions. “2D mindlin plate” module and “pardiso” solver have been selected for the analyses. Length (a), width (b) and thickness (t) of the sheet have been selected as 0.05 m, 0.01m and 0.00025 m respectively. Boundary conditions were the same as the conditions used in the plate analysis. 2.3658 MPa fluid pressure (q) at the inner side of the sheet. Elastic modulus and Poisson’s ratio of Haynes 188 at 540°C are 197GPa and 0.3 respectively [88]. Finite element analysis results have been presented in Figures 4.19-20.

The results indicate that, maximum displacement occurs at the center of the sheet as 2,535E-04 m (Figure 4.19). Maximum displacement solution of FE analysis is very close to

the analytical solution which is  $2.53E-04$  m. On the other hand, maximum stress has been calculated by FEA as  $1.684GPa$  which is relatively close to the analytical solution (with %9 error). The results from plate analysis and FEA have been compared in Table 4.4). The small difference is attributed to mesh resolution in Finite Element Analysis.

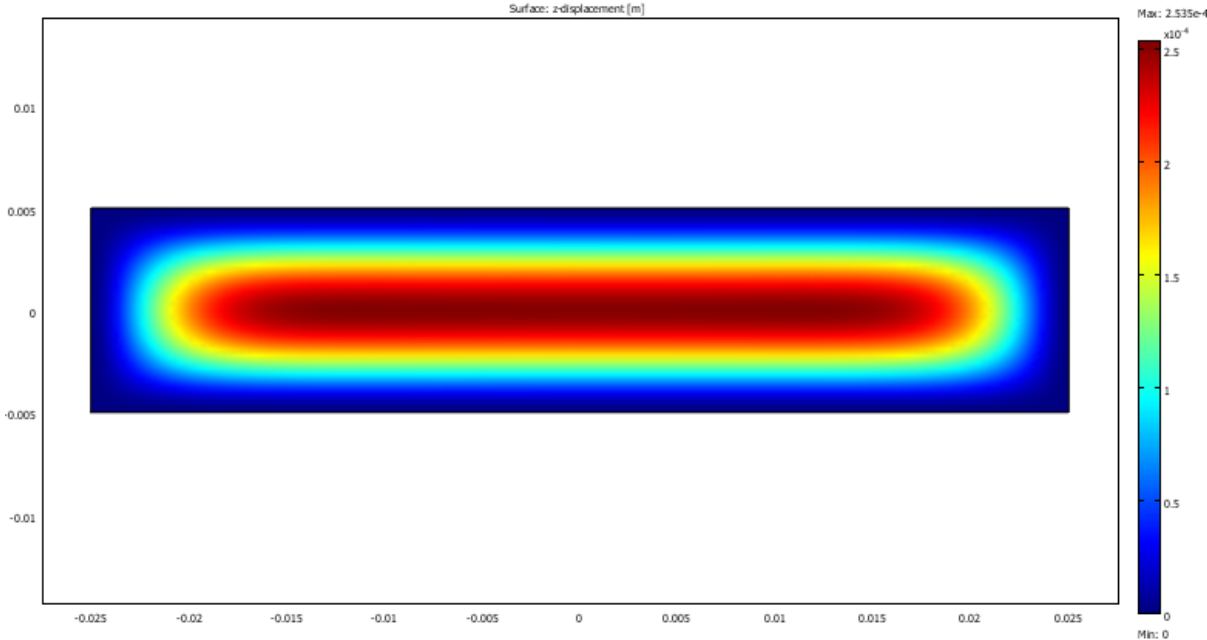


Figure 4.19 - Displacement distribution over the plate

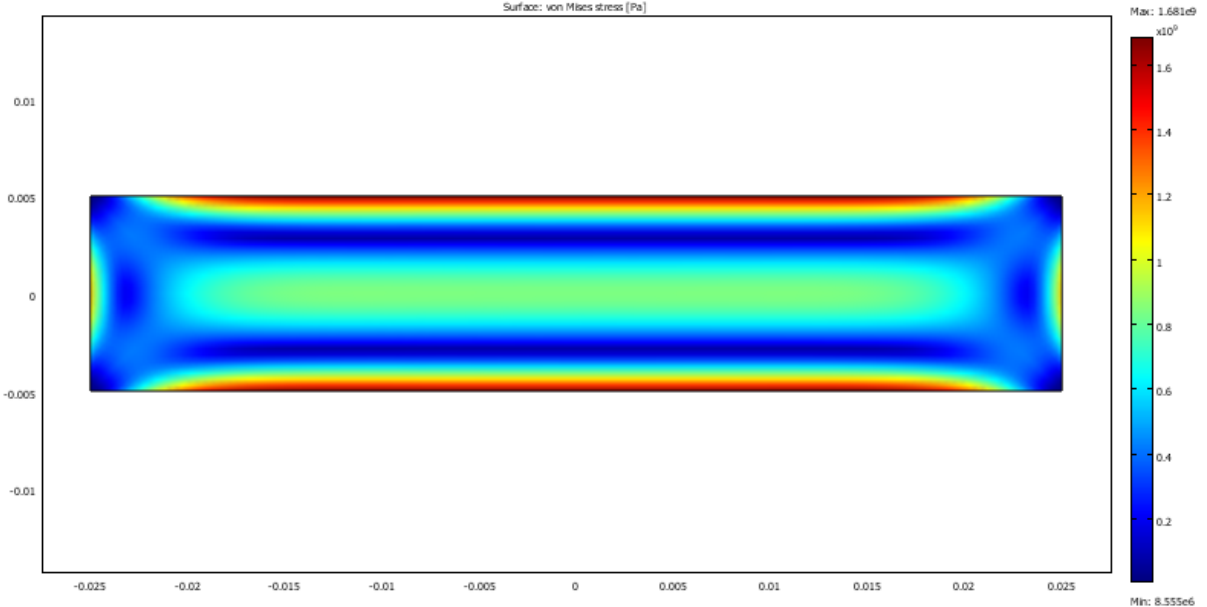


Figure 4.20– Stress distribution over the plate

**Table 4.4** – Comparison of analytical and comsol results

	<b>Analytical</b>	<b>Comsol</b>	<b>Error</b>
<b>Maximum Displacement</b>	0.25 mm	0.253 mm	1%
<b>Maximum Stress</b>	1.890 GPa	1.681 GPa	9%

Maximum stress values found both by analytical model and finite element analysis are in the order of GPa which are extremely higher than the yield strength of the material at 540°C, Haynes 188, that is 290MPa. Therefore, when restricted to 0.01 m actuator width, the first design does not allow actuation to 0.25 mm. The second prototype allows for larger deflections with a convoluted design.

### 4.3.2 Actuator Design B: Actuator with Bellow Cross Section

As an alternative to Design A, a bellow-like convoluted actuator structure has been studied. The convolutions allow for more displacement and reduce stresses. Just as the previous design, this design is also composed of sequential actuator bellow cells. Geometry of a single cell and convoluted bellow cross-section are presented at Figures 4.21 and 4.22 respectively.

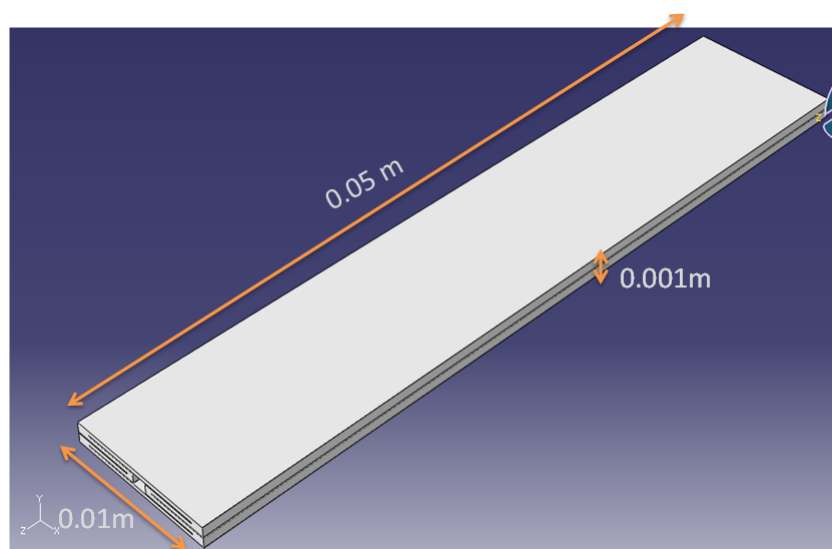


**Figure 4.21** – Design B dimensions

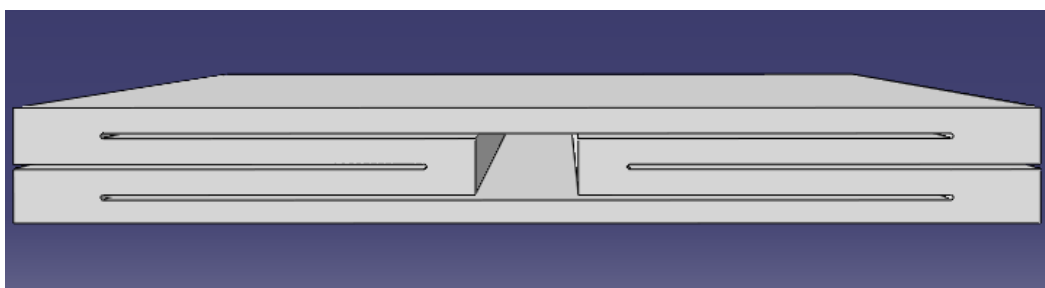


**Figure 4.22** – Design B front view

In Figure 4.23, upper right quarter portion of the cross section is presented to illustrate geometrical details clearly. The parameter “wd” is half of the actuator width as 5 mm, “th” is the thickness of a single sheet as 0.25 mm, “i.w.” and “o.w.” parameters stand for interior and outer weld penetration depths respectively, and both measure 1 mm. Finally, “gp” represents half of the gap width in the cross section which measures 0.5 mm.

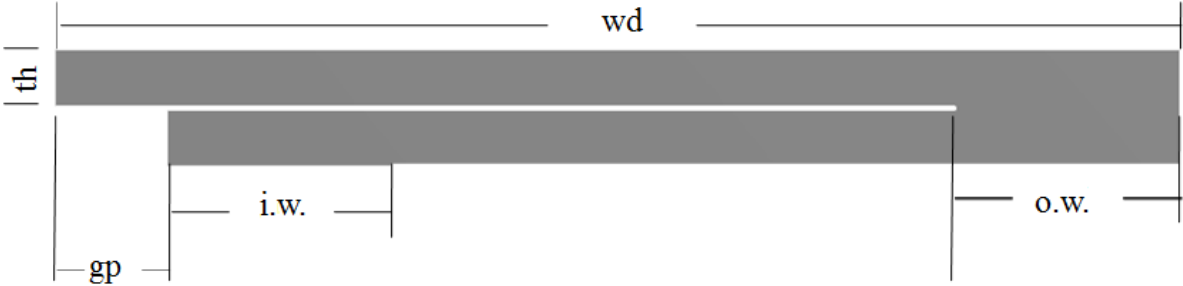


**Figure 4.23** –Design B upper right quarter section detail.

As illustrated in Figure 4.24, the array of actuator cells are connected to the each other with opening in the seam welds across, just like the previous design. A fluid inlet to pressurize the actuator is positioned in the first cell (Figure 4.25). The inlet is connected to a fluid channel with a welded attachment whose details were mentioned in Chapter 3.

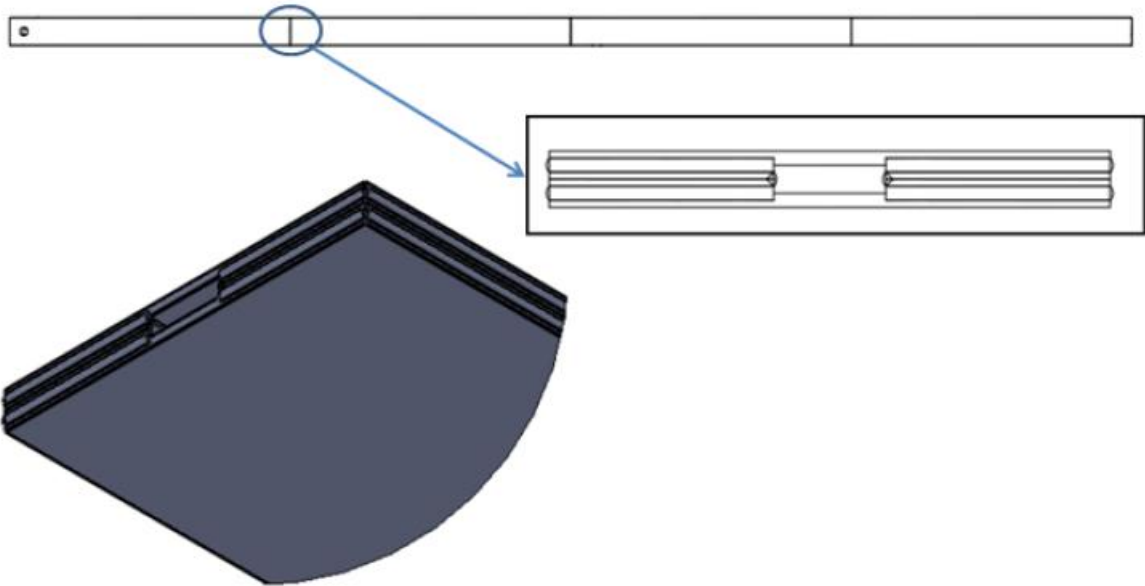


**Figure 4.24**– Seam welding locations between the cells.

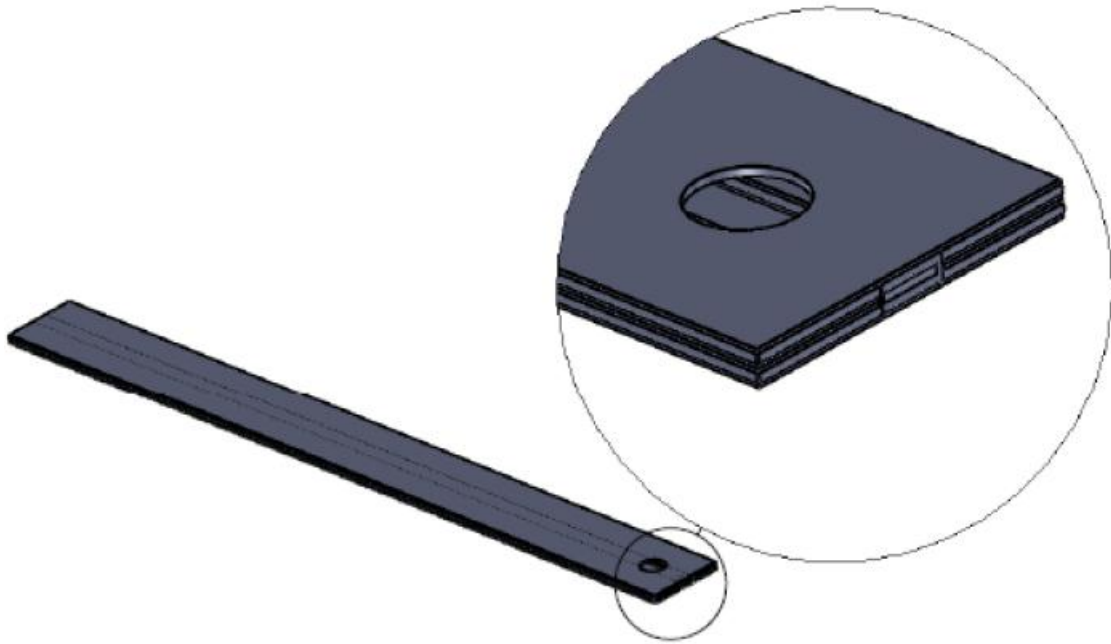


**Figure 4.25** - Fluid inlet position on the first cell of the array.

Due to the difficulties experienced with COMSOL regarding mesh density at small corners, another commercial FEA code, ABAQUS, has been used to analyze stress and displacements in Design B actuator. Following the discussion for Design A, dimensions of a representative actuator cell has been selected as 0.05 m, 0.01 m and 0.001 m which represent length (a), width (b) and total thickness (t) respectively. Elastic modulus and Poisson’s ratio for Haynes 188 at 540 °C are 197 GPa and 0.3 respectively. Yield strength at the same temperature is 290MPa. Material properties for Haynes 188 are summarized in Table 4.5.

**Table 4.5** – Mechanical properties of Haynes 188 at 540°C

<b>Haynes 188 @ 540°C</b>	
Elastic Modulus	197 GPa
Poisson Ratio	0.3
Yield Strength	290 MPa
Ultimate Strength	750 MPa

#### 4.3.2.1 Boundary Conditions:

To better illustrate boundary conditions 1/8 of the actuator is viewed in Figure 4.26. In order to represent seam welds along the edges, sections indicated in blue are fixed where all 6 degrees of freedom are constrained. The entire interior surface of the actuator cell is marked with red color where uniform distributed load has been applied in order to simulate the actuator internal pressure as shown in Figure 4.26. An external work load has been applied on the outer surface location representing the cell center. The magnitude of these loads follow from the discussion presented for Design A.

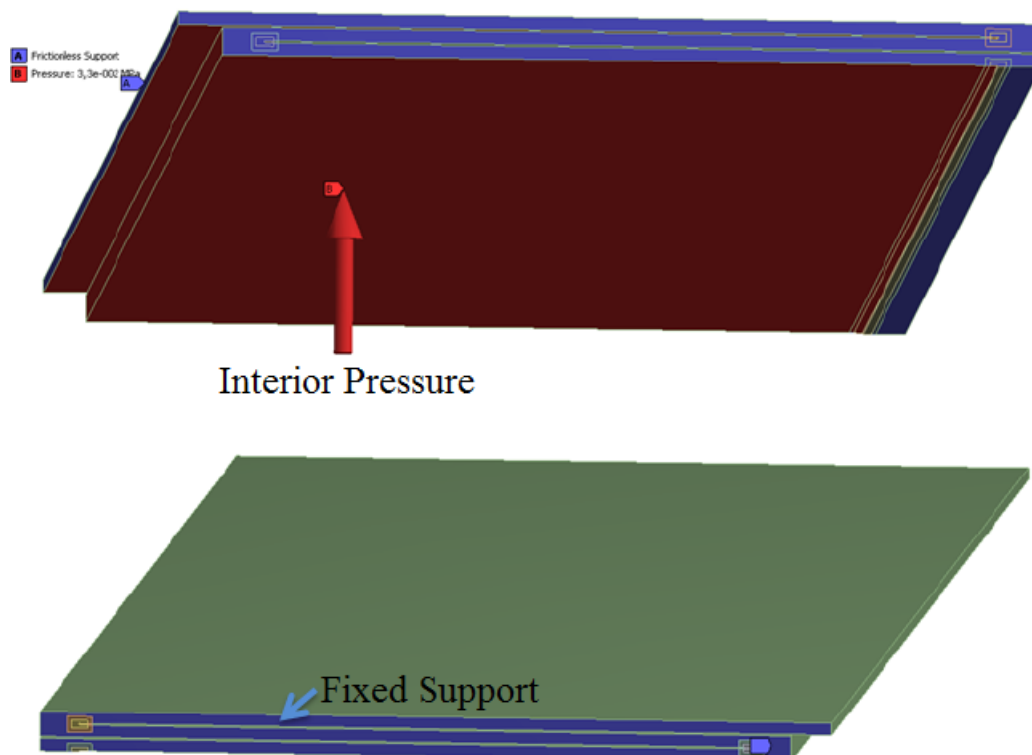


**Figure 4.26-** Boundary conditions

### 4.3.2.2 Results:

Finite element analysis solutions presented in Figures 4.27 through 4.32 and Tables 4.6 through 4.8. Overall results are summarized at Figure 4.33 and Table 4.9. Results indicate that maximum displacement occurs at the center of the cell as expected with a magnitude of  $1,298E-4m$  for 5 bar interior pressure (Figure 4.27). The achieved displacement is about half of the ultimate goal,  $2,5E-4$  m. Maximum stress is below the yield strength of Haynes 188 with a value of  $255.85MPa$  (Figure 4.28). When interior pressure is increased to 10 bar, the displacement and maximum stress values are increased to  $0.2596$  mm and  $511.7$  MPa respectively. Similarly for 20 bar interior pressure, displacement and maximum stress values are doubled again to reach  $0,5192$  mm and  $1023$  MPa respectively. Both 10 and 20 bar solutions indicate local plastic deformations among the corners of the edge welds.

**Table 4.6** –FEA results for Design B under 5 bar interior pressure

DESIGN B - Half Bellow	
Interior liquid pressure (bar)	5
Total displacement (mm)	0.1298
Maximum stress (MPa)	255.85

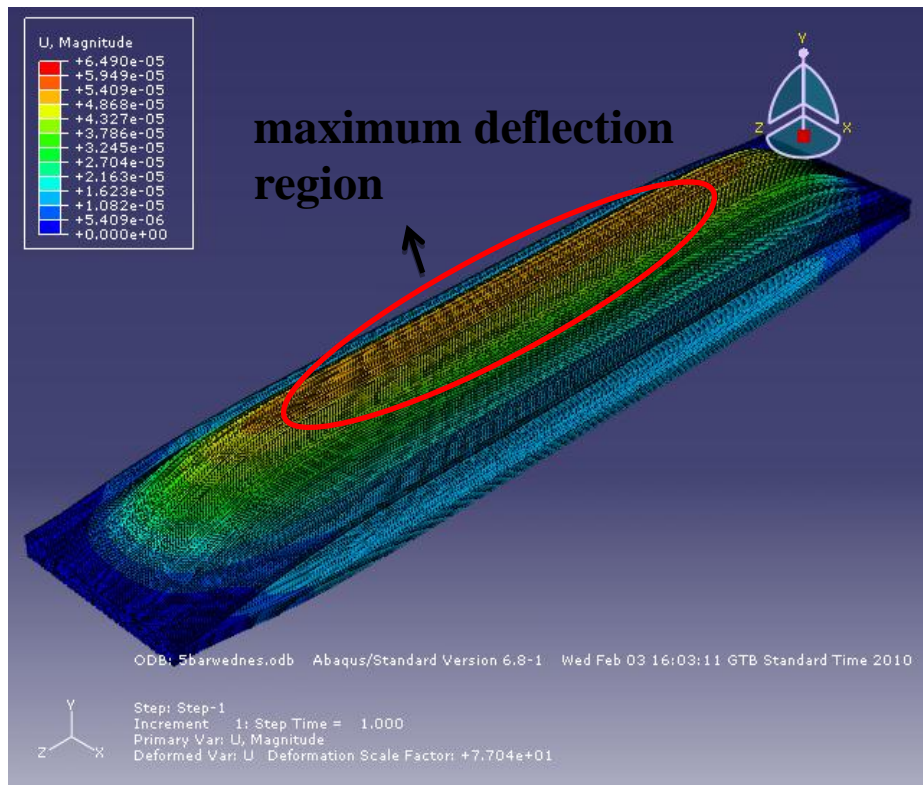


**Figure 3.27** – FEA displacement results for 5 bar interior pressure

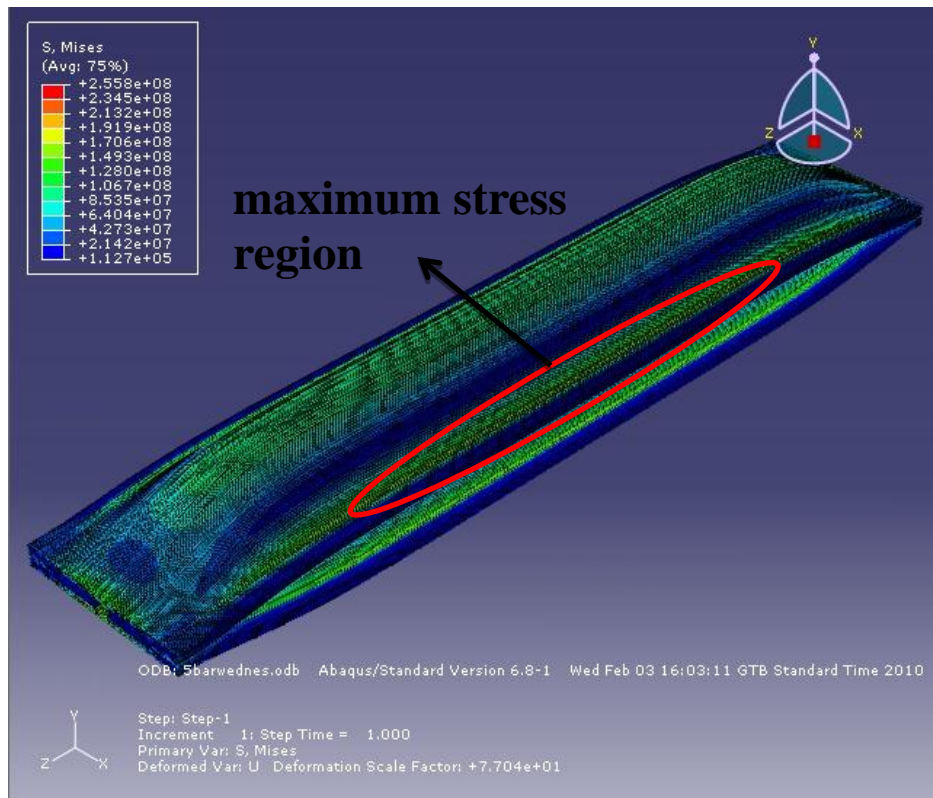


**Figure 4.28** – FEA stress results for 5 bar interior pressure

**Table 4.7** –FEA results for Design B under 10 bar interior pressure

<b>DESIGN B - Half Bellow</b>	
<b>Interior liquid pressure (bar)</b>	10
<b>Displacement of a single sheet (mm)</b>	0.1298
<b>Total displacement (mm)</b>	0.2596
<b>Maximum stress (MPa)</b>	511.7

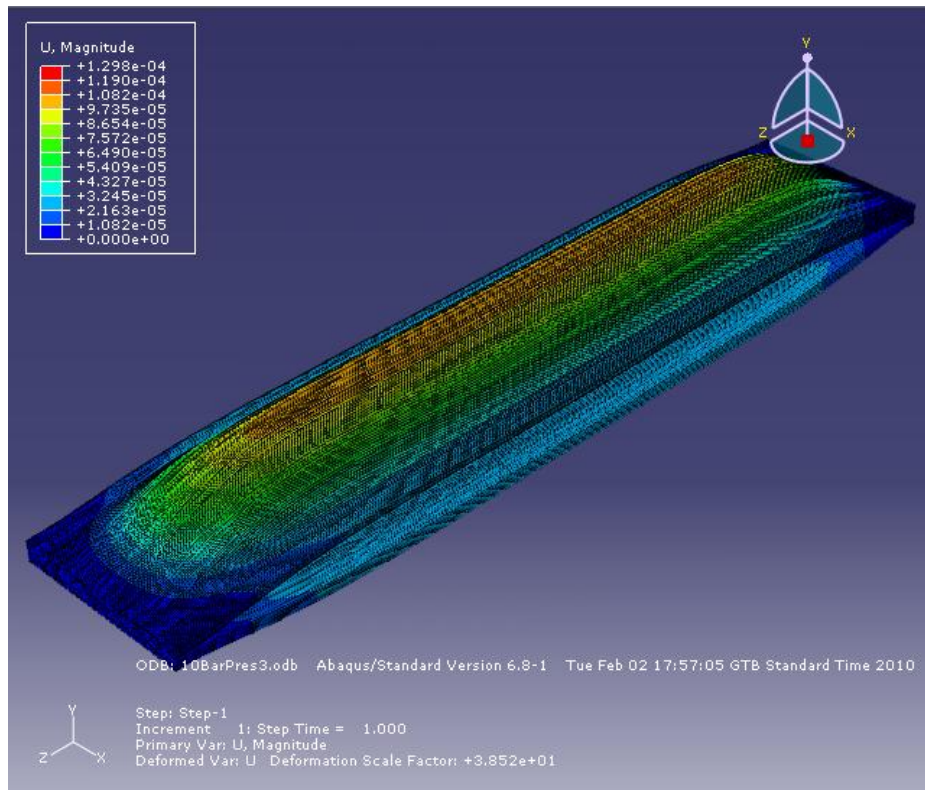


**Figure 4.29** – FEA displacement results for 10 bar interior pressure.

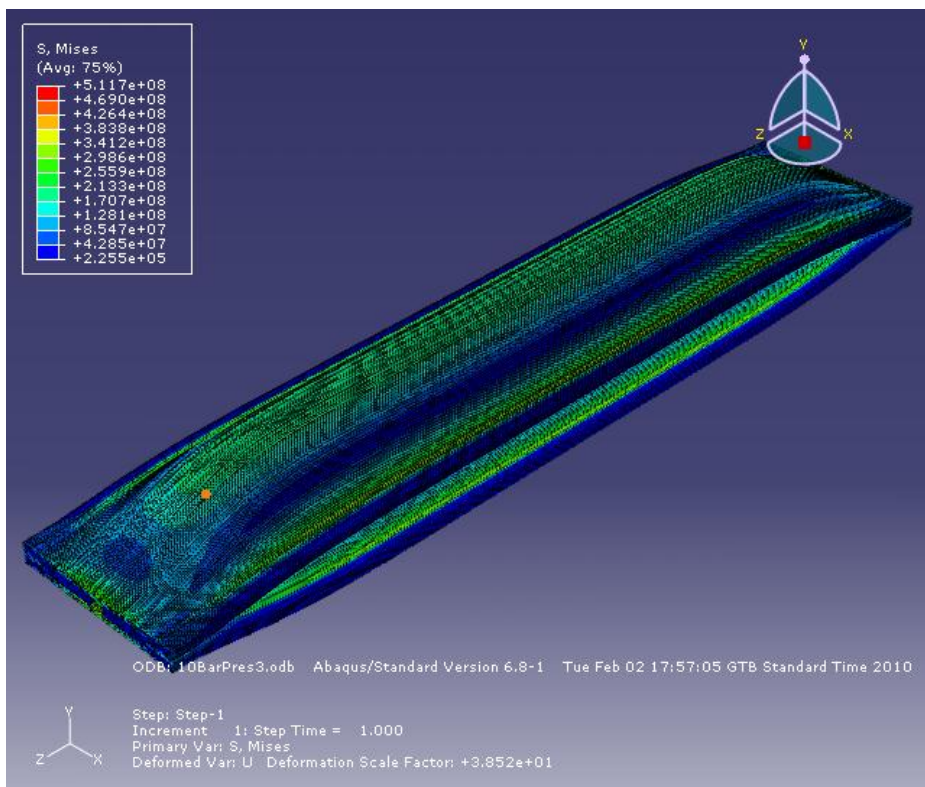


**Figure 4.30** – FEA stress results for 10 bar interior pressure.

**Table 4.8** –FEA results for Design B under 20 bar interior pressure.

<b>DESIGN B - Half Bellow</b>	
<b>Interior liquid pressure (bar)</b>	20
<b>Displacement of a single sheet (mm)</b>	0.2596
<b>Total displacement (mm)</b>	0.5192
<b>Maximum stress (MPa)</b>	1023.4

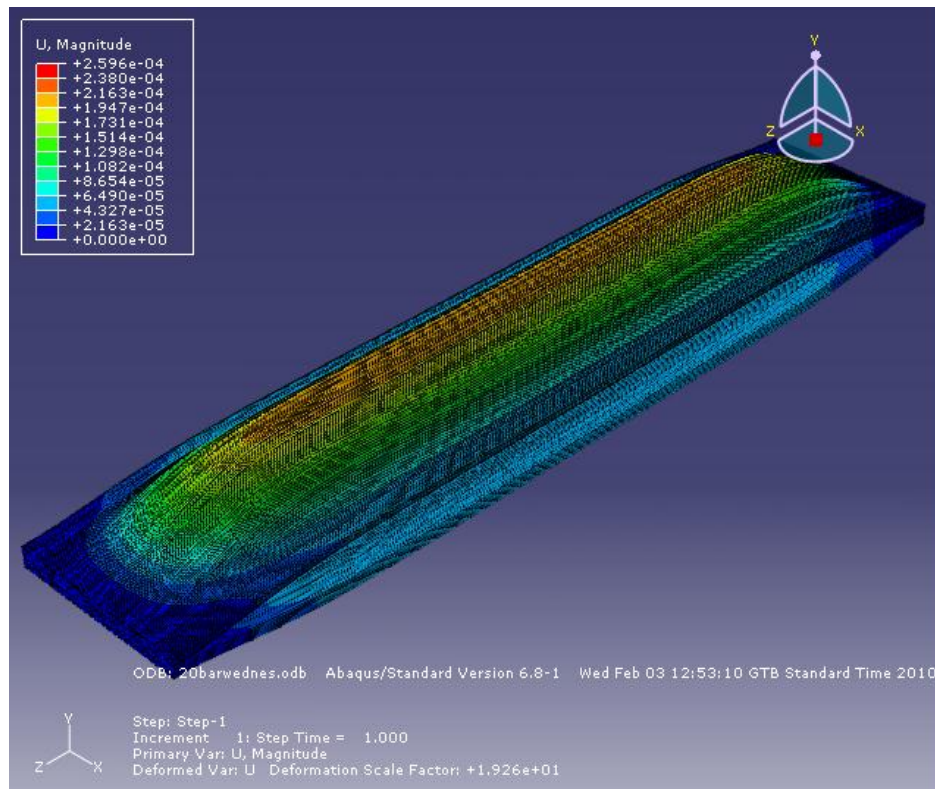


**Figure 4.31**– FEA displacement results for 20 bar interior pressure.

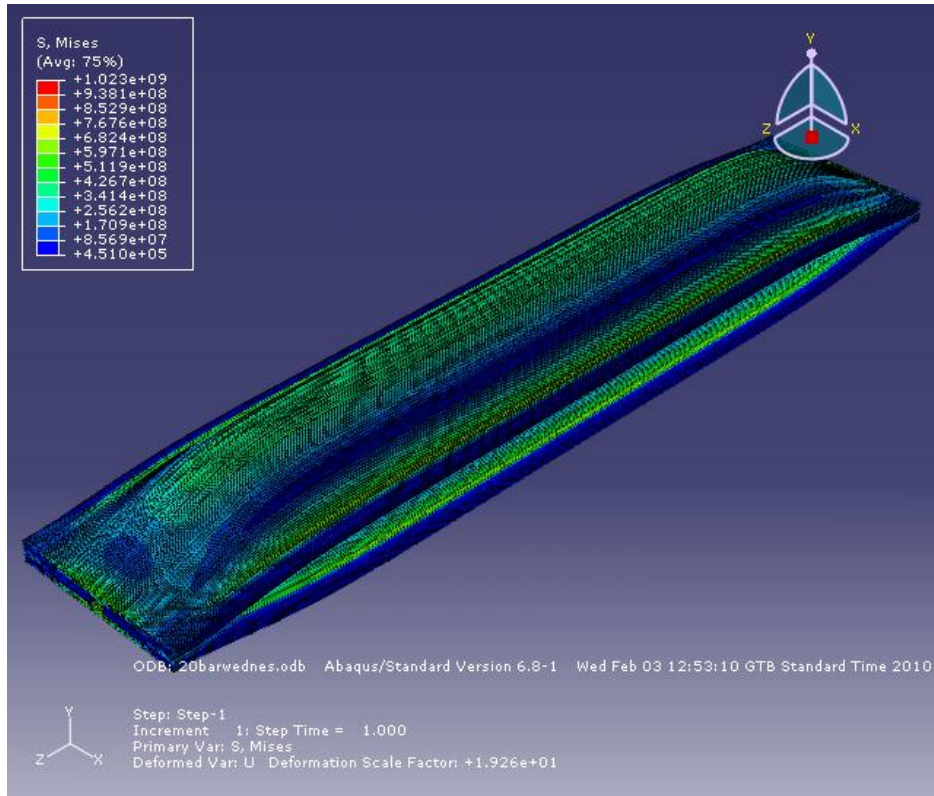


**Figure 4.32**– FEA stress results for 20 bar interior pressure

**Table 4.9** – Displacement solutions summary for corresponding interior pressure

<b>Analysis No:</b>	<b>Interior Pressure (bar)</b>	<b>Total Displacement (mm)</b>
1	1,0	0,0312
2	1,5	0,0470
3	2,0	0,0625
4	2,5	0,0778
5	3,0	0,0930
6	3,5	0,1082
7	4,0	0,1232
8	4,5	0,1381
9	5,0	0,1529
10	5,5	0,1677
11	6,0	0,1823
12	6,5	0,1969
13	7,0	0,2116
14	7,5	0,2263
15	8,0	0,2413
16	8,5	0,2563
17	9,0	0,2715
18	9,5	0,2874
19	10,0	0,3057

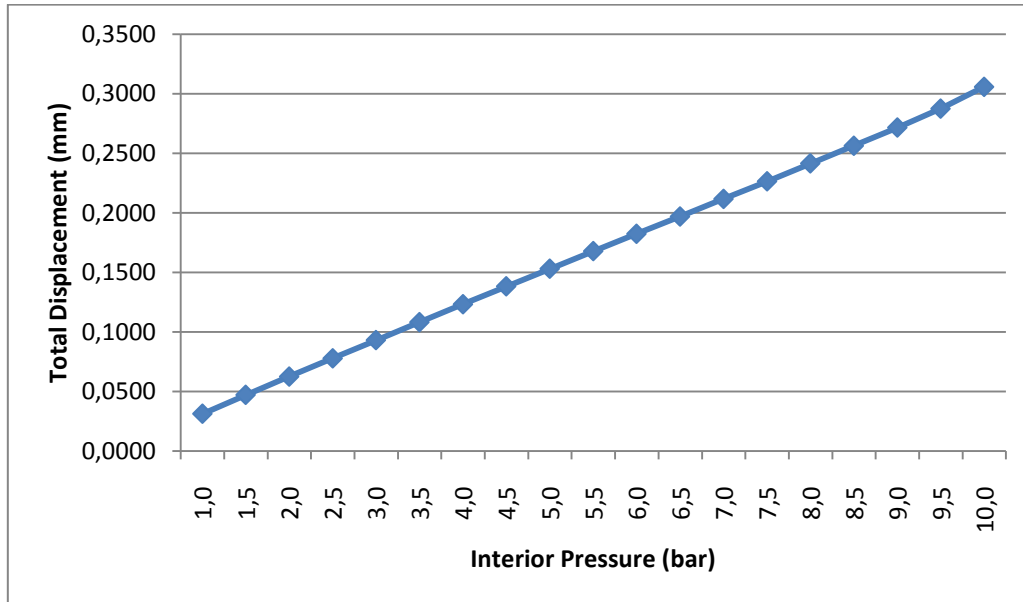


**Figure 4.33-** The trend of total displacement against interior pressure is almost linear

Solutions for the Design B indicates that, total displacement and maximum stress increase almost linearly with interior pressure. Moreover, the maximum stress values in the Design B are dramatically lower, and bellow cross section outperforms the former design. In the design A, 23.5 bar actuation pressure is needed to achieve 0.5 mm displacement, where maximum stress measures at 1.684GPa. Whereas, only 20 bar is required for the same displacement in the Design B, and maximum stress reduced to 1.023GPa which corresponds 40% reduction. For 5 bar pressure case, the maximum stress value is reduced to 227.5 MPa while achieving a 0.1127 mm displacement. When the interior pressure is 8.5 bar, we reach our displacement goal as 0.2563mm with 386.7 MPa. The actuator will be subjected to some local plastic deformation which means actuator will have limited service life which is expected. In the following section, fatigue life of the actuator Design B is investigated.

#### 4.4 LOW-CYCLE FATIGUE LIFE ESTIMATION OF THE ACTUATOR DESIGN B

Fatigue life of the actuator is another crucial design criterion, since the actuator will be subjected to stresses beyond the yield strength. Since operating stresses are sufficiently high to deform the material plastically, using strain based low-cycle fatigue models will be more practical and useful. In order to estimate number of cycles to failure Coffin-Manson low-cycle fatigue model has been used. Coffin-Manson analysis states that elastic part of the strain component can be approximated as;

$$\varepsilon_a^{el} = 1.75 \frac{\sigma_{UTS}}{E} N_f^{-0.12} \quad (4.5)$$

Where  $\varepsilon_a^{el}$  is the elastic strain component,  $\sigma_{UTS}$  is the ultimate tensile strength of material, E is the elastic modulus and  $N_f$  is the pertinent fatigue life. Plastic component of the strain amplitude is defined as;

$$\varepsilon_a^{pl} = 0.5D^{0.6}N_f^{-0.6} \quad (4.6)$$

where D is the ductility and defined as;

$$D \equiv \ln\left(\frac{A_0}{A_R}\right) \quad (4.7)$$

where  $A_R$  is the reduction of area. The strain amplitude can be defined as the sum of the plastic and elastic components, and we get the Coffin-Manson relationship as follows,

$$\varepsilon_a = 1.75 \frac{\sigma_{UTS}}{E} N_f^{-0.12} + 0.5D^{0.6} N_f^{-0.6} \quad (4.8)$$

The Coffin-Manson criterion includes three material parameters, i.e. ultimate tensile strength ( $\sigma_{UTS}$ ), elastic modulus (E), and ductility (D). Values of  $\sigma_{UTS}$  and E at 540 °C are obtained from Haynes 188 material datasheet [88] as 750 MPa and 197 GPa. Ductility of Haynes 188 is experimentally measured as presented in reference [92] as 0.1.

By iteratively solving equation 4.8 for  $N_f$  values ranging from 0 to  $10^6$  cycles, low cycle fatigue life curve is obtained as shown in Figure 4.34. Strain amplitude is calculated via finite element analysis. Following from Design B FE analysis, strain amplitude is 0.0052 when the interior pressure is 8.5 bar for a target 0.25 mm displacement. The corresponding cycle life of the actuator is calculated as 880 cycles as shown in Figure 4.34. Similarly, fatigue life at different pressure values are calculated and tabulated in Table 4.10.

Industrial gas turbines can be classified in 3 different groups in terms of operating mode. The “base load turbines” operate continuously year round with a couple of start-stop cycles annually. The “peaker gas turbines” start and stop roughly 5 times a week to support peak power load during week days. Some turbines in the third category are operated in “mixed mode”. The calculated 880 cycles fatigue life is sufficient to operate even a peaker unit for 3 years, and other turbines for much more service life. Depending on the turbine operating mode and desired service life Design B actuator can be used for higher actuation and displacement levels at the expense of reduced fatigue life.

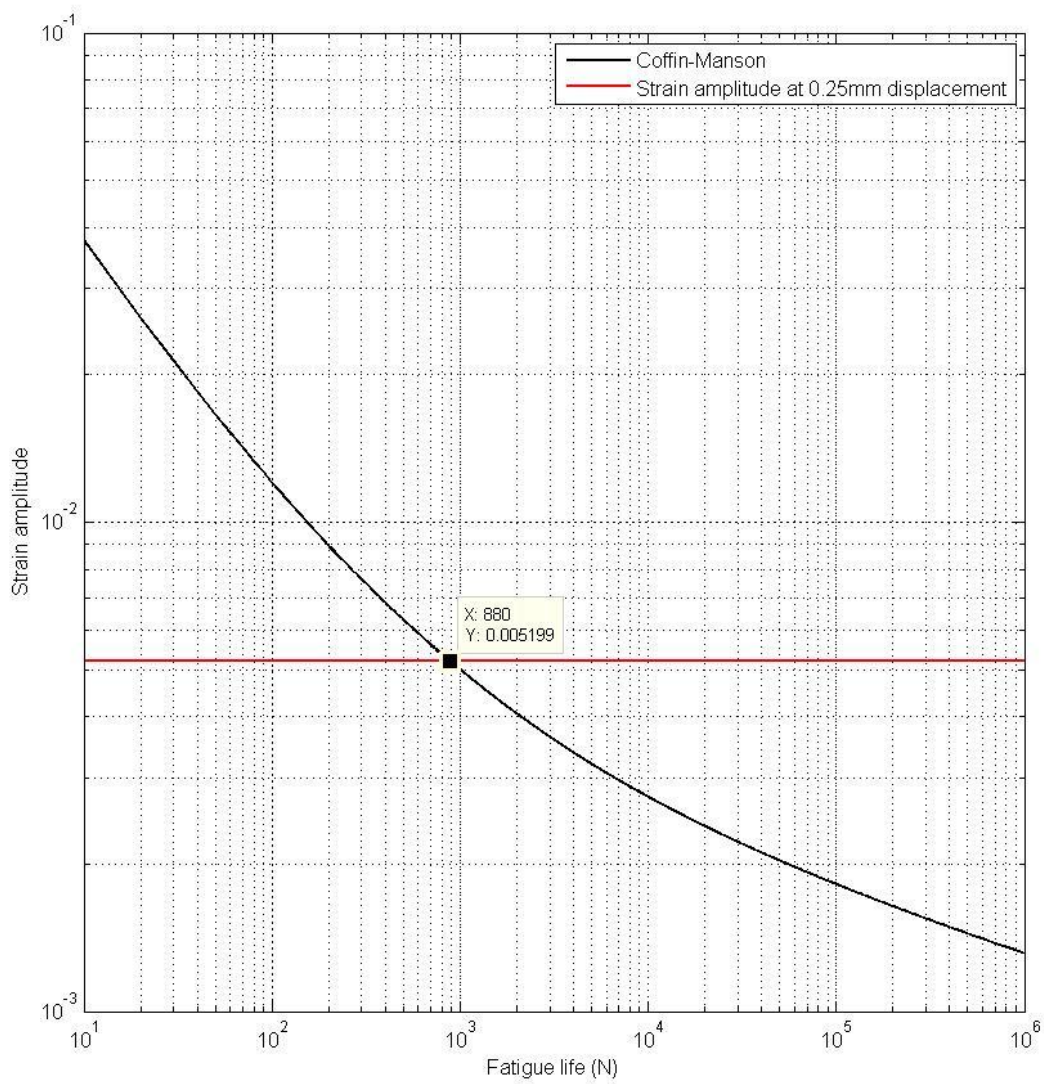


**Figure 4.34** – Low cycle fatigue life curve for actuator Design B

**Table 4.10** - Fatigue life of the actuator Design B with different pressure inputs

Interior Pressure (bar)	Displacement (mm)	Maximum Stress (MPa)	Life (Cycle)
6	0,1823	307,02	2920
7	0,2116	358,19	1720
8	0,2413	409,36	1120
8,5	0,2563	434,945	880
9	0,2715	460,53	780
10	0,3057	511,7	570
12	0,3741	614,04	330

In addition to the cyclic pressure load, actuator will be subjected to thermal cycling as well. Preliminary finite element analysis results indicated that thermal stresses remain very small (37.88 MPa), and occur near the holder-shim interface. Noting that maximum stress regions occur at mid section of each cell for pressure loading, thermal and pressure load driven strains appear to be decoupled. As thermal stresses are much smaller compared to pressure load stresses, a combined thermal and pressure load analysis has not been conducted.

## **CHAPTER 5**

### **ANALYSIS AND DESIGN VALIDATION**

Actuator response for different input pressures have been calculated by finite element analysis. According to the FEA results, deflection exhibits a linear trend with respect to inlet pressure. In order to validate the FEA results, a test rig has been designed and implemented (Figures 5.1-2). The rig allows an actuator cell to be pressurized, to inflate and push against a rod loaded with a dead weight simulating shroud load. The test piece is placed in a furnace where temperature can be controlled up to 1200°C. At the cooler side, motion of the push rod is detected to measure actuator displacement under work load at temperature. Different actuation cycles can be applied repeatedly by a programmable pressure control system. Samples can be cycled to failure under simulated engine conditions. Therefore, this test system allows for fatigue life verification as well.

#### **5.1 ACTUATOR TEST RIG DESIGN AND TEST PROCEDURE**

Test rig is composed of high temperature actuator, actuator connector, two rods, two pulleys, linear slide, displacement sensor, air inlet, deadweights and controller (Figures 5.1 and 5.2). With the aid of the control circuit's reference signal, proportional pressure regulator allows pressurized fluid through an air inlet. Air follows through a path in the rig as illustrated in Figure 5.3. Through air pressurization and depressurization cycle actuator sample is inflated and deflected. The actuator is in contact with the upper rod. Therefore upper rod is pushed towards the displacement sensor when actuator is pressurized. The rod is able to move only horizontally since it is connected to the rail of the linear slide. The car of the linear slide is fixed where the rail part is attached to the push rod, and able to move in horizontal axis.

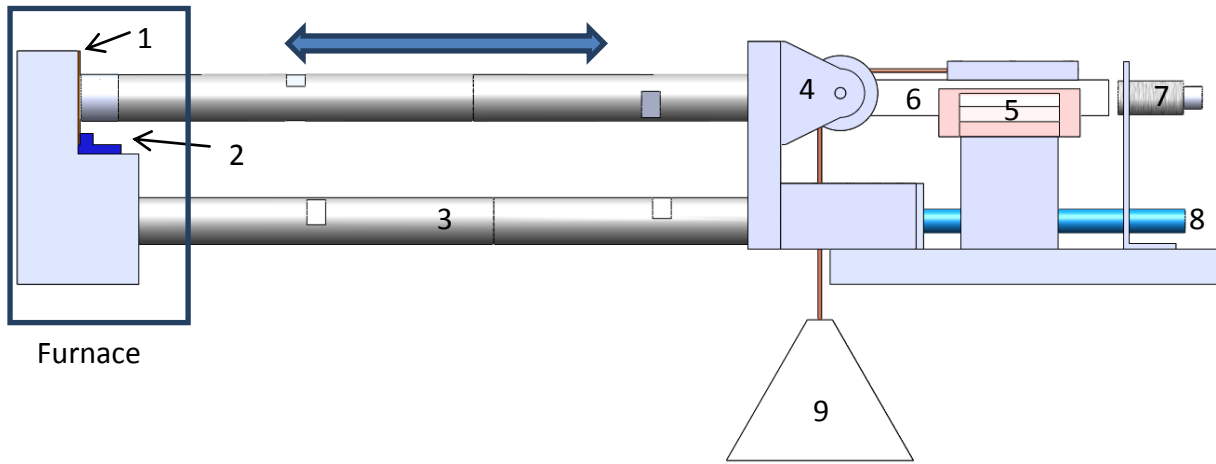


**Figure 5.1** Actuator test rig consists of; high temperature actuator (1), actuator connector (2), rods (3), two pulleys (4), linear slide – car (5), linear slide – rail (6), displacement sensor (7) , air inlet (8) and dead weight (9)

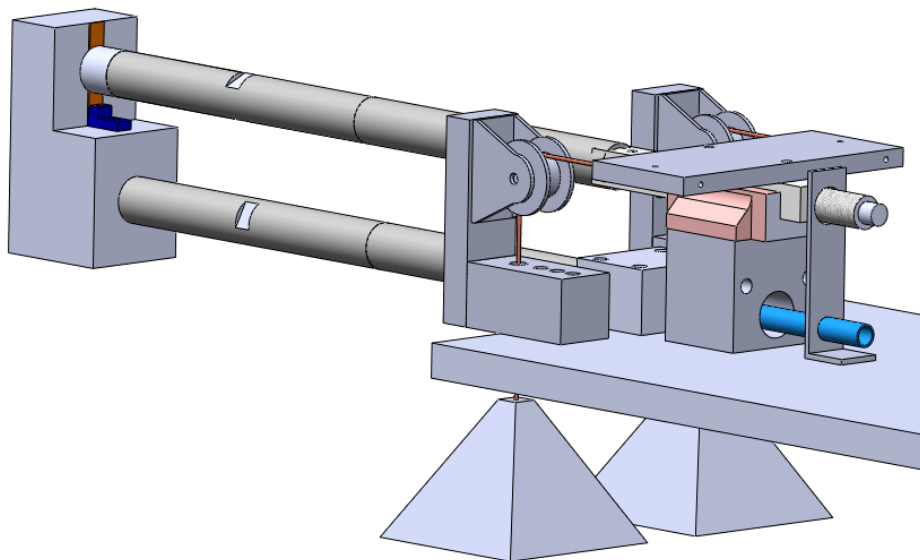


**Figure 5.2-** Isometric view of the actuator test rig

As mentioned before, the actuator will be used to lift the shrouds in gas turbines. To simulate a sample shroud load on the actuator, two 20 kg dead weights are used. Two pulleys allow for horizontal loading of the test piece by changing direction of the applied weight load

from vertical to horizontal. As a result, a load of 40 kg is exerted on the actuator simulating 400 N shroud operating pressure load.. Moreover, the operating temperature at the shroud location, 540 °C, is also simulated with a furnace. Test temperature is maintained by placing the actuator assembly in a furnace, and by drilling the furnace cover and inserting connecting rods through two small holes. The amount of deflection under the operating load and temperature conditions is measured via a displacement sensor positioned on the other side of the rail.

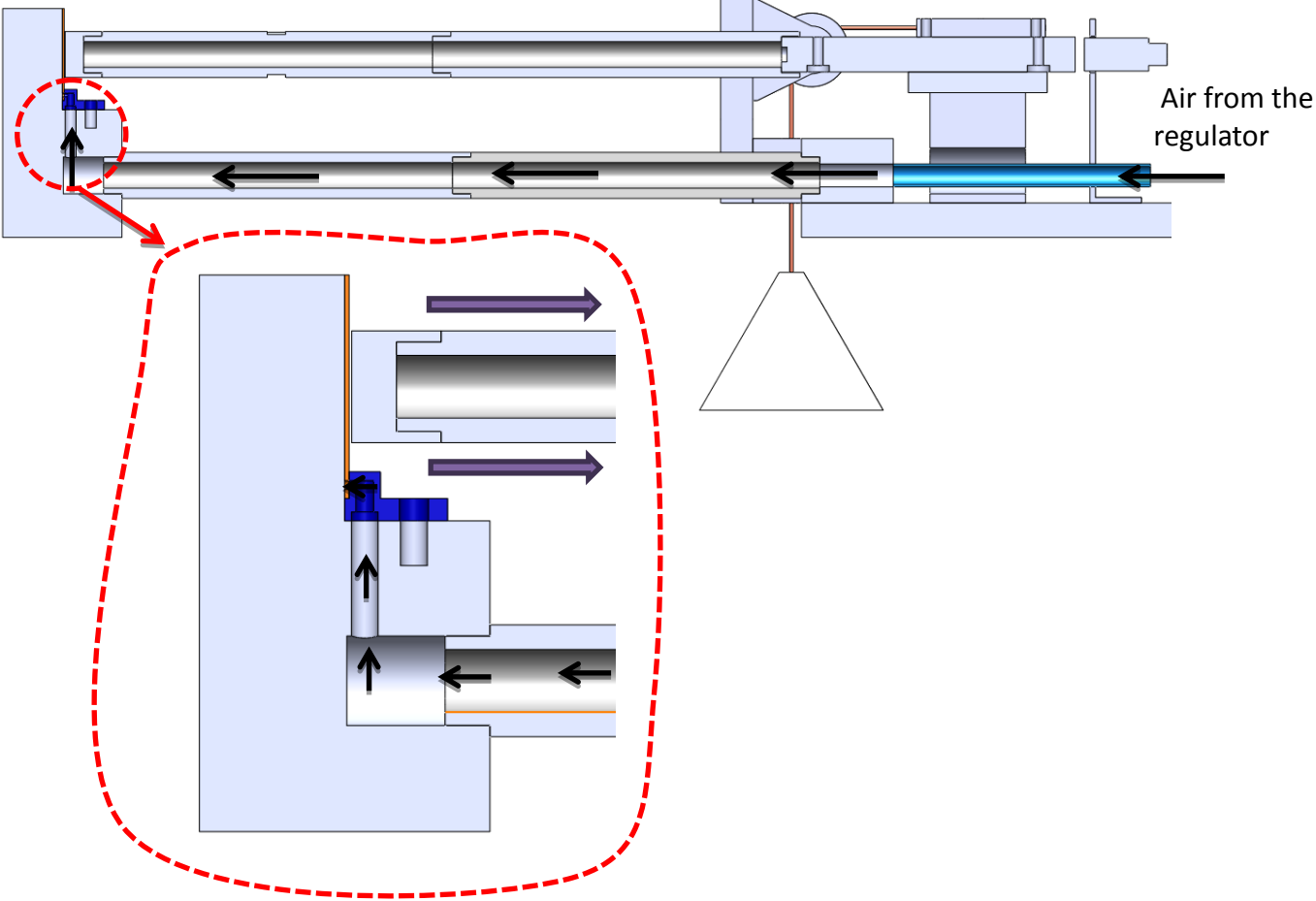


**Figure 5.3** – Pressurized air’s path from the pressure regulator to the actuator.

To compare validate finite element analysis results, interior pressure values (listed in Table 3.9) will be used ranging from 1 to 7 bars. Displacement data for corresponding to these pressure inputs will be recorded for comparison.

## 5.2 CONTROLLER DESIGN

Various control methods have been studied to design a controller circuit regulating actuation pressures and applying prescribed mission cycles. Both linear and non-linear control methods can be used in the system to track the reference. Proportional Integral Derivative Control (PID), Lead-Lag Controller, State Variable Feedback and Optimal Control can be given as examples of linear control algorithms. Through appropriate assumptions, system can be modeled by either Ordinary Differential Equations (ODE), or using Partial Differential Equations (PDE). Both ODEs and PDEs are usually non-linear, and they can be linearized to be used in a linear control algorithm. To name a few for non-linear algorithms, Feedback Linearization, Integral Backstepping, Sliding Mode Control, Adaptive Control and Lyapunov-based controllers can be listed. Non-linear control algorithms are usually complex and their applications are more expensive.

For precision position control, both linear and non-linear algorithms can be used. Linear control algorithms have simple structure, and they provide relatively low-cost solutions. Linear controllers such as PID or lead-lag can easily be designed for “Single Input Single Output” (SISO) systems by using classical control methods. However, for “Multi Input Multi Output” (MIMO) systems, one can prefer state feedback and optimal control algorithms since they can be designed easily in state space. For our case, PID control has been selected to be used.

### 5.2.1 Proportional Integral Derivative Control (PID)

PID controllers have a rich history with first studies conducted during early 20th century. Details about the background of PID controllers can be found in references [93-95]. PID control has numerous applications like ecological and biological systems, smart house designs, transportation, military vehicle systems etc. Theoretical background of these applications are available in open literature [96-105]. PID control units can be found in various forms, namely; autonomous, part of the hierarchical structure, distributed control systems and integrated systems. Although derivative component is not used often, in definition it is widely known as Proportional Integral Derivative Control.

There are two different approaches in the closed-loop PID controlled systems. Control signal “u” could be directly generated based on the error, “e” (Figure 5.4a), or alternatively, it is being controlled by mere error integration instead of proportional and derivative actions (Figure 5.4b).

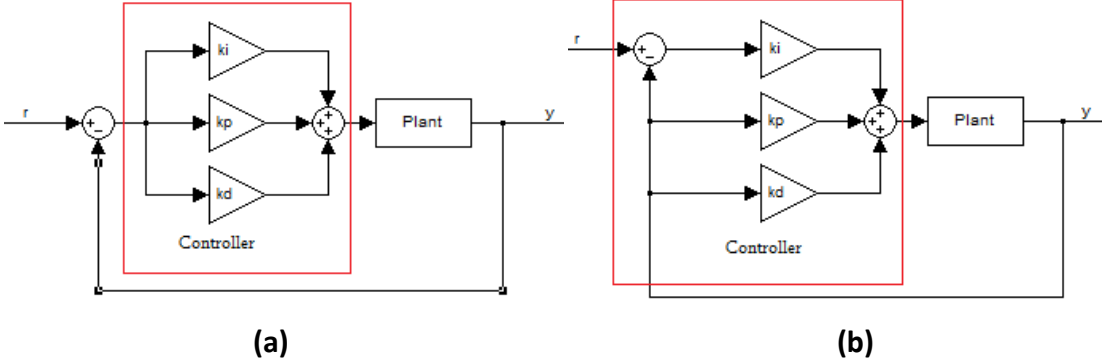


**Figure 5.4** (a) PID controller with error feedback (b) PID controller with 2 degrees of freedom

Ideally, a PID controller unit with error feedback that relates input and output signals can be defined as follows;

$$u = k_p e + k_i \int_0^t e(\tau) d\tau + k_d \frac{de}{dt} = k_p \left( e + \frac{1}{T_i} \int_0^t e(\tau) d\tau + T_d \frac{de}{dt} \right) \quad (4.1)$$

Control action can be defined as the sum of proportional feedback, integral and derivative terms. The control parameters can be listed as proportional gain  $k_p$ , integral gain  $k_i$  and derivative gain  $k_d$ .

**5.2.2 Control Circuit and Microcontroller**

In this work sensor-controller-actuator system is composed of compressor, compressed air dryer, control circuit, proportional pressure regulator, custom design actuator and distance sensor (Figure 5.5).

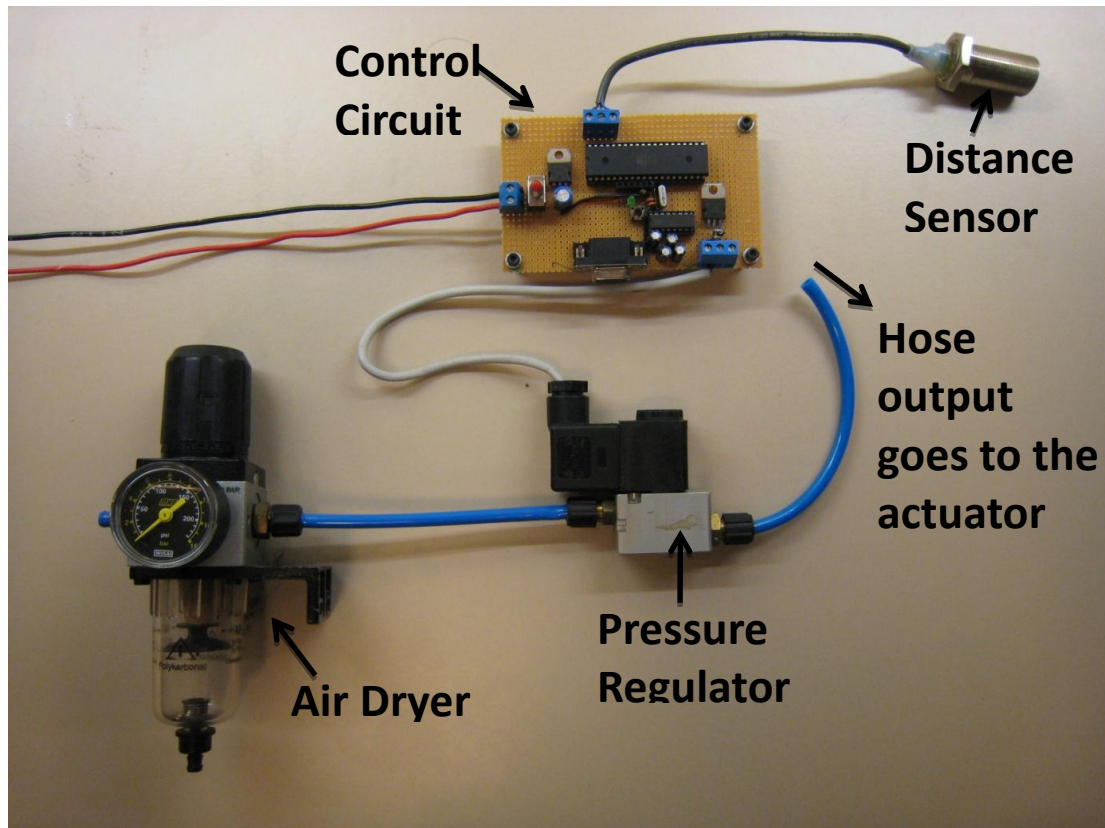


**Figure 5.5** – Electronic Control System

Compressed air dryer dehumidifies the air that comes from the compressor, pre-regulates the air pressure and outputs the dry air to the electro-pneumatic proportional pressure regulator. Pressure regulator is capable of regulating the air pressure from 0 to 10 bar and desired pressure output can be adjusted proportionally with a reference voltage which varies from 0 to 10V. The solenoid valve inside the regulator sets its position for the desired output pressure with the aid of the reference voltage. After that, regulated pressure is applied to the pipe to pressurize the actuator and actuator will inflate. Therefore, actuator will push upper rod loaded with deadweights towards the distance sensor, and displacement will be measured by the distance sensor for different input pressure values. Experimental data are necessary for comparison with finite element analysis results for the deflection and actuator fatigue life.

Control system adjusts the pressure input to the system with the aid of reference voltage. PIC16F877A is selected as the microcontroller, and it is capable of executing 5000 instructions per second. It has 40pins, 256bytes of EEPROM data memory, ICD, two comparators, 8 channels of 10-bit-Analog-to-Digital (A/D) converter and 2

capture/compare/PWM functions. PIC can be programmed by one of C, JAL or Assembly programming languages.

Schematic design of the control circuit is presented at Figure 5.6. The operating frequency of the microcontroller is set by crystal as 4Mhz. Analog signal from the pressure sensor is converted to digital with A/D module in the PIC. Then, digital data is compared with the reference signal that arises from an independent power supply. Error is calculated by subtracting the reference and sensor signals. After that, derivative and integral of the error are computed and control signal is calculated according to equation 5.1. Microcontroller is programmed with C and compiled by CCSC. Control signal between 0-5V, is outputted from the related pin to a low pass filter, and PWM signal is converted to analog signal again. Pressure regulator needs 0-10V input reference voltage. Therefore, signal amplitude is increased 2 times by a rail-to-rail op-amp.

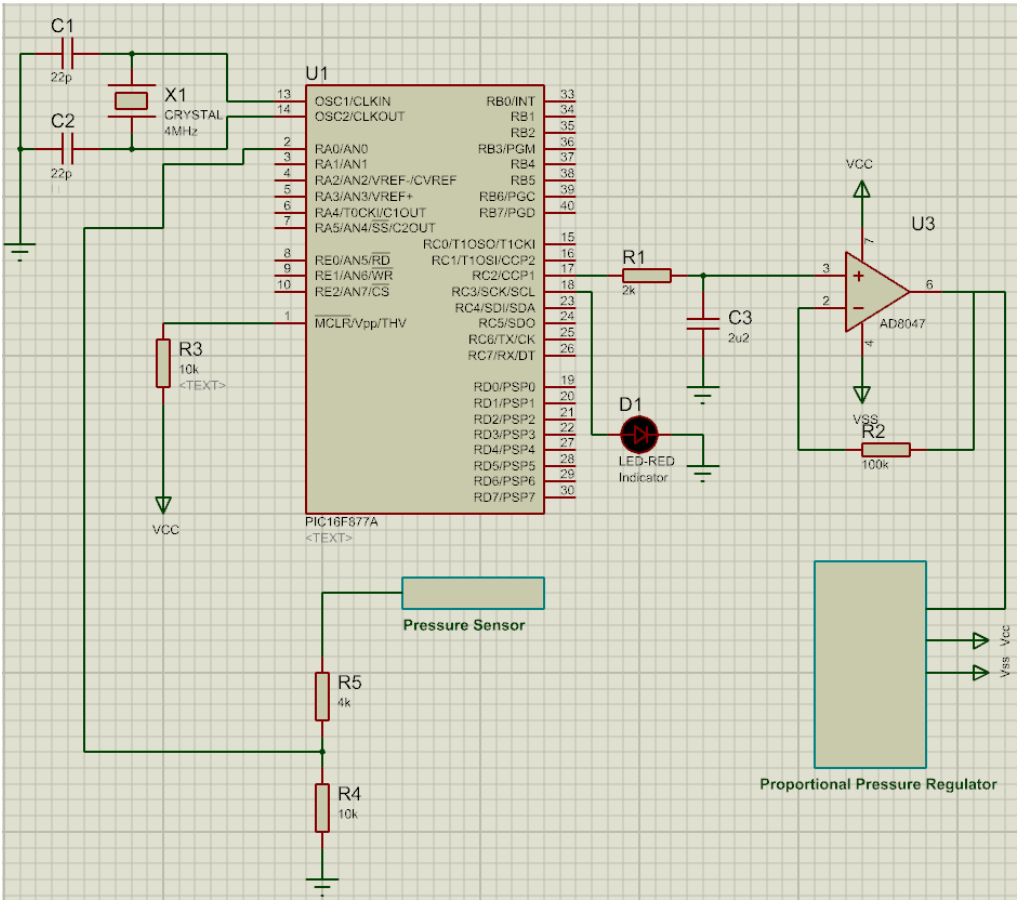


Figure 5.6 - Schematic design of the control circuit

### 5.3 FABRICATION OF THE ACTUATOR PROTOTYPE

Actuator prototype of Design B is manufactured by simply stacking thin sheets and welding them from the specific locations as shown in Figure 5.7. Since the actuator will be exposed to high temperature, welding type is critically important. In applications that require precision, quality and reliability in joining of thin sections Electron beam welding (EBW) is preferred. In this method, a beam of high velocity electrons are sent to the desired locations. Kinetic energy of the electrons is transformed to heat upon impact which leads to an increase in the temperature over the welding location. Therefore, impact locations are melted and plates merge after the solidification.

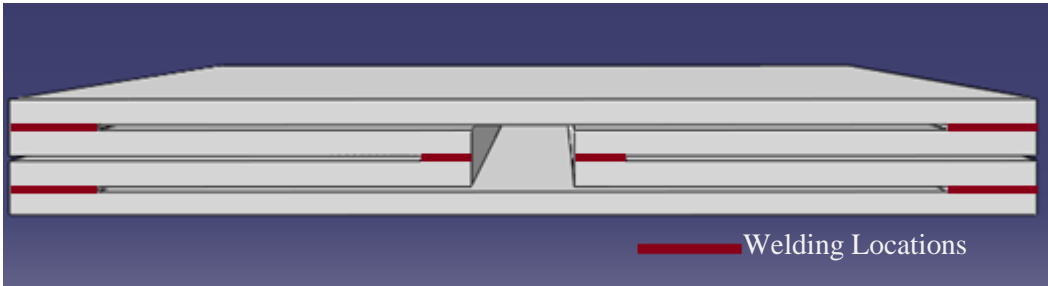


Figure 5.7 – Welding locations of the actuator

The other issue involving actuator fabrication is the inlet fixture to allow actuation air in the actuator, and to physically attach it to the test setup. Actuator is assembled to test rig via a custom design connector which allows air passage to the actuator. Actuator is welded to the connector from the edges that are highlighted in Figure 5.8.

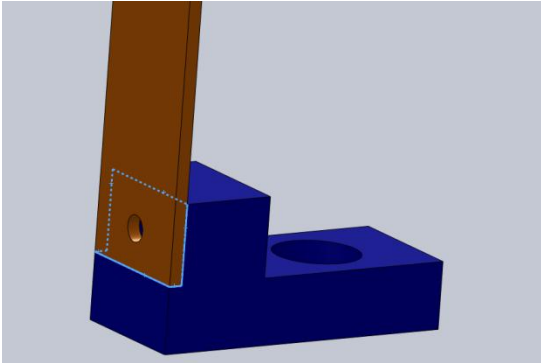


Figure 5.8– Actuator is connected to the test rig and fixed by the connector shown in blue.

During the manufacturing phase of the actuator, a lot of difficulties have been faced. The existing EBW system in a military facility in Eskisehir could not be used due to military use restrictions. Repeated attempts to fabricate elsewhere in Turkey via other techniques, like plasma welds, have failed in weld quality due to very thin sections. Quotes from abroad to fabricate 10 prototype actuator cell samples were too high (38000 USD) compared to available school funds. Therefore, actuator pressure tests have been abandoned.

## CHAPTER 6

### CONCLUSION

To achieve better efficiency and higher power, turbine blade tip clearance has to be controlled. Active clearance control (ACC) aims to improve efficiency in gas turbines by decreasing the tip clearance leakage. This work aims to design and develop a novel high temperature actuator system that is applicable and retrofitable to most of the current operating turbines with no major modifications on the turbine design. Design goal is to control tip clearance up to 0.25mm actuation stroke that leads to possible 1% efficiency gain.

Two different actuator designs have been analyzed for deflection and stress under different interior pressure values. Although very simple, Design A that consists of two plates positioned one on the top of other and welded along the edges exhibited very limited displacement capability. The alternate Design B with convoluted bellow-like structure allows for more displacements while dramatically reducing maximum stress values. In order to achieve 0.5 mm displacement, an actuation pressure of 20 bar is needed with maximum stress at 1.023GPa which corresponds to 40% decrease over Design A. A detailed materials selection procedure has been followed. Haynes 188 has been selected as the actuator material due to its favorable friction and wear characteristics observed during high temperature tests. Haynes 188 has 290MPa yield strength at 540°C. When actuated with 8.5 bar internal pressure, Design B achieves a displacement of 0.2563mm with 386.7MPa maximum stress. With maximum stress levels beyond material yield local plastic deformations are expected. Although repeated attempts have been made, Design B actuator could not be successfully manufactured. Therefore, actuator life has been calculated using low cycle fatigue models. Analyses using Coffin-Manson low-cycle fatigue method indicated that actuator will have a life of 880 cycles of life while it can sustain repeated 0.25 mm displacement. Considering that a peaker gas turbine can experience 260 cycles a year, 880 actuator cycles provide 3 years of field service with 0.25 mm deflection offering a potential 1% efficiency increase. Therefore, actuator Design B is considered successful. Service life can be much longer in base load units where more displacements and efficiency gain can be achieved at the expense of cycle life.

Future work in this subject may include actual fatigue testing of the actuator samples upon successful manufacturing. Various design configurations can be explored to further

reduce material stresses and to increase displacement capability. Eventual goal is to conduct actual engine tests to demonstrate efficiency gain potential.

## REFERENCES

1. Giampaolo, "Gas Turbine Hand Book, Principles and Practices", TJ778.G48, 2006
2. N.A., "General Electric 7A industrial gas turbine", retrieved from: <http://www.ge-7fa.com>, on 2009
3. N.A., "Gas turbine", retrieved from: <http://en.wikipedia.org>, on 2010
4. Lane, D., "Brayton Cycle: The ideal cycle for gas-turbine engines in relation to power plants", n.d.
5. Hazard, H.R., Sawyers' gas turbine engineering Handbook, vol.1, 1985
6. Aeronautical Technologies for the 21st Century, National Research Council (US) Committee on Aeronautical Technologies, 1992
7. Halila, E.E., Lenahan, D.T., Thomas, T.T., "Energy Efficient Engine, High Pressure Turbine Test Hardware Detailed Design Report," NASA CR-167955, 1982.
8. Gaffin, W.O., "JT9D-70/59 Improved High Pressure Turbine Active Clearance Control System," NASA CR-159661, 1979.
9. Fasching, W.A., "CF6 Jet Engine Performance Improvement Summary Report," NASA CR-165612, 1982.
10. Ciokajlo, J.J., "Blade Tip Clearance Control Apparatus Using Shroud Segment Annular Support Ring Thermal Expansion," U.S. Patent 5,116,199, 1992.
11. Paprotna, H.E., Foust, A.M., "System For Actively Controlling Compressor Clearances," U.S. Patent 7,434,402 B2, 2008
12. Carpenter, K.D., Wiedemer, J.D., Smith, P.A., "Rotor Blade Outer Tip Seal Apparatus," U.S. Patent 5,639,210, 1997.
13. US Patent 5,456,576; Lyon, Bruce V., Dynamic Control of Tip Clearance, 1995.
14. Catlow, R., "Blade Tip Clearance Control Apparatus," U.S. Patent 5,211,534, 1993.
15. US Patent 5,211,534; Catlow, Ronald, Blade Tip Clearance Control Apparatus, 1993.
16. Wardle, R.L., "Floating Blade Shrouds," U.S. Patent 2,927,724, 1960.
17. Huber, F.W., Dietrich, D.J., "Clearance Control for the Turbine of a Gas Turbine Engine," U.S. Patent 5,667,359, 1997.
18. US Patent 5,054,997; Robert J. Corsmeier; Joseph Petsche, "*Blade Tip Clearance Control Apparatus Using Bellcrank Mechanism*", 1991.

19. Aeronautical Technologies for the 21st Century, National Research Council (US) Committee on Aeronautical Technologies, 1992 Bruce M. Steinetz.
20. Lattime, S.B., Steinetz B.M., “*Evaluation of an Active Clearance Control System Concep*,” NASA TM-213856, 2005
21. Steinetz B.M., Taylor S.C., “*Further Characterization of an Active Clearance Control Concept*” NASA TM-215039, 2007.
22. John H., “*Technical Support Package for High-Temperature SMAS For Actuator Applications*” LEW-18054-1, 2008.
23. DeCastro, J.A., Melcher K.J., “*System-Level Design of a Shape Memory Alloy Actuator for Active Clearance Control in the High-Pressure Turbine*” NASA/TM-213834, 2005.
24. H.E. Sliney, *Solid lubricant materials for high temperatre---a review*, Tribology International, 1982, vol. 15, pp. 303-315.
25. I.M. Allam, *Solid lubricants for applications at elevated temperatures—a review*, Journal of material sciences, 1991, vol. 26, pp. 3997-3984.
26. T. Hoornaert, Z.K. Hua, J.H. Zhang,”*Hard wear-resistant coating: A review*”, 2010, Part 3, pp. 774-9
27. Kato, K. Noritsugu, U., Koshi, A., “*Friction, wear and N<sub>2</sub>-lubrication of carbon nitride coating: a review*”, Wear, 2003, vol. 253, pp.1062-9.
28. N.E.W. “*Hartley, Friction and wear of ion-implanted metal – A review*” , Thin solid films, 1979, vol 64, issue 2, pp. 177-90.
29. A. Schallamach, “*Recent advances in knowledge of rubber friction and tire wear*”, Rubber Chem. Technol., 1968, vol. 41.
30. N.A., “*Literature review: Effect of surface texturing on friction and wear for sliding surfaces.*”
31. R.J.K Wood, “*Tribo-corrosion of coatings: a review*”, J. Phys, 2007, vol.40, pp. 5502-21
32. J. Lu, Q. Xue, *Sliding friction, wear and oxidation behavior of CeF<sub>3</sub> compact in sliding against steels at temperatures 700<sup>0</sup>C in air*, Wear, 1998, vol. 219, pp. 73-77.
33. J. Lu, Q. Xue, G. Zhang, *Effect of silver on the sliding friction and wear behavior of CeF<sub>3</sub> compact at elevated temperatures*, Wear, 1998, vol. 214, pp. 107-111.
34. P.J. John, S.V. Prasad, A.A. Voevodin, J.S. Zabinski, *Calcium sulfate as a high temperature solid lubricant*, Wear, 1998, vol. 219, pp. 155-161.
35. D. Jianxin, *Friction and wear behavior of Al<sub>2</sub>O<sub>3</sub>/TiB<sub>2</sub>/SiC<sub>w</sub> ceramic composites at temperatures at 800<sup>0</sup>C*, Ceramics international, 2001, vol. 27 pp. 135-141.

36. J.H. Ouyang, S. Sasaki, K. Umeda, *The friction and wear characteristics of low-pressure plasma-sprayed ZrO<sub>2</sub>-BaCrO<sub>4</sub> composite coating at elevated temperatures*, Surface and coating technology, 2002, vol. 154, pp. 131-139.
37. J.H. Ouyang, S. Sasaki, T. Murakami, K. Umeda, *Tribological properties of spark-plasma-sintered ZrO<sub>2</sub>(Y<sub>2</sub>O<sub>3</sub>)-CaF<sub>2</sub>-Ag composites at elevated temperatures*, Wear, 2005, vol. 258, pp. 1444-1454.
38. J.H. Ouyang, S. Sasaki, *Microstructure and tribological characteristics of ZrO<sub>2</sub>-Y<sub>2</sub>O<sub>3</sub> ceramic coating deposited by laser-assisted plasma hybrid spraying*, Tribology international, 2002, vol. 35, pp. 255-264.
39. J.H. Ouyang, S. Sasaki, T. Murakami, K. Umeda, *Spark-plasma-sintered ZrO<sub>2</sub>(Y<sub>2</sub>O<sub>3</sub>)-BaCrO<sub>4</sub> self-lubricating composites for high temperature tribological applications*, Ceramics international, 2005, vol. 31, pp. 543-553.
40. J.H. Ouyang, S. Sasaki, *Tribological characteristics of low-pressure plasma-sprayed Al<sub>2</sub>O<sub>3</sub> coating from room temperature to 800<sup>0</sup>C*, Tribology international, 2005, vol. 38, pp. 49-57.
41. J.H. Ouyang, T. Murakami, S. Sasaki, *High-temperature tribological properties of a cathodic arc ion-plated (V,Ti)N coating*, Wear, 2007, vol. 263, pp. 1347-1353.
42. J.H. Ouyang, Y.F. Li, Y.M. Wang, Y. Zhou, T. Murakami, S. Sasaki, *Microstructure and tribological properties of ZrO<sub>2</sub>(Y<sub>2</sub>O<sub>3</sub>) matrix composites doped with different solid lubricants from room temperature to 800<sup>0</sup>C*, Wear, 2009, vol. 267, pp. 1353-1360.
43. L. Yao-hui, D. Jun, Y. Si-rong, W. Wei, *High temperature friction and wear behaviour of Al<sub>2</sub>O<sub>3</sub> and/or carbon short fibre reinforced Al-12Si alloy composites*, Wear, 2004, vol. 256, pp. 275-285.
44. G. Lopez, M.H. Staia, *High-temperature tribological characterization of zirconium nitride coatings*, Surface & coatings technology, 2005, vol. 200, pp. 2092-2099.
45. T. Polcar, T. Kubart, R. Novak, L. Kopecky, P. Siroky, *Comparison of tribological behaviour of TiN, TiCN, CrN at elevated temperatures*, Surface & coating technology, 2005, vol. 193, pp. 192-199.
46. T. Polcar, N.M.G. Parreira, R. Novak, *Friction and wear behaviour of CrN coating at temperatures up to 500<sup>0</sup>C*, Surface & coating technology, 2007, vol. 201, pp. 5228-5235.
47. T. Polcar, T. Vitu, L. Cvrcek, J. Vyskocil, A. Cavaleiro, *Effects of carbon content on the high temperature friction and wear of chromium carbonitride coatings*, Tribology international, vol.
48. J.L. Li, D.S. Xiong, M.F. Huo, *Friction and wear properties of Ni-Cr-W-Al-Ti-MoS<sub>2</sub> at elevated temperatures and self-consumption phenomena*, Wear, 2008, vol. 265, pp. 566-575.

49. J. Li, D. Xiong, Z. Huang, J. Kong, J. Dai, *Effect of Ag and CeO<sub>2</sub> on friction and wear properties of Ni-base composite at high temperature*, *Wear*, 2009, vol. 267, pp. 576-584.
50. Z. Ruijun, W. Hong, L. Yanjie, *High temperature friction and wear performances of Ti/Cu-doped carbonaceous mesophases*, *Tribology international*, 2009, vol. 42, pp. 657-661.
51. S. Zhang, J. Zhou, B. Guo, H. Zhou, Y. Pu, J. Chen, *Friction and wear behaviour of laser cladding Ni/hBN self-lubricating composite coating*, *Materials science and engineering*, 2008, vol. A491, pp. 47-54.
52. Q. Bi, W. Liu, J. Yang, J. Ma, Q. Xue, *Tribological properties of Ni-17.5Si-29.3Cr alloy at room and elevated temperatures*, *Tribology international*, 2010, vol. 43, pp. 136-143.
53. P.A. Benoy, C. DellaCorte, *Tribological characteristics of sputtered Au/Cr films on alumina substrates at elevated temperature*, DOE/NASA/50306-3, 1993, NASA TM-106078.
54. J.A. Laskowski, C. DellaCorte, *Friction and wear characteristics of candidate foil bearing materials from 25<sup>0</sup>C to 800<sup>0</sup>C* DOE/NASA/50306-11, 1996, NASA TM-107082.
55. C. DellaCorte, B.J. Edmonds, *Preliminary evaluation of PS300: A new self-lubricating high temperature composite coating for use to 800<sup>0</sup>C*, DOE/NASA/50306-8, 1996, NASA TM-107056.
56. C. DellaCorte, *The effect of counterface on the tribological performance of a high temperature solid lubricant composite from 25 to 650<sup>0</sup>C*. *Surface and coatings technology*, 1996, vol. 86-87, pp. 486-492.
57. C. DellaCorte, B.J. Edmonds, *NASA PS400: A new high temperature solid lubricant coating for high temperature wear applications*, NASA/TM, 2009, 215678.
58. O. Barrau, C. Boher, R. Gras, F. Rezai-Aria, *Analysis of the friction and wear behaviour of hot work tool steel for forging*, *Wear*, 2003, vol. 255, pp. 1444-1454.
59. O. Barrau, C. Boher, R. Gras, F. Rezai-Aria, *Wear mechanisms and wear rate in a high temperature dry friction of AISI H11 tool steel: Influence of debris circulations*, *Wear*, 2007, vol. 263, pp. 160-168.
60. Q. Yang, T. Senda, N. Kotani, A. Hirose, *Sliding wear behaviour and turbofilm formation of ceramics at high temperatures*, *Surface coating and technology*, 2004, vol. 184, pp. 270-277.
61. J. Hardell, E. Kassfeldt, B. Prakash, *Friction and wear behaviour of high strength boron steel at elevated temperatures up to 800<sup>0</sup>C*, *Wear*, 2008, vol. 264, pp.788-790.
62. J.Hardell, B. Prakash, *High temperature friction and wear behaviour of different tool steels during sliding against Al-Si coated high-strength steel*, *Tribology international*, 2008, vol. 41, pp. 663-671.

63. S. Taktak, S. Ulker, I. Gunes, *High temperature wear and friction properties of duplex surface treated bearing steels*, Surface and coating technology, 2008, vol. 202, pp. 3367-3377.
64. E. Arslan, Y. Totik, O. Bayrak, I. Efeoglu, A. Celik, *High temperature friction and wear behavior of MoS<sub>2</sub>/Nb coating in ambient air*, J. Coat. Technol, 2010, vol. 7, pp. 131-137.
65. B.S. Mann, B. Prakash, *High temperature friction and wear characteristics of various coating materials for steam valve spindle application*, Wear, 2000, vol. 240, pp. 223-230.
66. H. Kumar, V. Ramakrishnan, S.K. Albert, C. Meikandamurthy, B.V.R. Tata, A.K. Bhaduri, *High temperature wear and friction behaviour of 15Cr-15Ni-2Mo titanium-modified austenitic stainless steel in liquid sodium*, Wear, 2010, Article in press.
67. N.J. Barnick, T.A. Blanchet, W. G. Sawyer, J.E. Gardner, *High temperature lubrication of various ceramics and metal alloys via directed hydrocarbon feed gases*, Wear, 1998, vol. 214, pp. 131-138.
68. W.G. Sawyer, T.A. Blanchet, *Vapor-phase lubrication in combined rolling and sliding contacts: modeling and experimentation*, Transactions of ASME, 2001, DOI:10.1115/1.1308039.
69. J.L. Lauer, T.A. Blanchet, B.L. Vlcek, B. Sargent, *Lubrication of Si<sub>3</sub>N<sub>4</sub> and steel rolling and sliding contacts by deposits of pyrolyzed carbonaceous gases*, Surface and coating technology, 1993, vol. 32, P. 339-405
70. T.A. Blanchet, J.L. Lauer, Y.F. Liew, S.J. Rhee, W.G. Sawyer, *Solid lubrication by decomposition carbon monoxide and other gases*, Surface and coating technology, 1994, vol. 68, P. 446-452
71. B.F. Hanyaloglu, E.E. Graham, T. Oreskovic, C.G. Haji, *Vapor phase lubrication of high temperature alloys*, Lubrication engineering, 1995, vol. 51, pp. 503-508.
72. W.G. Sawyer, T.A. Blanchet, S.J. Calabrese, *Lubrication of silicon nitride in a simulated turbine exhaust gas environment*. Tribology transactions, 1997, vol. 40, pp. 374-380.
73. W. Wang, *Application of a high temperature self-lubricating composite coating on steam turbine components*, Surface and coating technology, 2004, vol. 177-178, pp. 12-17.
74. Q. Xue, J. Lu, *Physical and chemical effects of CeF<sub>3</sub> compact in sliding against hastelloy C in temperatures to 700<sup>0</sup>C*, Wear, 1997, vol. 211, pp. 9-14.
75. J. Lu, Q. Xue, J. Ouyang, *Thermal properties and tribological characteristics of CeF<sub>3</sub> compact*, Wear, 1997, vol. 211, pp. 15-21.
76. P.J. John, J.S. Zabinski, *Sulfate based coatings for use as high temperature lubricants*, Tribology letter, 1999, vol. 7, pp. 31-37.

77. J.H. Ouyang, S. Sasaki, *Unlubricated friction and wear behavior of low-pressure plasma-sprayed ZrO<sub>2</sub> coating at elevated temperatures*, *Ceramics international*, 2000, vol. 27, pp. 251-260.
78. M.H. Staia, Y. Perez-Delgado, C. Sanchez, A. Castro, E. Le Bourhis, E.S. Puchi-Cabrera, *Hardness properties and high-temperature wear behaviour of nitride AISI D' tool steel, prior and after PAPVD coating*, *Wear*, 2009, vol. 267, pp. 1452-1461.
79. X.D. Lu, H.M. Wang, *High-temperature sliding wear behaviours of laser clad Mo<sub>2</sub>Ni<sub>3</sub>Si/NiSi metal silicide composite coatings*, *Appl. Surf. Sci.*, 2003, vol. 214, pp. 190-195.
80. X.D. Lu, H.M. Wang, *High-temperature phase stability and tribological properties of laser clad Mo<sub>2</sub>Ni<sub>3</sub>Si/NiSi metal silicide composite coatings*, *Acta Mater*, 2004, vol. 52, pp. 5419-5426.
81. Y.L. Fang, H.M. Wang, *High-temperature sliding wear resistance of a ductile metal-toughened Cr<sub>13</sub>Ni<sub>5</sub>Si<sub>2</sub> ternary metal silicide alloy*, *J. Alloys Compd.*, 2007, vol.433, pp.114-119.
82. M.K. Stanford, C. DellaCorte, *Friction and wear characteristics of Cu-4Al foil bearing coating at 25 and 650<sup>o</sup>C*, 2004, NASA/TM-212972.
83. J.S. Zabinski, A.E. Day, M.S. Donley, C. DellaCorte, N.T. McDevitt, *Synthesis and characterization of a high-temperature oxide lubricant*, vol. 29, num. 22, pp. 5875-5879, DOI: 10.1007/BF00366870.
84. C. DellaCorte, V. Lukaszewicz, D.E. Morris, B.M. Steinetz, *Static and dynamic friction behavior of candidate high temperature airframe seal materials*, 1994, NASA Technical Memorandum 106571.
85. H. Heshmat, P. Hryniewicz, J.F. Walton II, J.P. Willis, S. Jahanmir, C. DellaCorte, *Low-friction wear resistant coatings for high-temperature foil bearings*, *Tribology international*, 2005, vol. 38, p.p 1059-1075.
86. K. Miyoshi, S.C. Farmer, A. Sayir, *Wear properties of two-phase Al<sub>2</sub>O<sub>3</sub>/ZrO<sub>2</sub>(Y<sub>2</sub>O<sub>3</sub>) ceramics at temperatures from 296 to 1073K*. *Tribology international*, 2005, vol. 38, pp. 974-986.
87. Haynes International Catalogue, Haynes 25, retrieved from: [www.haynesintl.com](http://www.haynesintl.com)
88. Haynes International Catalogue, Haynes 188, retrieved from: [www.haynesintl.com](http://www.haynesintl.com)
89. Haynes International Catalogue, Haynes 214, retrieved from: [www.haynesintl.com](http://www.haynesintl.com)
90. M.F. Aksit. "Patent: Actuator system for high temperature applicaitons", patent pending.

91. W. Roark, R. Budynas, "*Roark's formulas for stress and strain*", 7<sup>th</sup> edition. Chp 8, pp. 508.
92. J.P., Shingledecker, D.B. Glanton, R.L. Martin, B.L. Sparks, R.W. Swindeman, "*Tensile and creep-rupture evaluation of a new heat of Haynes alloy 25*", ORNL/TM-2006/609.
93. S. Bennett. *A History of Control Engineering: 1800-1930*. Peter Peregrinus, Stevenage, 1986.
94. S. Bennett. *A History of Control Engineering: 1930-1955*. Peter Peregrinus, Stevenage, 1986.
95. D. A. Mindel. *Between Human and Machine: Feedback, Control and Computing Before Cybernetics*. John Hopkins University Press, Baltimore, MD, 2002.
96. B. Bialkowski. Process control sample problems. In N. J. Sell (editor), *Process Control Fundamentals for the Pulp & Paper Industry*. Tappi Press, Norcross, GA, 1995.
97. F. G. Shinskey. *Process Control Systems. Application, Design, and Tuning*, 4th ed. McGrawHill, New York, 1996.
98. S. Yamamoto, I. Hashimoto. Present status and future needs: The view from Japanese Industry. In Y. Arkun and W. H. Ray (editors), *Chemical Process Control - CPCIV*, 1991.
99. T.-M. Yi, Y. Huang, M.I. Simon, and J. Doyle. Robust perfect adaptation in bacterial chemotaxis through integral feedback control. *PNAS*, 97:4649-4653, 2000.
100. K. Ogata, *Solving Control Engineering Problems with Matlab*. Eaglewoo Cliffs, NJ: Prentice Hall, 1994.
101. B. C. Kuo, *Automatic Control Systems*, 6th ed. Englewood Cliffs, NJ: Prentice Hall, 1991.
102. W. S. Levin, *The Control Handbook*. Boca Raton, FL: CRC Press, 1996.
103. W.R. Evans, *Control System Dynamics*. New York: McGrawHill Book Compan, 1954.
104. C. L. Phillips, R. D. Harbor, *Feedback Control Systems*, Eaglewoo Cliffs, NJ: Prentice Hall, 1988.
105. G. Rowell, D. Wormley, *System Dynamics*. Upper Saddle River, NJ: Prentice Hall, 1997.